



SRI KRISHNA COLLEGE OF TECHNOLOGY

[An Autonomous Institution | Affiliated to Anna University and Approved by
AICTE | Accredited by NAAC – UGC with 'A' Grade]

KOVAIPUDUR, COIMBATORE – 641042,INDIA



info@skct.edu.in | www.skct.edu.in

Ph: +91 422 2604567 to 70 | Fax: +91 422 2607152

CRITERIA 3

3.7.1 – Collaborative Activities

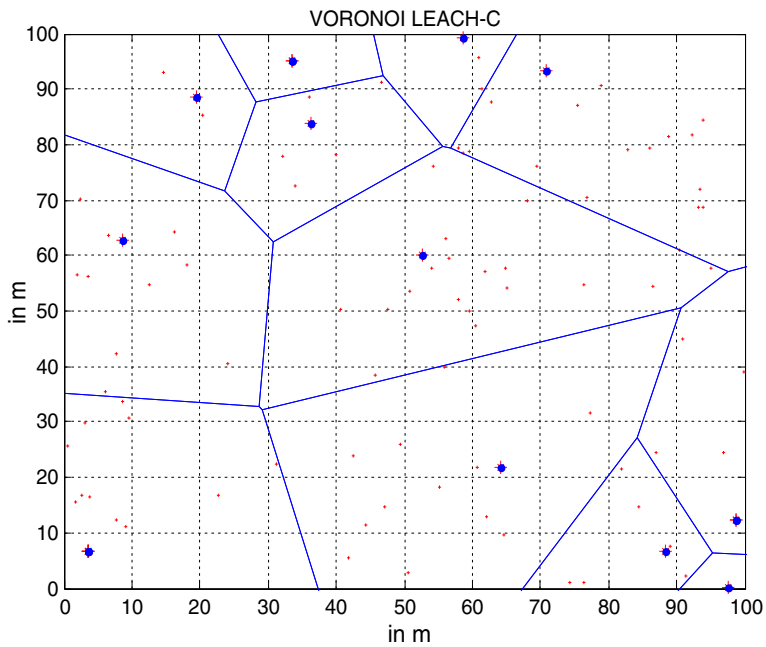


Fig. 10 VORONOI realization of LEACH-C

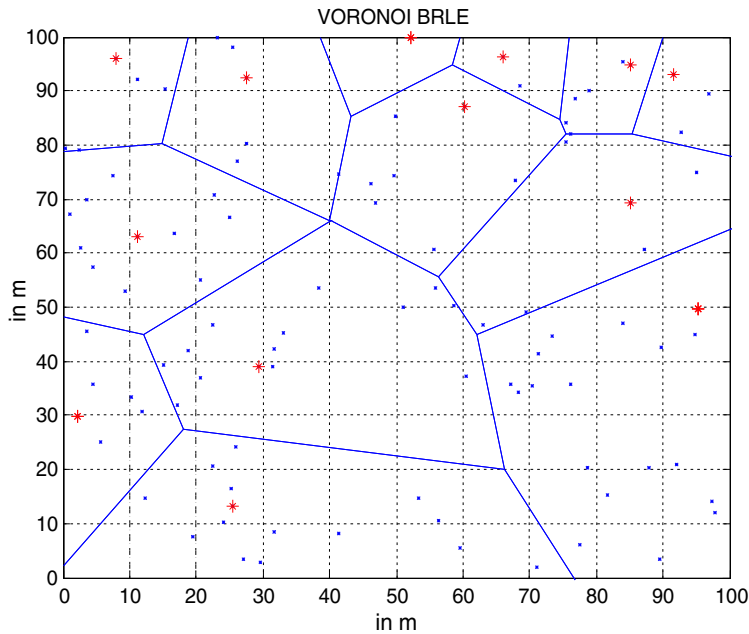


Fig. 11 VORONOI realization of BRLE

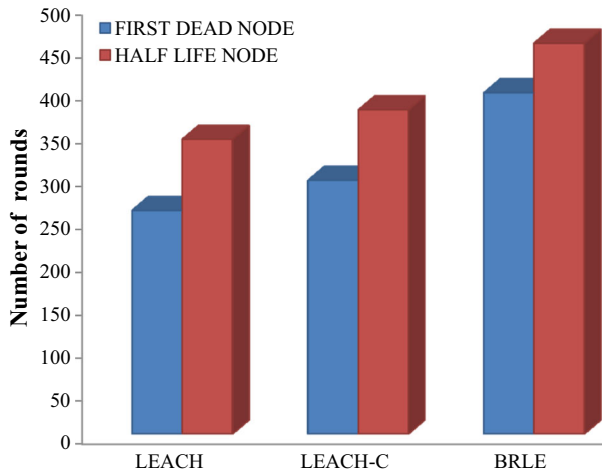


Fig. 12 Survivability comparison

The Voronoi representation of the LEACH, LEACH-C and proposed BRLE algorithm is given in Figs. 9, 10 and 11 respectively. In Figs. 8 and 9 the cluster formation is irrespective of the sink location. Figure 11 represents that the cluster formation of BRLE algorithm.

The clusters near the sink are observed to be smaller in size whereas the cluster far away from the sink is larger in size.

The hot spot and energy hole problem is avoided by employing unequal clustering in BRLE algorithm. The connectivity with the network is retained avoiding HOT SPOT problem in the network. Figure 12 represents the comparison of LEACH, LEACH-C and BRLE algorithms, First node dead and Half Node Alive (HNA) rate in BRLE algorithm is improved when compared to LEACH and LEACH-C. The BRLE shows improvement in the case of first dead node condition. The first node dies only after 397 rounds in case of BRLE, whereas in LEACH and LEACH-C protocols it dies at 260 round and 295 round.

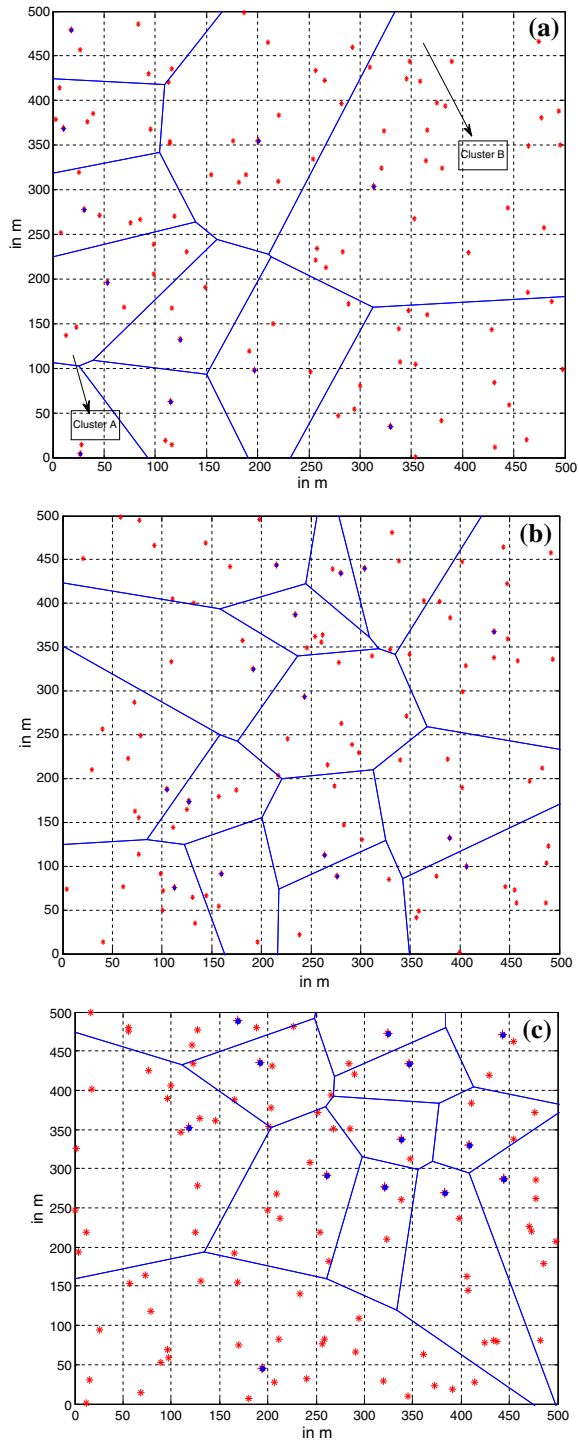
The sink is placed in different positions to verify the unequal clustering nature exhibited by the BRLE protocol. Figure 13 represents the unequal clustering of BRLE with different sink position.

In all cases the clustering is respect to the sink position as shown in Fig. 13a–c. The clusters near the sink are smaller and cluster far away from the sink is larger in nature.

7 Conclusion

The BRLE algorithm outperforms the LEACH and LEACH-C algorithm in terms of lifetime and throughput. The total number of packets sent to sink in case of BRLE algorithm is improved by 1.574 times when compared with LEACH protocol. The BRLE algorithm solves the HOT spot problem following unequal clustering approach. The BRLE algorithm serves as the better solution for energy hole problem in WSN. The result supports that the BRLE algorithm enhances the lifetime of the network with high throughput

Fig. 13 Unequal Clustering of BRLE. **a** Sink position (0, 0), **b** Sink position (250, 250), **c** Sink position (500, 500)



utilizing the battery effectively. The future work includes analyzing discharge time and recovery time of battery in different environments.

References

1. Tang, Q., Yang, L., Giannakis, G. B., & Qin, T. (2007). Battery power efficiency of PPM and FSK in wireless sensor networks. *IEEE Transactions on Wireless Communications*, 6(4), 1308–1319.
2. Kanagachidambaresan, G. R., & Chitra, A. (2015). Fail safe fault tolerant mechanism for wireless body sensor network. *Wireless Personal Communication*, 78(1), 247–260.
3. Kanagachidambaresan, G. R., & Chitra, A. (2016). Thermal aware-fail safe fault tolerant mechanism for wireless body sensor network. *Wireless Personal Communication*, 90(4), 1935–1950.
4. Li, H., Yi, C., & Li, Y. (2013). Battery friendly packet transmission algorithms for wireless sensor networks. *IEEE Sensors Journal*, 13(10), 3548–3557.
5. Chau, C. K., Qin, F., Sayed, S., & Wahab, M. H. (2010). Harnessing battery recovery effect in wireless sensor networks : Experiments and analysis. *IEEE Journal on Selected Area in Communication*, 28(7), 1222–1232. doi:[10.1109/JSAC.2010.100926](https://doi.org/10.1109/JSAC.2010.100926).
6. Leu, S. J., Chiang, T. H., Yu, M.-C., & Su, K. W. (2015). Energy efficient clustering scheme for prolonging the lifetime of wireless sensor network with isolated nodes. *IEEE Communication Letters*, 19(2), 259–262.
7. Nayak, P., & Devulapalli, A. (2016). A fuzzy logic based clustering algorithm for WSN to extend the network lifetime. *IEEE Sensor Journal*, 16(1), 137–144.
8. Akyildiz, I. F., Su, W., Sankarasubramaniam, Y., & Cayirci, E. (2002). Wireless sensor networks: A survey. *Computer Networks*, 38(4), 393–422.
9. Rukpakavong, W., Guan, L., & Phillips, I. (2014). Dynamic node lifetime estimation for wireless sensor networks. *IEEE Sensors Journal*. doi:[10.1109/JSEN.2013.2295303](https://doi.org/10.1109/JSEN.2013.2295303).
10. Karakus, C., Gurbuz, A., & Tavli, B. (2013). Analysis of energy efficiency of compressive sensing in wireless sensor networks. *IEEE Sensors Journal*, 13(5), 1999–2008.
11. Li, Y., Bakkaloglu, B., & Chakrabarti, C. (2007). A system level energy model and energy-quality evaluation for integrated transceiver front-end. *IEEE Transactions on Very Large Scale Integration (VLSI) Systems*, 15(1), 90–103.
12. Pantazis, N. A., Nikolidakis, S. A., & Vergados, D. D. (2013). Energy efficient routing protocols in wireless sensor networks: A survey. *IEEE Communications Survey and Tutorials*, 15(2), 551–591.
13. Lajara, R. J., Perez solano, J. J., & Pelegri-Sebastia, J. (2015). A method for modeling the battery state of charge in wireless sensor networks. *IEEE Sensors Journal*, 15(2), 1186–1197. doi:[10.1109/JSEN.2014.2361151](https://doi.org/10.1109/JSEN.2014.2361151).
14. Lee, J. S., & Cheng, W. L. (2012). Fuzzy logic based clustering approach for wireless sensor networks using energy predication. *IEEE Sensors Journal*, 12(9), 2891–2896.
15. Kim, J. Lee, S. & Cho, B. (2009). Discrimination of battery characteristics using discharging/charging voltage pattern recognition, In *Proceedings IEEE conference on energy conversion congress and exposition* (pp. 1799–1805).
16. Cloth, L. Haverkort, B. R. & Jongerden, M. R. (2007). Computing battery lifetime distributions, In *Proceedings 37th annual IEEE international conference on dependable system network* (pp. 780–789).
17. Rakhmatov, D., Vruthula, S., & Wallach, D. (2003). A model for battery lifetime analysis for organizing applications on a pocket computer. *IEEE Transactions on Very Large Scale Integration (VLSI) Systems*, 11(6), 1019–1030.
18. Jongerden M. R. & Haverkort, B. R. (2008). Battery modeling, Department of Electrical Engineering and Mathematical Computer Science, Design Analysis Communication System, Technical Report TR-CTIT-08-01, University of Twente, Enschede.
19. Ma, C., & Yang, Y. (2006). Battery-aware routing for streaming data transmissions in wireless sensor networks. *Mobile Networks and Applications*, 11, 757–767.
20. Li, Y., Li, H., Zhang, Y., & Qiao, D. (2010). Packet transmission policies for battery operated wireless sensor networks. *Journal of Frontiers Computer Science in China*, 4(3), 365–375.
21. Abouzar, P., Michelson, D. G., & Hamdi, M. (2016). RSSI-based distributed self-localization for wireless sensor networks used in precision agriculture. *IEEE Transactions on Wireless Communications*, 15(10), 6638–6650.
22. Luo, Q., Peng, Y., Li, J., & Peng, X. (2016). RSSI-based localization through uncertain data mapping for wireless sensor networks. *IEEE Sensors Journal*, 16(9), 3155–3162.

23. Yaghoubi, Forough, Abbasfar, Ali-Azam, & Maham, Behrouz. (2014). Energy-efficient RSSI-based localization for wireless sensor networks. *IEEE Communications Letters*, 18(6), 973–976.
24. Nuggehalli, P., Srinivasan, V., & Rao, R. R. (2006). Energy efficient transmission scheduling for delay constrained wireless networks. *IEEE Transactions on Wireless Communications*, 5(3), 531–539.
25. Chiasserini, C. F., & Rao, R. R. (2001). Improving battery performance by using traffic shaping techniques. *IEEE JSAC Wireless Series*, 19(7), 1385–1394.
26. Ma, C. & Yang, Y. (2005). Battery aware routing in wireless ad hoc networks. Part II. Battery-aware routing. In Proceeding of 19th international tele traffic congress (ITC-19) (pp. 303–312).
27. Rakhmatov, D., & Vrudhula, S. (2003). Energy management for battery-powered embedded systems. *ACM transactions embedded. Computing Systems*, 2(3), 277–324.



V. Mahima received her Bachelor degree in Electronics and Communication Engineering in 2011 and her Master degree in Applied Electronics in 2013 from Anna University. She is currently a Part time research scholar in PSG College of Technology. She is currently working as an Assistant Professor in the Department of Electronics and Communication Engineering, Sri Krishna College of Technology, Coimbatore. Her research interest includes Energy management and Quality of Service issues in Wireless Sensor Network.



A. Chitra is Professor and Head, Department of Computer Applications, PSG College of Technology. She has more than two decades of experience in teaching and research. She holds a BE, ME and Ph.D. in Computer Science and Engineering from Bharathiar University, Coimbatore. Chitra is the recipient of Tamil Nadu Young women Scientist Award, ISTE National award for Outstanding Academician and IETE MN Saha Award and a gold medal for the Best application oriented paper published in IETE journals during 2007. She has published prolifically and her books include programming with Data Structures, C Programming and Internet and Java Programming. She has published around 100 papers in national/international journals and conferences. She is a Fellow member of Institution of Engineers, Life member of ISTE, ACCS and CSI. She is the secretary of the ACCS Coimbatore chapter.



Original research article

D-glucose sensor using photonic crystal fiber



Harikesavan Thenmozhi^a, MuruganSenthil Mani Rajan^{a,*}, Veluchamy Devika^a,
Dhasarathan Vigneswaran^b, Natesan Ayyanar^c

^a Department of Physics, University College of Engineering, Anna University, Ramanathapuram, 623513, India

^b Département Of ECE, Sri Krishna Collège of Technology, Coimbatore, 641 042, India

^c Department of Electronics and Communication Engineering, Dhirajlal Gandhi College of Technology, Salem, Tamilnadu, 636309, India

ARTICLE INFO

Article history:

Received 20 March 2017

Accepted 3 August 2017

Keywords:

Biosensor

Diabetes

D-glucose

Photonic crystal fiber

Refractive index

Tuberculosis

ABSTRACT

We propose triangular lattice structured photonic crystal fiber (PCF) sensor for sensing applications with attractive features for the detection of glucose concentration. The proposed sensor is numerically investigated using Finite Element Method (FEM). We have investigated the sensing property of the proposed photonic crystal fiber structure by varying the concentration of the D-glucose from 10%–60% which gives the average sensitivity of 19135.70 nm/RIU. We expect that this sensor can provide an effective platform for glucose sensing and potentially leading to a further development of optical sensing applications.

© 2017 Elsevier GmbH. All rights reserved.

1. Introduction

Diabetes, as a medical condition, is ever on the increase and a large number of people require Continuous Glucose Monitoring which is not only highly accurate but also compact and minimally invasive [1]. It is in this background that we find the Photonic Crystal Fibres to play a very important role in the field of sensors due to design flexibility, high sensitivity and large refractive index contrast. The Photonic Crystal Fiber (PCF) based sensors are well developed and found to offer extremely high sensitivity reported in the last few decades. [2,3]. Several methods like surface plasmon resonance (SPR) based sensors [4], Ring resonant cavities [5,6] and mid-infrared photo acoustics [7,8] have been proposed in the literature for sensing the blood glucose concentration. PCF sensors develop the potential virtues of optical fibers in chemical [9] and biological sensing [4,5,7,8] applications.

Glucosuria is glucose in the urine which is an indirect index of the blood glucose concentration [10,11] and ranges from 0 mg/dl – 15 mg/dl. Normal blood glucose levels range between 165 mg/dl and 180 mg/dl. If the blood glucose concentration reaches a very low value of less than 40 mg/dl, the condition is called “Hypoglycemia” and the condition where the blood glucose concentration is very high and ranges from 270 mg/dl to 360 mg/dl [12] is called “Hyperglycemia”. Glucose concentration in the blood level is affected by physical properties such as refractive index, specific gravity, surface tension and viscosity of the blood/plasma. In this work, we consider the D-glucose solution to analyze and predict the sensitivity of PCF with reference to variation in the refractive index of the solution. D-glucose solutions with different concentrations have been investigated whose refractive index values varies from 1.3477 to 1.4394 at 10%–60% [13] concentrations.

* Corresponding author at: Department of Physics, University College of Engineering, Anna University, Ramanathapuram, 623513, India.
E-mail address: senthilmanirajanofc@gmail.com (M. Mani Rajan).

D-glucose is a form of sugar to treat hypoglycemia which will bring the blood glucose concentration to their normal levels very quickly. Dextrose can be used in intravenous (IV) preparations and injections in clinics for hypoglycemia and dehydration and for IV feeding since dextrose has a very high glycemic index. People with dangerously low blood glucose concentrations may be treated with dextrose tablets or gels. Dextrose is the dextrorotatory form of glucose which can be used by athletes as a supplementary to manage the blood sugar levels and also for replenishing glycogen during and after workouts. It can also be used as a “carrier” in nutritional supplements. When using dextrose, blood sugar levels should be closely monitored to prevent hyperglycemia.

Diabetes mellitus has been well reported to be associated with increased risk of tuberculosis [14–17]. The presence of indefinite social factors, metabolic derangements and comorbidities also poses major difficulties in dissecting the effect of diabetes mellitus from other potential confounders. Diabetes mellitus was diagnosed, mainly by a fasting plasma glucose level of 126 mg/dl or higher, together with confirmatory symptoms and/or blood/plasma glucose determinations.

We investigated a particular design of PCF based glucose sensor to diagnose the variation in the blood glucose level. Different types of PCF based sensors like single core, multi core and 2D-phonic crystals based sensors have been proposed for various sensing purposes in the literature. In this context we optimized a triangular structure based glucose sensor design utilizing the index guiding multi core fibers and present a numerical analysis based on the finite element method [FEM]. It is worthwhile to mention that this PCF based glucose sensor is a novel sensor which offers high sensitivity and linearity over the other type of PCF based sensors. The designed structure provides a very large dynamic refractive index detection range and comparatively provides high sensitivity range for temperature sensing [18]. In our context, the triangular lattice structure [18] is proposed due to its high detection range for continuous monitoring of glucose in human blood providing high sensitivity, which will pave to identify the glucose concentration to replace the existing glucose sensor with high sensitivity as well for a long term use. The proposed work creates a great deal for the physicians and the patients. It also provides integrated understanding of diseases and creates opportunities for new diagnosing methods.

2. Structure designed

The cross section of the proposed fiber sensor is shown in Fig. 1. with six identical solid cores with the increase of dynamic refractive index [RI] detection range shown by Qiang Liu et al. [18] in their temperature sensor. To obtain the high sensitivity with easier fabrication, the air holes are arranged in a triangular lattice having pitch constant (Λ) of 2 μm and diameters of all the air holes are optimized at $d = 1.2 \mu\text{m}$. In the second layer, the defect mode is created by removing the air holes which enhances the propagation of chosen wavelength of light into the liquid core. Its mode propagation is studied using FEM and the electric field distribution is shown in Fig. 2(a)–(l).

Glucose of 60% concentration with refractive index of 1.4394 at room temperature (20 °C) is filled into the central air hole of the designed PCF structure. Refractive index of the glucose in water solution is tunable for different concentration (10%–60%). All the modes in the PCF are leaky modes because the real part of the refractive index is lower than background material. The leaky mode can be controlled by choosing the suitable liquid material with the appropriate refractive index. The energy transfer between the liquid core mode and defect mode can be identified by the peak wavelength.

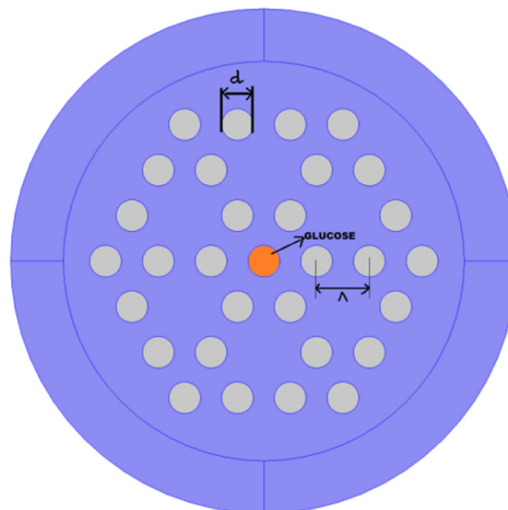


Fig. 1. Cross section of proposed glucose sensor based on PCF.

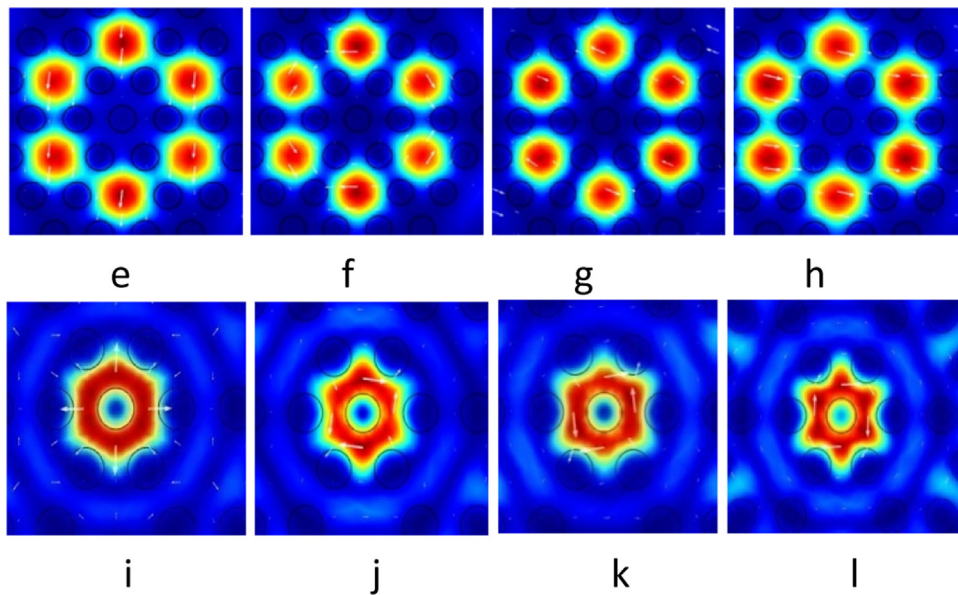


Fig. 2. Electric field distributions of (a)–(h) defect modes and (i)–(l) liquid-core modes. The arrow represents the direction of the electric field. The coupling between defect and core modes are shown in Fig. 2(b) and 2(l), as well in 2(a) and 2(i) were employed to analyze our glucose sensor, respectively.

Table 1

Concentration of D-glucose in water at 20 °C.

Mass%	C Molarity (moles of solute per liter of solution)	C (mmole/liter)	C (mg/dl)	Refractive index (RIU)	Peak wavelength (nm)
10	0.576	576	33.6842	1.3477	1500
20	1.070	1070	62.57309	1.3635	1480
30	1.873	1873	109.88304	1.3805	1460
40	2.603	2603	152.222	1.3986	1440
50	3.396	3396	198.596491	1.4181	1420
60	4.261	4261	270.233	1.4394	1380

The background material of the fiber is filled with silica whose refractive index is calculated by Eq. (1). The RI of analyte is taken for different concentrations of glucose in water and the values are tabulated in Table 1.

$$n^2(\lambda) = 1 + \frac{B_1\lambda^2}{\lambda^2 - C_1} + \frac{B_2\lambda^2}{\lambda^2 - C_2} + \frac{B_3\lambda^2}{\lambda^2 - C_3} \quad (1)$$

By using FEM, the study about the fundamental modes and its coupling modes with good radiation absorber has been analyzed by adding perfectly matched layers (PML) with scattering boundary condition. The cylindrical coordinate is used for PML to absorb the radiant energy from fiber axis. The outer boundary of PML is set with scattering boundary condition to further reduce reflecting energy. In our glucose sensor, the coupling between the liquid core and defect modes are shown in Fig. 2(a) & (2l) and 2b & 2i.

3. Numerical results

In this numerical investigation, we have calculated the loss by using Eq. (2) where unit of the loss and wavelength is dB/m and μm respectively and $\text{Im}(n_{\text{eff}})$ represents the imaginary part of the effective refractive index of mode.

$$\alpha(x, y) = 8.686 * \frac{2\pi}{\lambda} \text{Im}(n_{\text{eff}}) * 10^6 \quad (2)$$

The illustrations of mode field distributions are displayed in Fig. 3(a) which represents the real part of refractive index and loss dependence on the operating wavelength λ for the different samples of the glucose. For the upper mode, the mode field is mainly distributed in liquid core at the shorter wavelength, mode field begins to transfer from liquid core to defect cores as wavelength increases, the energies of liquid-core mode and defect mode are equal at the turning of the curve and almost all the field transfers from liquid core to defect core at the longer wavelength. For the lower mode, the mode transition is contrary to that of the upper mode. Fig. 3(b) shows the loss as a function of wavelength. For the black solid curve in Fig. 3(b) the loss follows liquid core mode at the shorter wavelength and follows defect mode at the longer wavelength. The losses of liquid core mode and defect mode are equal at the intersection of black and red solid curve. The intersection corresponds to

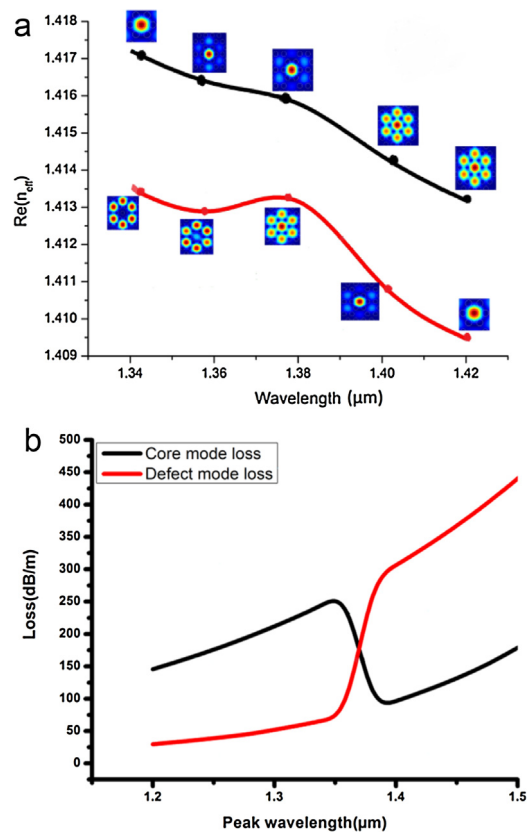


Fig. 3. (a) The real part of core mode (red) and defect mode (black) refractive index for the chosen wavelength. The insets in (a) show electric field distributions and transfer of energy between fundamental and liquid mode. (b) Loss as a function of wavelength. (For interpretation of the references to colour in this figure legend, the reader is referred to the web version of this article.)

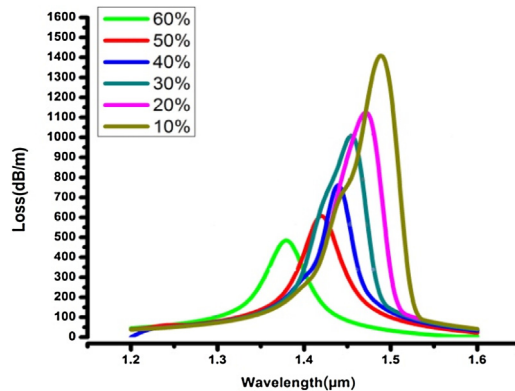


Fig. 4. Simulated results show the relation between confinement loss and different samples of glucose solution.

the tuning of the curve in Fig. 3(a) which shows the complete coupling. The coupling between a liquid core mode and defect mode is shown in Fig. 2(l) and 2(a) which gives perfect coupling.

The simulated result (Fig. 4) gives the relationship between confinement loss and wavelength for different concentrations of the samples. We can see that the resonance wavelength blue-shifts with each increment of the glucose concentration. The spectral sensitivity of the corresponding sensor can be obtained as

$$S \left(\text{nm}/\text{RIU} \right) = \Delta\lambda / \Delta n \quad (3)$$

Where $\Delta\lambda$ is the offset of the resonant wavelength and Δn is the change in the RI of glucose solution. When the RI of the glucose solution is changed, the resonance spectrum will be varied. Therefore, we can obtain information about the analyte according to the change of the resonance wavelength. When the glucose concentration changes from 10 mg/dL to 60 mg/dL

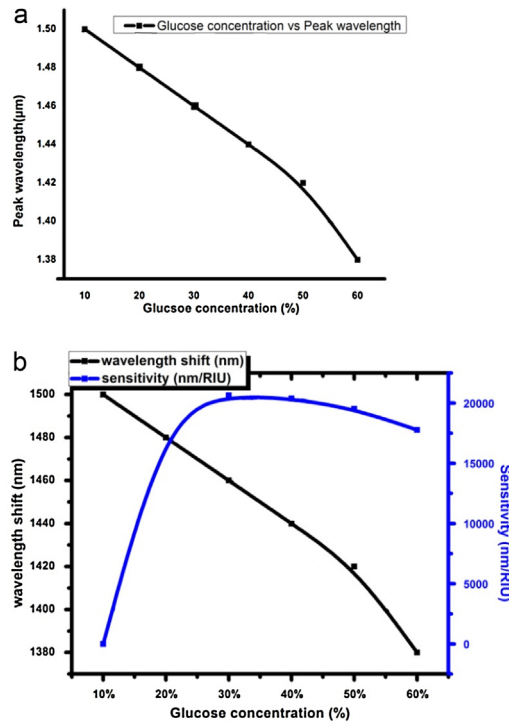


Fig. 5. (a) Represents the peak shift and sensitivity value for the D-glucose concentration varying from 10%–60%. (b) Represents the resonance wavelength as the function of varying glucose concentration.

the offset of the resonance wavelength $\Delta\lambda$ is 120 nm. The increment of solution RI is 6.27×10^{-3} , and the average spectral sensitivity 19135.70 nm/RIU can be obtained by experiments. Their solution of the spectrograph we used is 1 nm, and then the detection resolution of the sensor is 47.30 mg/dl of D-glucose in water, which is lower than 70 mg/dl for efficient detection of hypoglycemia episodes. We observed the change in peak wavelength by varying the concentration of the glucose. Peak wavelength is decreased when we increase the concentration of the glucose and loss is decreases as shown in Fig. 4. The total wavelength shift is obtained is 120 nm.

The resonance or peak wavelength for the different concentration of glucose at a refractive index of 20 °C with the wavelength shift of the proposed glucose sensor is as shown in Fig. 5(a). The average sensitivity can reach upto 19135.70 nm/RIU. The high linearity can reach upto 0.99872. This is important in the actual application for the sensor. In Fig. 5(b) we have represented the wavelength shift and the sensitivity value for varying concentration of D-glucose between 10%–60%. It is calculated that wavelength shift of 20 nm for 20% D-glucose concentration in the water solution. The sensitivity of designed PCF sensor is 19120.45 nm/RIU for the 20% of D-glucose concentration with a detection limit of 0.006271 RIU.

4. Conclusion

In this paper, we analyzed a PCF glucose sensor filled with different concentrations of glucose solution. The results show that a blue-shift is obtained with increasing the RI of filling analyte and an extremely high average spectral sensitivity of 19135.70 nm/RIU. A high-sensitivity glucose sensor based on compact PCF is proposed by the finite element method. A glucose sensitivity material is injected into the central air hole of PCF which supports liquid core mode. The six cores in the second layer are formed by removing air holes and work as defect mode. As phase matching condition is satisfied, the liquid-core mode couples to defect mode completely and reveals loss peak which is employed to detect glucose concentration. The sensor shows high sensitivity and high linearity. Our glucose sensor of simple structure is competitive in the glucose sensor field and suitable to measure glucose concentration in real time. The structure can be further optimized to obtain better results.

References

- [1] Michael S. Boyne, David M. Silver, Joy Kaplan, Christopher D. Saudek, Timing of changes in interstitial and venous blood glucose measured with a continuous subcutaneous glucose sensor, *Diabetes* 52 (2003) 2790.
- [2] Julie Wagner, Howard Tennen, Howard Wolpert, Continuous glucose monitoring: a review for behavioral researchers, *Psychosom. Med.* 74 (4) (2012) 356.
- [3] H. Barry, G. Ginsber, An overview of minimally invasive technologies, *Clin. Chem.* 38/9 (1992) 1596.

- [4] Abdulhalim Srivastava, Spectral interrogation based SPR sensor for blood glucose detection with improved sensitivity and stability, *J. Biosens. Bioelectron.* 6 (2015) 172.
- [5] Poonam Sharma, Preeta Sharan, Photonic crystal based ring resonator sensor for detection of glucose concentration for biomedical applications, *Int. J. Emerging Technol. Adv. Eng.* 4 (2014) 702.
- [6] P. Sharma, Photonic crystal based ring resonator sensor for detection of glucose concentration for biomedical application, *IJETAE* 4 (2014) 706.
- [7] M.R. Pintoa, M. Baptistaj, J.L. Santos, M.A. Lopez, O. Frazão, Micro-displacement sensor based on a hollow-core photonic crystal fiber, *Sensors* 12 (2012) 17497.
- [8] C.M.B. Cordeiro, M.A.R. Franco, G. Chesini, E.C. Barretto, R. Lwin, C.H.B. Cruz, Micro structured-core optical fiber for evanescent sensing applications, *Opt. Exp.* 14 (2006) 13056.
- [9] A.M. Cubillas, S. Unterkofler, T.G. Euser, B.J.M. Etzold, A.C. Jones, P.J. Sadler, P. Wasserscheid, S.T.J. Russell, Photonic crystal fibers for chemical sensing and photochemistry, *Chem. Soc.* 42 (2013) 8629.
- [10] P. Sharma, P. Sharan, Design of photonic crystal-Based biosensor for detection of glucose concentration in urine, *IEEE Sens.* 15 (2015) 1035.
- [11] R. Savarimuthu, N. Dhanlaksmi, Photonic crystal based biosensor for the detection of GlucoseConcentration in urine, *Photonic Sens.* 7 (2017) 11.
- [12] P. Sharma, P. Sharan, Design of photonic crystal based biosensor for detection of glucose concentration in urine, *IEEE Sens.* 15 (2) (2015) 1035.
- [13] R. Lide David, *Handbook of Chemistry and Physics*, 84th edition, CRC PRESS), 2003 (2003–2004).
- [14] The Diabetes control and complications Trial Research Group. The effect of intensive treatment of diabetes on the development and progression of long-term complications in insulin-dependent diabetes mellitus, *J. New Engl. Med.* 329 (1993) 977.
- [15] D.M. Peterson, D.L. Jones, A. Dupuis, Bernstein, M. O'shea, Feasibility of tight control of juvenile diabetes mellitus through patient monitored glucose, *Diabetes* 27 (1978) 437.
- [16] P.H. Sönksen, S.L. Judd, C. Lowy, Home monitoring of blood glucose, *Lancet* 1 (1978) 729.
- [17] S. Walford, E. Gale, S.P. Allison, B. Tattersallr, Self-monitoring of blood glucose, *Lancet* 1 (1978) 732.
- [18] L.I.U. Qiang, L.I. Shuguang, Hailiang Chen, Zhenkai Fan, L.I. Jianshe, Photonic crystal fiber temperature sensor based on coupling between liquid-Core mode and defect mode, *IEEE Photonics* 7 (2015) 2.

Power model analysis using variable rate clock network in CMOS processor

T.Joby Titus
Assistant
Professor(Sr.Gr)
Department of ECE
Sri Ramakrishna Institute
of Technology,
Coimbatore
+919489915620
jobytitus.ece@srit.org

Dr.V.Vijayakumari
Professor,
Department of ECE
Sri Krishna College of
Technology,
Coimbatore
+919486654147
ebinviji@rediffmail.co
m

B.Saranya
Assistant Professor,
Department of ECE
Sri Ramakrishna Institute
of Technology,
Coimbatore
+919677553626
saranyab.ece@srit.org

V.S.Sanjana Devi
Assistant Professor,
Department of Electrical
and Electronics
Engineering
Sri Krishna College of
Technology
+917402600147
v.s.sanjanadevi@skct.
edu

ABSTRACT

In this paper, we present a variable node clock network and a power model to estimate leakage power in CMOS processor. Design of clock delivery network is a constrained optimization problem. A variable rate clock network is provided to reduce unwanted switching as well as to limit active clock routing network. We propose two power models to estimate processor performance under variable rate clock signal. Overall this optimization method provides improved in power and performance in current CMOS processor.

Keywords

Lookup table; CMOS Processor; Variable clock; sub clock.

1. INTRODUCTION

As the technology scales high performance VLSI circuits is highly desirable as it directly relates to battery life, reliability, packing and heat removal cost. Among the total power consumption in CMOS processor, leakage power contributes to maximum value. Scaling of supply voltage and frequency reduces dynamic power but degrades the performance of the device. A topology-based solution for a low-skew rotary oscillator array (ROA) clock distribution network design and skew calculation is mentioned in [1] & [6]. A half-rate clock to the common mode of the differential data with its mixing phase off by 0.5 UI and Multi-domain clock skew scheduling (MDCSS) is one way to overcome this limitation also the power reduction is analyzed through two mechanisms: 1) power gating the logic network within the clock period (sub clock) and 2) reducing the virtual supply to less than threshold voltage rather than shutting down completely as is the case in conventional power gating [7]-[13].

Permission to make digital or hard copies of all or part of this work for personal or classroom use is granted without fee provided that copies are not made or distributed for profit or commercial advantage and that copies bear this notice and the full citation on the first page. Copyrights for components of this work owned by others than ACM must be honored. Abstracting with credit is permitted. To copy otherwise, or republish, to post on servers or to redistribute to lists, requires prior specific permission and/or a fee. Request permissions from Permissions@acm.org.

ICCCNT '16, July 06-08, 2016, Dallas, TX, USA

© 2016 ACM. ISBN 978-1-4503-4179-0/16/07...\$15.00

DOI: <http://dx.doi.org/10.1145/2967878.2967915>

As the dynamic power contribution is related to increase in active interconnection and number of active devices used, it is necessary to reduce the factors affecting dynamic power consumption without performance degradation. A system level methodology for interconnection analysis and multibit flip-flop utilization is mentioned [14]-[16]. The supply noise produced by switching is analyzed using virtual circuit switching and packet switching. Systematic approach to actively alleviating Power Gating noises using the parasitic capacitance of on-chip memories and unconventional power grid optimization solution that allows to resize each transistor specifically. A technique that decreases the parasitic capacitance on the dynamic node, yielding a smaller keeper for wide fan-in gates to implement fast and robust circuits were analyzed [2]-[5]. A fine-grained approach where each gate in the circuit is provided with an independent sleep transistor and major disadvantage is clustering-based approaches utilized with polynomial-time fine-grained sleep transistor sizing algorithm [13], [17]-[18]. Sleep transistor sizing is one of the most important concerns for designing CMOS processor because it affects the overall circuit performance. In order to optimize leakage power, worst case IR drops is to be estimated. Valuable information points the technique of variable clock network to activate leakage power controller. Leakage power is estimated using power models at clock controller network and logic network.

2. RELATEDWORK

Numerous power model techniques over the earlier periods have been introduced to reduce the power consumption of CMOS processor. The switching activity of clock network typically accounts for major contribution of total power consumption. Power consumption in CMOS processor is caused by four sources

- Leakage current i.e., Reverse bias current and sub threshold current formed during idle mode of processor
- Stand by current drawn from V_{DD} to ground
- Short circuit current between supply rails
- Capacitance current during active mode

In [Jee Khoi Yin], multi phase clock signals for logic network using ultra grained pipelines to improve the performance of CMOS processor. In fact, two phase clock scheme leads to race through failure if overlap of clock signal is too long in consecutive stages. In [Jain Peng Zhu], a circuit level power model is developed to estimate low voltage level. In [YiCi Cai],

lookup table based delay estimation is provided. A lookup table is built through SPICE simulator to estimate delay and slow. A buffer insertion algorithm is utilized for slow optimization; also a sampling technique is adapted to speedup buffer insertion algorithm. The static power issues associated with large register file is mentioned in [Hamed Tabkhi]. A functional level register file power gating is introduced to manage and reduce static power consumption. Register file power contributes to reduction in core power of CMOS processor. However delay and performance of the processor is not taken into account by these approaches. Reducing power consumption at clock network level and logic block level is important because 1. Clock network itself contributes to major portion of core power consumption. 2. Logic block level power consumption is taken into account both in active mode and standby mode of processor. Most existing approaches have focused on power consumption by proposing clock gating and power gating techniques without considering the performance and area overhead of the design. The power model analysis is an application guided architecture level solution targeting CMOS processor. To put our work in context, the next paragraph focus on clock network and logic level power estimation technique.

In this paper, we propose a variable rate threshold voltage selection based on high and low active data lines. A power model algorithm variable data active line is also proposed. Both the threshold voltage controller and power model methods can be successfully applied to improve power and performance of CMOS processor. The remainder of this paper is organized as follows. In section-2 surveys some related work. Section-3 explains clock and power gating controller at circuit level. Section-4 focused on variable clock rate & leakage controller. In section-5 the power model and threshold voltage selection is introduced. Evaluation of CMOS processor blocks are presented in section-6. Finally section-7 concludes this.

3. CLOCK AND POWER GATING CONTROLLER AT CIRCUIT LEVEL

At circuit level the total power dissipation consists of leakage, short circuit and switching components. There are several clock controller techniques that utilizes flip flop grouping in data driven clock network, factored form of logic block matching to utilize clock network, half rate and multiphase clock signal to improve the performance of CMOS processor. Supply voltage scaling, clock polarity assignment for gated clock network provide minimized dynamic power consumption but all these methods the delay, area and performance of CMOS processor is not considered as major criterion.

Static power is contributed by major factor called leakage current and transistor size. Several leakage power reduction techniques such as fine grained transistor placement, tunable sleep transistor insertion, intermediate power off modes is concentrated on power reduction in standby mode of CMOS processor. In coarse grained reconfigurable architecture and sub clock power gating the control network enabled based on data activity modes which leads to power reduction during active modes. Our proposed approach could utilize a variable clock network and power model estimation in active and standby modes.

4. VARIABLE CLOCK NETWORK AND LEAKAGE

Clock signals are utilized at system level for enabling logic operation. In many cases clock enabling signals are fixed throughout the processor. It is important to note that the entire

switching power consumed by the processor is die to unnecessary switching of logic blocks and frequency of the priority of usage of clock signal it is necessary to consider the factors such as frequency and switching activity for both active mode and idle mode of processor.

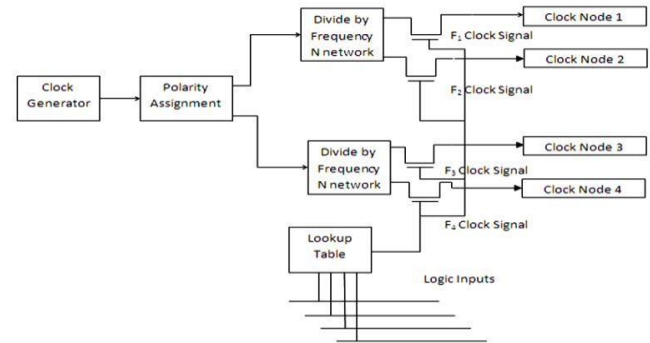


Fig.1: Fixed and variable clock activation network

Fig.1 shows the fixed and variable clock usage for logic network. The variable rate clock signal is generated from common clock generator circuit. The clock signal is utilized as two phase transition clock based on the priority of usage more over the driven polarity assigned clock pulse is modified as two different clock frequency. The variable clock frequency is selected based on data activity using lookup table controller. This clock frequency signal is activates clock nodes of logic network in active mode. Hence unnecessary switching of logic network is minimized which leads to reduced power consumption.

In order to minimize leakage current during standby mode a leakage controller is proposed which utilizes the enable signal generated from lookup table. As the switching activity poses more amount of power consumption during active and idle mode. Two major factors to be considered for leakage power reduction are supply voltage scaling and increasing threshold voltage for transistor network. To achieve these goals, the data activity of logic block input enables the clock network and leakage controller.

5. PROPOSED POWER MODEL ANALYSIS

Two major components contribute to power dissipation in CMOS processor are clock network and number of transistors utilized. Dynamic power is mainly derived from clock network switching component. Therefore the paper focuses on clock network controller which minimizes unnecessary switching of logic network. The total load capacitance which contributes to switching power is minimized using lookup table based active selection of logic network.

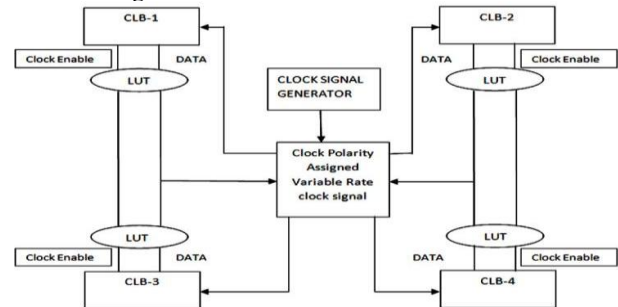


Fig.2 Proposed clock and data activity in power model analysis

This work used computes the power associated with clock network through the circuit model as shown in figure. The clock node power consumption depends on activity of logic network, supply voltage, frequency of clock signal and capacitance of active inputs.

$$P_{\text{Clock node}} = \alpha_N f_N V_{DD}^2 C_N \dots \dots \dots (1)$$

The term α_N designates the total switching activity resulting as the algebraic sum of activity in logic network. The activity of logic network is minimized by Lookup table controller. The clock network frequency is assigned as variable rate clock signal. The logic network utilizing maximum switching activity is supplied with maximum frequency clock signal and minimum frequency clock signal is connected with less activity logic network in order to avoid reduction in performance of logic network. Based on the logic activity, Lookup table provides enable signal to select supply voltage connected with logic network. The logic network is activated and connected with 3.5V and 2.5V based on data active lines. The power model analysis also includes estimation of inter connection capacitance and transistor capacitance. This method of analysis includes power calculation based on data active lines.

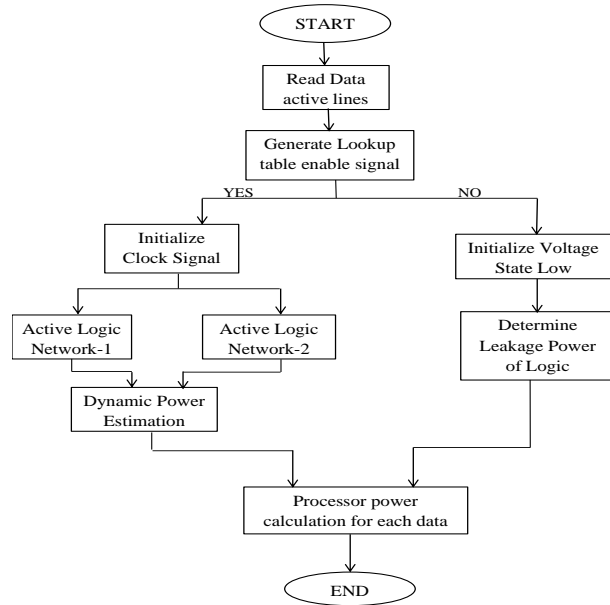


Fig.3 Proposed power model analysis

Power model analysis in leakage mode leads to a complex procedure. Leakage current is increased by the usage of large number of transistors and also due to the variation of threshold voltage. Power model analysis for leakage controller is concentrated on supply voltage reduction and threshold voltage variation without affecting the processor performance. Lookup table provides an enable signal to activate and to provide idle state to logic network.

6. EXPERIMENTAL RESULTS

In this section we present the simulation results for data activated logic blocks using Tanner Eda tool. The design flow described in section IV is experimented on two set of logic network. The power model for dynamic power calculation is analyzed and compared with the logic network in which all the data activity

lines are at high state. For leakage power controller network the entire logic network power is calculated and compared with active mode power of logic network.

In the proposed approach the variable frequency clock provides the timing simulation for logic network activity and the delay overhead is analyzed by comparing the processor result with logic network where the controller network is disabled. Initially, we show the power variation for logic network which is unutilized by controller network. In Fig.4, the timing diagrams for normal clock, polarity assigned clock and variable clock which propagates to activate logic network. Based on these clock signal variation the switching activity of logic network is varied and power model analysis is carried out.

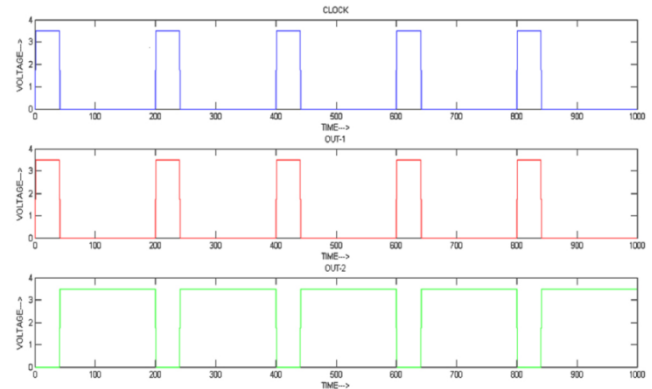


Fig.4: variable clock and output switching characteristics

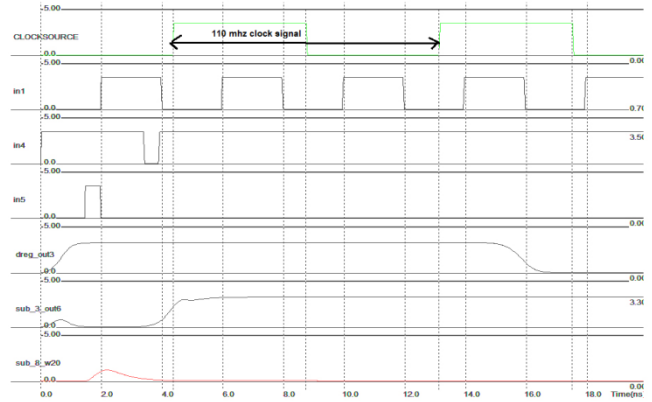


Fig.5: Fixed rate clock signal activating logic network

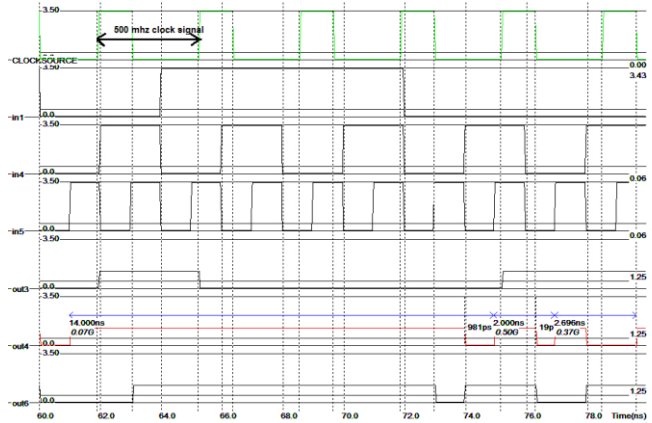


Fig.6: Variable rate clock signal activating global nodes

Fig.5,6 indicates the variable and fixed clock enabling the logic network based on data active lines. The performance of logic network is improved based on selection of variable rate clock signal. In Table –I and Table-II the comparison of power, leakage current and area estimation of various CMOS processor utilizing variable clock and leakage controller.

Table-I Power and Area analysis for various CMOS processor

CMOS Processor	No. of Transistors	Clock Frequency	Power	Leakage Current	Area of logic network
0.12μm	892	0.51Ghz	16.88mw	13.892mA	112.8μm×1249.2μm
0.25 μm		0.5Ghz	8.501mw	6.978mA	23.5μm×131.3μm
90nm		0.25Ghz	8.970 mw	12.291mA	9.4μm×52.5μm
50nm		0.6Ghz	6.229mw	5.341mA	4.7μm×26.3μm
35nm		0.9Ghz	4.77mw	4.358mA	3.76 μm×18.6μm

Table-II Power and Area analysis for various CMOS processor utilizing variable clock and leakage controller

CMOS Processor	No. of Transistors	Clock Frequency	Power	Leakage Current	Area of logic network
0.12μm	1114	0.51Ghz	7.422mw	5.9mA	127.2μm×1999.6μm
0.25 μm		0.5Ghz	2.518mw	3.847mA	26.5μm ×208.3μm
90nm		0.25Ghz	2.648 mw	1.513mA	10.6μm×83.3μm
50nm		0.6Ghz	0.56mw	0.758mA	5.3μm×41.7μm
35nm		0.9Ghz	0.93mw	1.210mA	4.42 μm×33.32μm

7. CONCLUSION

This paper presents an efficient variable clock and leakage controller .Initially, the power model analysis for various CMOS processor utilizing data activity is established. Subsequently, variable clock and lookup table based leakage controller is tested and power and area analysis for various CMOS processor is performed. The method makes it possible to estimate the power consumption of a processor based on transistor count and data active lines. A few verifications with various CMOS processor indicate that the power models attached with CMOS processor give reasonable results. Variable clock rate controller provides 30% of power reduction and 16% of leakage current reduction with minimum area overhead for controller circuit. The performance of CMOS processor is not degraded due to variable clock selection based on data activity. Therefore using variable clock rate and power model controller proposes a practical and efficient implementation of logic network.

8. REFERENCES

- [1] Ying Teng and BarisTaskin 2015, ROA-Brick Topology for Low-Skew Rotary Resonant Clock Network Design, *IEEE Transactions on very large scale Integration (VLSI) Systems*, 23,11, (NOVEMBER 2015),2519-2530
- [2] Pierre-Emmanuel Gaillardon, Xifan Tang, Gain Kim, and Giovanni De Micheli, 2015, A Novel FPGA Architecture Based on Ultrafine Grain Reconfigurable Logic Cells, *IEEE Transactions on very large scale Integration (VLSI) Systems*, 23, 10, (OCTOBER 2015), 2187-2197.
- [3] JosepRius,2015, Supply Noise and Impedance of On-Chip Power Distribution Networks in ICs With Non uniform Power Consumption and Interblock Decoupling Capacitors, *IEEE Transactions on very large scale Integration (VLSI) Systems*, 23, 6, (JUNE 2015.), 993-1004.
- [4] Guoyue Jiang, Zhaolin Li, Fang Wang, and Shaojun Wei,2015, A Low-Latency and Low-Power Hybrid Scheme for On-Chip Networks,*IEEE Transactions on very large scale Integration (VLSI) Systems*, 23, 4,(APRIL 2015), 664-677.
- [5] Xuan Wang, Xiaowen Wu, Zhehui Wang, 2015, Actively Alleviate Power Gating-Induced Power/Ground Noise Using Parasitic Capacitance of On-Chip Memories in MPSoC, *IEEE Transactions on very large scale Integration (VLSI) Systems*, VOL. 23, NO. 2, Pages: 266-279, FEBRUARY 2015.
- [6] YiciCai, Chao Deng, Qiang Zhou, Hailong Yao, FeifeiNiu, and Cliff N. Sze, 2015, Obstacle-Avoiding and Slew-Constrained Clock Tree Synthesis With Efficient Buffer Insertion,*IEEE Transactions on very large scale Integration (VLSI) Systems*,23,1,(JANUARY 2015),142-155.
- [7] Juan Núñez, María J. Avedillo, and José M. Quintana,2014, Experimental Validation of a Two-Phase Clock Scheme for Fine-Grained Pipelined Circuits Based on Monostable to Bistable Logic Elements , *IEEE Transactions on very large scale Integration (VLSI) Systems*,22,10, (OCTOBER 2014), 2238-2242.
- [8] Kyongsu Lee, and Jae-Yoon Sim, 2014, Half-Rate Clock-Embedded Source Synchronous Transceivers in 130-nm CMOS , *IEEE Transactions on very large scale Integration (VLSI) Systems*, 22, 10,(OCTOBER 2014), 2093-2102.
- [9] Aida Todri-Sanial, SandipKundu, Patrick Girard, AlbertoBosio, Member, Luigi Dilillo, and Arnaud Virazel,2014,Globally Constrained Locally Optimized 3-D Power Delivery Networks,*IEEE Transactions on very large scale Integration (VLSI) Systems*, 22, 10, (OCTOBER 2014), 2131-2144.
- [10] Li Li, Yinghai Lu, and Hai Zhou, 2014, Optimal and Efficient Algorithms for Multidomain Clock Skew Scheduling, *IEEE Transactions on very large scale Integration (VLSI) Systems*, 22, 9, (SEPTEMBER 2014) 1888-1897.
- [11] Jatin N. Mistry, James Myers, Bashir M. Al-Hashimi, Fellow, David Flynn, John Biggs and Geoff V. Merrett, 2014, Active Mode Subclock Power Gating, *IEEE Transactions on very large scale Integration (VLSI) Systems*, 22, 9,(SEPTEMBER 2014),1898-1908.
- [12] Sumeet S. Kumar, Arnica Aggarwal, RadhikaSanjeevJagtap, Amir Zjajo, and Rene van Leuken,2014, System Level Methodology for Interconnect Aware and Temperature Constrained Power Management of 3-D MP-SOCs*IEEE Transactions on very large scale Integration (VLSI) Systems*, 22, 7, (JULY 2014),1606-1619.

- [13] Yoshiro Riho and Kazuo Nakazato, 2014, Partial Access Mode: New Method for Reducing Power Consumption of Dynamic Random Access Memory, *IEEE Transactions on very large scale Integration (VLSI) Systems*, 22, 7, (JULY 2014), 1461-1469.
- [14] Inhak Han and Youngsoo Shin, 2014, Simplifying Clock Gating Logic by Matching Factored Forms , *IEEE Transactions on very large scale Integration (VLSI) Systems*, 22, 6, (JUNE 2014), 1338-1349.
- [15] Ya-Ting Shyu, Jai-Ming Lin, Chun-Po Huang, Cheng-Wu Lin, Ying-Zu Lin, and Soon-Jyh Chang, 2013, Effective and Efficient Approach for Power Reduction by Using Multi-Bit Flip-Flops, *IEEE Transactions on very large scale Integration (VLSI) Systems*, 21, 4, (APRIL 2013), 624- 635.
- [16] Palkesh Jain and Ankit Jain, 2012, Accurate Current Estimation for Interconnect Reliability Analysis, *IEEE Transactions on very large scale Integration (VLSI) Systems*, 20, 9, (SEPTEMBER 2012), 1634- 1644.
- [17] Ali Peiravi and Mohammad Asyaei, 2007, Current-Comparison-Based Domino: New Low-Leakage High-Speed Domino Circuit for Wide Fan-In Gates, *IEEE transactions on computer-aided design of integrated circuits and systems*, 26, 7, (JULY 2007), 1246-1255.
- [18] Vishal Khandelwal, and Ankur Srivastava, 2007, Leakage Control through Fine-Grained Placement and Sizing of Sleep Transistors, *IEEE transactions on computer-aided design of integrated circuits and systems*, 26, 7, (JULY 2007), 1246-1255.

An online task placement algorithm using Hilbert curve for a partially reconfigurable field programmable gate array

Senoj Joseph

Department of ECE
Sri Krishna College of Technology
Coimbatore, 641042, India

K. Baskaran

Department of CSE
Government College of Technology
Coimbatore, 641013, India

Abstract— With the arrival of partial reconfiguration technology, modern FPGAs support tasks that can be loaded in (removed from) the FPGA individually without interrupting other tasks already running on the same FPGA. Many online task placement algorithms designed for such partially reconfigurable systems have been proposed to provide efficient and fast task placement. A new approach for online placement of modules on reconfigurable devices, by managing the free space using a run-length based representation. This representation allows the algorithm to insert or delete tasks quickly and also to calculate the fragmentation easily. In the proposed FPGA model the CLBs are numbered according to Hilbert space filling curve model. The search algorithm will quickly identify a placement for the incoming task based on first fit mode or a fragmentation aware best Fit mode. Simulation experiments indicate that proposed techniques result in low ratio of task rejection and high FPGA utilization compared to existing techniques

Keywords— *Partial Reconfiguration; Task Placement; Free Space Management; Hilbert Curve; FPGA; Task Scheduling*

I. INTRODUCTION

Reconfigurable devices with partial reconfiguration capabilities allow multitasking applications on a single chip. Embedded applications like cryptography, video communication, image processing etc. can exploit this capability. Efficient placement and scheduling algorithm can improve FPGA resources utilization and overall execution time of applications.

One of the most interesting problems is to decide where to locate the bitmap of a new task in the FPGA when it must be run. A data structure is required to keep track of available free area and the algorithm must find out the best location for the arriving task, trying to use the reconfigurable area as efficiently as possible. In online placement system, due to dynamic addition and deletion of tasks, the empty area of FPGA becomes highly fragmented and FPGA area cannot be utilized efficiently. In this study a new data structure based on one dimension run-length encoding is developed to manage the empty area.

Copyright: '978-1-4799-8641-5/15/\$31.00©2015 IEEE'

Using this data structure placement algorithm can locate suitable location to place the incoming task quickly. A new fragmentation metric gives an indication of continuity of free space. The FPGA surface is modeled by a matrix coded according to Hilbert curve. The results show significant improvement over placement using well known algorithms like Bottom left, 2D adjacency based placement, Least interference fit technique and C Look algorithm.

This study is organized as follows: Section 2 presents an overview of problem of Scheduling and Placement in Dynamic Reconfigurable devices. A brief review of various placement and scheduling techniques are given in Section 3. In section 4, a new technique called Hilbert curve based placement is proposed. Section 5 describes about the experimental setup made for performance analysis. Results and discussion are presented in section 6, followed by conclusions.

II. SYSTEM MODEL

The proposed online placement system model is as shown in Fig. 1 which consists of Host CPU and partially reconfigurable FPGA. The reconfigurable resources in FPGA are a set of CLB organized in a two dimensional array. The placement module running on the host CPU consists of scheduler, placer and loader. The scheduler determines which of the tasks in the module library should be loaded and executed next. The placer will manage free space and find out optimum placement for the task. The loader loads the configuration data of tasks in the FPGA. When a task completes the resources occupied by it will be released.

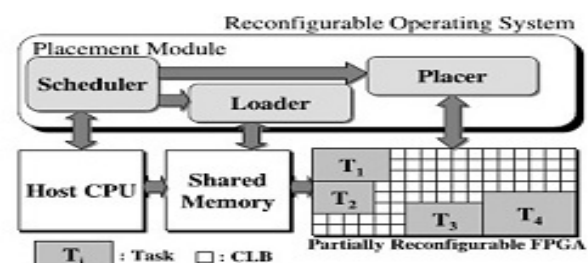


Fig. 1. System model

The system assumes that the tasks arrive online, queued and placed in arrival order. As long as free area is available in the FPGA the incoming task will be placed on an unoccupied area on the FPGA. If there is no free space and the task cannot be delayed then the task is rejected. A good placement algorithm should reduce rejection rate.

The tasks are non-preemptive. Once a task is loaded onto the FPGA, it runs to termination. The tasks should be independent without any precedence constraints. These task parameters are defined as: for a task $t_i = (h_i, w_i, a_i, s_i, d_i, x_i, y_i)$, h_i and w_i represent its height and width respectively and are measured in number of cells, a_i , s_i and d_i are the task arrival time, execution time and deadline time. The rectangular area assigned to the task by its top left corner (x_i, y_i) where x_i : row number and y_i : column number. The size, arrival time, execution time and deadline are uniformly distributed in a predefined region and a-priori unknown.

III. RELATED WORKS

An algorithm for managing free space by keeping track of non-overlapping rectangles is proposed in [1]. The main disadvantage is that the number of empty rectangles produced quickly increases with more task insertions. This can lead to some tasks being rejected even though there is enough space to accommodate them but this space is divided between two non-overlapping rectangles. To solve this problem, they presented the idea of allowing overlapping of the empty rectangles, specifically overlapping maximal empty rectangles MERs. For n tasks, we can have $O(n)$ non-overlapping rectangles and in the case of MERs we can have $O(n^2)$ rectangles.

Reference [13] proposed three partition algorithms based on Bazargan method: Enhanced Bazargan, on the fly and enhanced on the fly. The third is based on a 2D hashing table to find a feasible task placement with a run time complexity of $O(1)$, but they did not account for reconfiguration time and also they did not account for the update time needed to update the hashing table.

Reference [2] proposed Horizontal line algorithm in which two horizontal lines are used: one above and another below the placed tasks. They also presented a free space management based on contour of union of rectangles algorithm. Staircase algorithm was suggested by [7] for finding the maximal empty rectangles. Bottleneck is time for constructing staircase and finding MERs. Vertex lists was used to store free space [11] where each vertex is a possible location for an input task. Module connectivity to the remainder of the system is taken into account in [12]. Scan line algorithm was proposed by [4]. But finding maximum key elements and MER is time consuming. An intelligent merging technique to speed up Bazargan algorithm without losing its placement quality was proposed in [9]. It is a combination of three techniques selected based on the task characteristics. The techniques are: Merge only if needed, partial merging and direct combine. Reference [5] proposed an algorithm which packs tasks densely called 2D and 3D adjacency method. A C Look and CSAF method was proposed in [8].

IV. PROPOSED TECHNIQUE

The design of multidimensional access methods is difficult compared to one-dimensional cases because there is no total ordering that preserves spatial locality. Since it is preferred to fetch a set of consecutive disk blocks rather than a randomly scattered set to reduce additional seek time, it is desirable that objects close together in a multidimensional attribute space also be close together in the one-dimensional space.

Sophisticated mapping functions have been proposed in the literature. One, based on interleaving bits from the coordinates, which is called z-ordering was proposed. By interleaving bits we get another curve called gray code curve. A third method, based on the Hilbert curve has been proposed in literature. Under most circumstances the mapping based on Hilbert space-filling curve outperforms the others therefore in this proposed work we use Hilbert curve. It have been shown in [10] that in 2-dimensional space, Hilbert curve achieves better clustering than z-curve; the number of clusters for Hilbert curve is one fourth of the perimeter of a query rectangle, while that of z-curve is one third of the perimeter plus two thirds of the side length of the rectangle in the unfavoured direction. Fig. 2 shows the steps in Hilbert space filling curve.

In this method the FPGA area has been labeled in Hilbert curve order. A novel data structure called run-length matrix has been introduced to describe the target area. In the Fig. 3 the shaded area indicates task already placed. The free area can be described using run-length matrix as shown below:

$$\text{Runlen} = \{(8, 24), (36, 8), (52, 12)\}$$

If it is not able to find a candidate it will to obtain a location which is a multiple of 8 and selected region can be represented by two regions of 8 cells and so on. In order to avoid checking the same place again and again the checked locations are stored. Once a probable location is obtained then it has to extract an region of width and height equivalent to incoming task (in this example 4x4) containing the probable candidate location. The search algorithm will be based on location and identifying the direction of loop in Hilbert curve. Let FPGA (r, c) be the location (in Hilbert let it be X) of the probable candidate, where r and c indicates row and column of the CLB. Loop direction can be explored by checking the position of $X+1$ and $X-1$ using a look up Hilbert matrix.

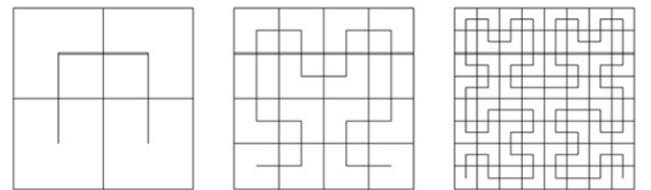


Fig. 2. Steps in Hilbert space filling curves (a) First step (b) Second step (c) Third step

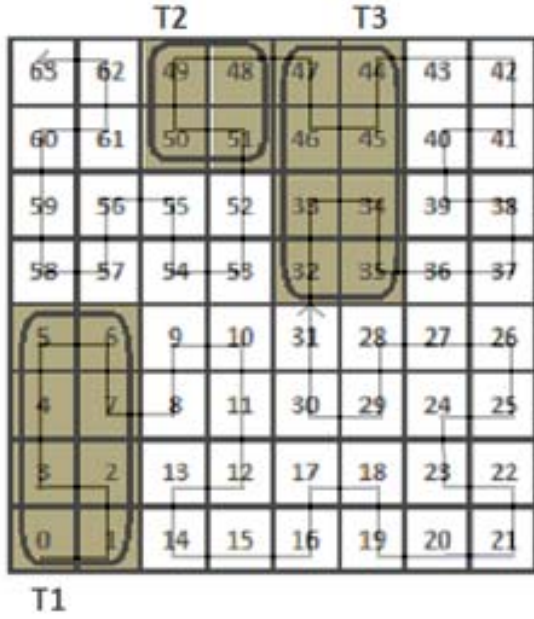


Fig. 3. FPGA with some tasks already placed

Based on this information a block of CLBs are selected according to the required height and width of incoming task. Let T, R, L, B be top, right, left and bottom neighbors of X as shown in Fig. 4. Coordinates are mentioned below each. There are four types of loop. C loop, inverted C loop, U loop and inverted U loop. Each loop will have an entry which can be vertically or horizontally. For the candidate location we have to identify the type of loop and its entry. Let X is the candidate position. By checking the coordinates of X+1 and X+3 we can identify the shape of loop. By checking coordinate of X-1 direction of entry can also be identified. Suppose the candidate position is 8. Keep the mask on top of the FPGA area such that the center of the mask overlaps the candidate position. If the positions of 9 is at T and that of 7 is at L, then the loop will be of inverted U loop with horizontal entry as shown in Fig. 5. Since the task is having height 4 algorithm extracts all possible 4x4 regions using a sliding window of size 4x4 moved vertically and containing search location 8. For location 8 it finds two such regions. The regions are having bottom left corner 8 and 14 respectively. Next another function will arrange the regions in to run-lengths and give it to Addtask routine. For region with bottom left corner 14 it gives run-length as $cblk = \{(8, 12), (28, 4)\}$. Addtask will find out whether it can place the task there.

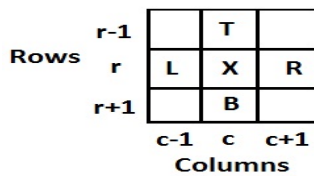


Fig. 4. Notations to identify loops

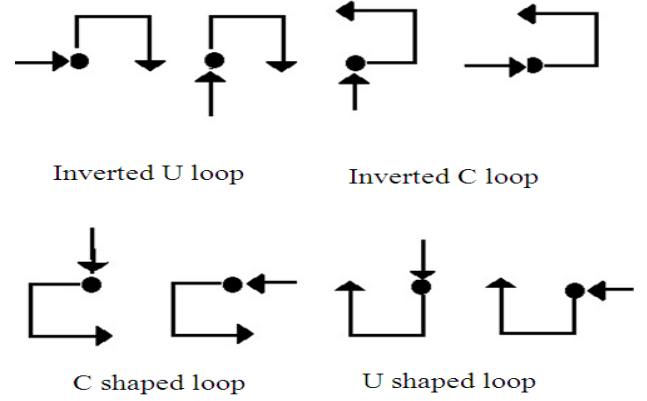


Fig. 5. Various loops occurring in Hilbert curve

If the required regions are occupied then the Addtask routine will fail. If it is a vertical entry case the algorithm proceed in same manner but sliding is done in the horizontal direction such that region include the candidate location. In the example considered if an incoming task T5 with width and height, 4 and 4 respectively. It finds location 8 according to algorithm. The function *hilsen16v1a* will return the blocks to be removed as $cblk = \{(8,12),(28,4)\}$. This list is used to adjust the run-length matrix. The updated run-length matrix will be as shown:

$$Runlen = \{(20,8),(36,8),(52,12)\}$$

When the task T₁ placed at position 0 get expired. Here again we find the blocks to be removed. $Cblk = \{(0,8)\}$. The run-length matrix will be updated as follows $Runlen = \{(0,8),(20,8),(36,8),(52,12)\}$. The status after removing task T₁ is shown in Fig. 6.

In algorithms based on area matrix methods whenever a new task is added or deleted the cells have to be recalculated. This takes considerable amount of time. The run-length will be smaller in size (worst case will be one eight of the number of CLB's) and hence less number of entries only need to be checked. Updating the run-length is also having less complexity.

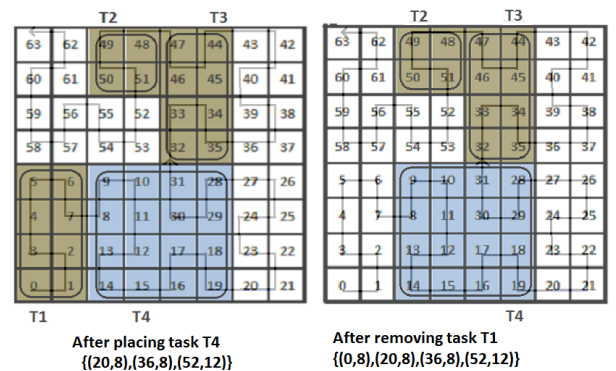


Fig. 6. Insertion of Task T4 and deletion of task T1

The quality of placement algorithm can be improved by finding all feasible solutions and then selecting one based on fragmentation. Best fit find the fragmentation index for all the feasible solutions and place the task in a position that reduces the resulting fragmentation. Due to the run-length representation we make use of a new method to measure continuity of free space. Compared to other methods proposed in literature this is faster and give better results. Fragmentation is calculated using the method given by Gehr and Schneider (2009) as in [6] :

$$F = 1 - \frac{\sum_{i=1}^n fi^p}{(\sum_{i=1}^n fi)^p} \quad p = 1, 2, \dots, n \quad (1)$$

Here p is taken as 2. If the entire space is free then fragmentation will be 0. In worst case of checkerboard pattern it will be almost 1. First fit method tries to place task in the first available location that can accommodate the incoming task. Best fit tries to fix the task in a place which reduces the overall fragmentation. It doesn't guarantee optimal result because it is a heuristic and the future inputs are unpredictable.

V. EXPERIMENTAL SETUP

Simulation framework has been done using Matlab 7.8 running on 2.2 GHz Intel core i3 processor. The simulation is done using randomly generated data for evaluating the algorithm. This has been done in the past because it is impossible to generate real data for future technological advancement. In this section we present two methods: the first one is a fast placement and another fragmentation aware placement technique. These techniques are compared with standard placement techniques like Bottom left, 2D adjacency based placement, Least interference fit technique and Clook algorithm. Bottom left is a classical bin packing algorithm which places the incoming task first empty slot available starting from bottom left corner of FPGA. 2D adjacency based technique choose the location for the incoming tasks to make tasks placed "densely", in order to have larger continuous free area remains. The 2D-Adjacency of a Candidate Cell equals to the number of adjoining tasks/boundaries of the incoming task if the Base Cell of the incoming task is placed here. Least interference technique will select a location which minimize the number of columns disturbed to minimize the number of running tasks getting halted while reconfiguration. Clook method is explained in Lee et al. (2010).

In order to evaluate the effectiveness of algorithm simulation is performed for an FPGA with 16x16 CLB. This model is adopted because the previous studies most relevant to this work used FPGA of similar size for their simulations and the space filling curve works on surface with size power of two. Sixty sets of 500 tasks each are randomly generated for each experimental environment and the results shown in next section are the average over these sets. The height and width of the tasks are chosen randomly between 1 and a maximum value of 8 CLBs. Lifetime of the tasks is generated randomly between 1 and 500 time units. Delay between two consecutive tasks is also chose between 1 and user defined L time units. The workload can be controlled using different upper bound L. A smaller L means that the tasks arrivals are more frequent and

FPGA area utilization is higher. All parameters are assigned by sampling a uniform random distribution function in their respective validity intervals. It is not within the scope of this study to evaluate a full-fledged online scheduling algorithm which includes admission control, priority assignment. Instead a simple scheduling algorithm which can place task from a waiting list is used.

The following assumptions are used in this work. The tasks are independent and preemptive. Preemptive task is one if started cannot be stopped before its expiry. Due to this relocation of tasks is also not permitted. Since the tasks are independent they can be scheduled in any order. Rotation of task is not used. The following parameters are measured to test the effectiveness of the proposed algorithm. Suppose during the simulation interval (0, T), N tasks arrived and n tasks were rejected. For a reconfigurable area of size W*H.

Average task rejection ratio: A task may be rejected placement if sufficient contiguous area is not available currently and it if cannot meet its deadline if scheduled at a later time. Average task rejection ratio is the ratio of number of tasks rejected to total number of tasks.

Total waiting time for tasks: if the online placement cannot find a feasible space the task will be added to a waiting list. When some task that is currently running completes, new space will be created, the waiting list will be examined to place tasks that can meet the deadline.

Average area utilization is calculated as shown in (2)

$$\frac{\sum_{i=1}^{N-n} Ei * Wi * Hi}{T * W * H} \quad (2)$$

VI. RESULTS AND DISCUSSION

In this section, snapshot of Simulation results of output at particular instance is shown in Fig. 7. The colored boxes correspond to tasks that are currently running. Task that have completed is not shown. The white region indicates empty region which is already got fragmented due to placement and removal of tasks.

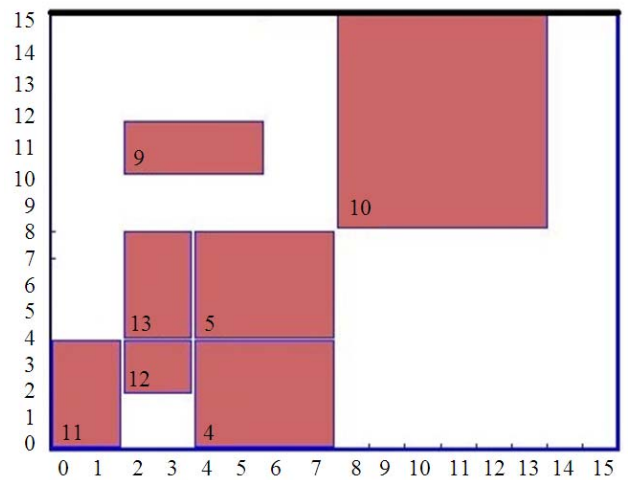


Fig. 7. FPGA status after placing the 13th task

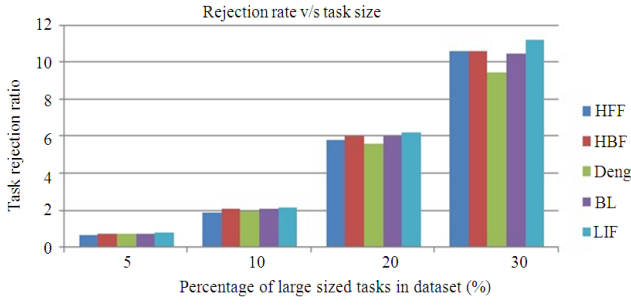


Fig. 8. Variation in rejection rate with respect to percentage of large sized tasks in dataset

In the next experiment the inter-task arrival time is varied from 5 to 20% of execution time. The rejection rates are plotted in Fig. 9. In order to examine the impact of deadline on the performance we repeated the experiments with different values of slack. The deadline is calculated as sum of arrival time, execution time and slack. The impact of deadline on rejection rate is shown in Fig. 10. The Table 1 gives the performance of various algorithms. The experiment is repeated with skewed probability distribution of task width and height to study the impact of task size on placement quality. The results are shown in Fig. 8.

The results shows that the performance of the proposed placement matches with conventional method for all cases. The rejection rate was more for large sized task as expected. The rejection rate increases with decrease in inter-task arrival time range. When tasks arrive in quick succession then more number of tasks will be running on the FPGA leaving less room for the newly arrived task. When deadline is tight then more tasks get rejected. If deadline is loose then tasks can wait till their ALAP time and get placed whenever a free slot is available. When slack becomes very large then none of the tasks get rejected. Other results show that average utilization for Hilbert method is marginally better with lesser execution time than others. From Table 1 even though BL, Deng and LIF seem to be faster, their speed reduces when the size of the FPGA is increased. CLook has more execution time but its rejection rate performance is better than others. The proposed methods have rejection rate performance equal to CLook algorithm with faster execution time.

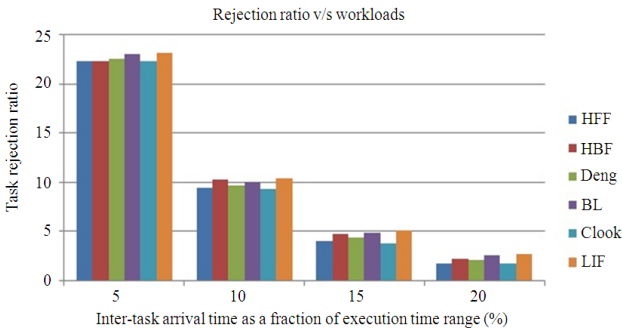


Fig. 9. Rejection ratio for various loads



Fig. 10. Rejection ratio varies with slack

VII. CONCLUSIONS

In this study a new approach for scheduling and placement of task on a dynamic reconfigurable device based on Hilbert space filling curve method is being presented with the goal of minimizing task rejection ratio and increasing FPGA utilization. The free space is managed as one dimensional run-length based representation. Also a new method to find the fragmentation is used.

TABLE I. OTHER PERFORMANCE METRICS

10x500 10%large even I/U/S 8/100/20	Average utilization factor	Average waiting time	Program execution time
BL	48.15	39.10	69.49ms
Deng	47.72	26.80	176.80ms
LIF	47.29	40.10	202.20ms
Clook	48.62	31.60	1023.00ms
HFF	47.84	34.80	530.00ms
HBF	47.45	44.10	694.00ms

ACKNOWLEDGMENT

Researchers thank the SKCT management and acknowledge the immense help received from the scholars whose articles are cited and included in references of this manuscript. The authors are also grateful to authors/editors/publishers of all those articles, journals and books from where the literature for this article has been reviewed and discussed.

REFERENCES

- [1] A. Ahmadiania, C. Bobda, M. Bednara and J. Teich, "A new approach for on-line placement on reconfigurable devices," Proceedings of the 18th International Parallel and Distributed Processing Symposium, IEEE Xplore Press, pp: 134-140, April. 26-30, 2004.
- [2] A. Ahmadiania, C. Bobda, S.P. Fekete, J. Teich and J.V.G.Veen, "Optimal free space management and routing conscious dynamic placement for reconfigurable devices," IEEE Trans. Comput., 56: pp. 673-680, 2007.
- [3] K. Bazargan, R. Kastner and M. Sarrafzadeh, "Fast template placement for reconfigurable computing systems," Proceedings of the IEEE Design Test-Special Reconfigurable Computing, (SRC' 00), pp: 68-83, 2000.

- [4] J. Cui, Q. Deng, X.Q. He and Z. Gu, "An efficient algorithm for online management of 2D area of partially reconfigurable FPGAs," Proceedings of the 7th IEEE International Conference Design, Automation and Test in Europe Conference Exhibition, IEEE Xplore Press, pp: 1-6, Apr. 6-20, 2007.
- [5] Q. Deng, F. Kong, N. Guan, L. Mingsong and W. Yi, "On-line placement of real-time tasks on 2D partially run-time reconfigurable FPGAs. Proceedings of the 5th IEEE International Symposium Embedded Computing, IEEE Xplore Press, Beijing, pp: 20-25, Oct. 6-8, 2008.
- [6] J. Gehr, and J. Schneider, "Measuring fragmentation of two-dimensional resources applied to advance reservation grid scheduling," Proceedings of the 9th IEEE International Symposium Cluster Computing Grid, IEEE Xplore Press, pp: 276-283, May 18-21, 2009.
- [7] M. Handa, and R. Vemuri, "An efficient algorithm for finding empty space for online FPGA placement. Proceedings of the 41st annual Design Automation Conference, San Diego, pp: 960-965, Jun. 07-11, 2004
- [8] T.Y. Lee, C.C. Hu and C.C. Tsai, "Adaptive free space management of on-line placement for reconfigurable systems," Proceedings of the International Multi-Conference Engineers Computer Scientists, Hong Kong, pp: 322-326 Mar 17-19, 2010.
- [9] T. Marconi, Y. Liu, K. Bertels and G. Gaydadjiev, "Intelligent merging on-line task placement algorithm for partial reconfigurable system," "Proceedings of the 8th Design, Automation and Test in Europe, IEEE Xplore Press, Munich, pp: 1346-1351, Mar. 10-14, 2008.
- [10] B. Moon, H.V. Jagadeesh, C. Faloustos and J.H. Saltz, "Analysis of clustering property of Hilbert space filling curve," IEEE Trans. Know. Data Eng., 2001
- [11] J. Tabero, J. Septian, H. Mecha and D. Mozos, "A Low Fragmentation Heuristic for Task Placement in 2D RTR HW Management," Proceedings of the 14th International Conference field programmable Logic Application, IEEE Xplore Press, Belgium, pp: 241-250, Belgium, Aug. 30-Sep. 1, 2004.
- [12] M. Tomono, M. Nakanishi, S. Yamashita, N. Nakajima and K. Watanabe, "A new approach to online FPGA placement," Proceedings of the 40th Annual Conference Information Sciences Systems, IEEE Xplore Press, Princeton, pp: 145-150, Mar. 22-24, 2006.
- [13] Walder, H., C. Steiger and M. Platzner, "Fast online task placement on FPGAs: Free space partitioning and 2D-hashing," Proceedings of the IEEE International Parallel and Distributed Processing Symposium, IEEE Xplore Press, pp: 178-178, Apr. 22-26, 2003.

Institutional Sign In

Browse

My Settings

Get Help

Subscribe

Advertisement

Advertisement

Conferences > 2018 9th International Confer...

Performance Evaluation of Fault Nodes Using Queue Threshold Based on N-Policy Priority Queueing Model

Publisher: IEEE

6 Author(s)

P. Jayarajan ; R. Maheswar ; G.R. Kanagachidambaresan ; V. Sivasankaran... View All Authors

1
Paper
Citation

30
Full
Text Views

Abstract

Abstract: A major issue in Wireless Sensor Networks (WSNs) is the minimum availability of energy and hence reducing the amount of energy consumed is of greater interest. In WSN, la... [View more](#)

Authors

References

Citations

Keywords

Metrics

More Like This

Metadata

Abstract:

A major issue in Wireless Sensor Networks (WSNs) is the minimum availability of energy and hence reducing the amount of energy consumed is of greater interest. In WSN, large amount of energy is consumed during transmission and failure of nodes in sensor network is common. Here, a novel technique is proposed to reduce the node's energy consumption during data transmission using queue threshold based on N-Policy Priority Queueing Model (PQM) by taking failure of nodes into consideration. A sensor network model is developed analytically to evaluate the performance of the proposed scheme by means of energy consumption and delay by taking node failures into consideration. From the results, it is inferred the average energy consumption savings is about 43% for the optimal threshold value by taking node failures into consideration. Simulations are carried out and the results obtained show that the analytical and simulation results matches thus validating the accuracy of the analytical model.

Published in: 2018 9th International Conference on Computing, Communication and Networking Technologies (ICCCNT)

Date of Conference: 10-12 July 2018

INSPEC Accession Number: 18182237

Date Added to IEEE Xplore: 18 October 2018

DOI: 10.1109/ICCCNT.2018.8494097

ISBN Information:

Publisher: IEEE

Conference Location: Bangalore, India

Advertisement

Authors

References

Citations

Keywords

More Like This

Energy consumption analysis of ZigBee-based energy harvesting wireless sensor networks
2012 IEEE International Conference on Communication Systems (ICCS)
Published: 2012

Minimization of average energy consumption to prolong lifetime of Wireless Sensor Network
2014 IEEE Global Conference on Wireless Computing & Networking (GCWCN)
Published: 2014

[View More](#)

Top Organizations with Patents on Technologies Mentioned in This Article



Advertisement

Photonic crystal with epsilon negative and double negative materials as an optical sensor

Optical and Quantum Electronics

May 2018, 50:222 | Cite as

Article

First Online: 11 May 2018

125

4

Downloads Citations

Abstract

Two ternary photonic crystals are proposed for sensing applications. The first one is composed of an air layer as an analyte sandwiched between two double negative material (DNM) layers whereas the second one consists of an air layer sandwiched between two epsilon negative material (ENM) layers. The transmission spectrum is studied for two different values of the refractive index of the analyte layer with $\Delta n = 0.01$. A specific peak in the transmission spectrum is observed and the wavelength at which the peak occurs is determined. The wavelength shift due to any change in the index of the analyte layer is also determined. The effect of varying the parameters of the DNM and ENM on the sensitivity of the sensor is discussed. It is found that the sensitivity of the structure ENM/air/ENM is much greater than that of the structure DNM/air/DNM and it is estimated as 26 times of the sensitivity of the latter structure.

Keywords

Photonic crystal Epsilon negative materials Double negative materials Sensor

This is a preview of subscription content, [log in](#) to check access.

References

- Abadla, M., Taya, S.A.: Excitation of TE surface polaritons in different structures comprising a left-handed material and a metal. *Optik Int. J. Light Electron. Opt.* **125**, 1401–1405 (2014)
[CrossRef](https://doi.org/10.1016/j.ijleo.2013.08.040) (<https://doi.org/10.1016/j.ijleo.2013.08.040>)
[Google Scholar](http://scholar.google.com) (<http://scholar.google.com>)
 /scholar_lookup?title=Excitation%20of%20TE%20surface%20polaritons%20in%20different%20structures%20comprising%20a%20left-handed%20material%20and%20a%20metal&author=M.%20Abadla&author=SA.%20Taya&journal=Optik%20Int.%20J.%20Light%20Electron.%20Opt.&volume=125&pages=1401-1405&publication_year=2014)
- Awasthi, S.K., Ojha, S.P.: Design of a tunable optical filter by using one-dimensional ternary photonic band gap material. *Prog. Electromagn. Res. M* **4**, 117–132 (2008)
[CrossRef](https://doi.org/10.2528/PIERM08061302) (<https://doi.org/10.2528/PIERM08061302>)
[Google Scholar](http://scholar.google.com) (<http://scholar.google.com>)
 /scholar_lookup?title=Design%20of%20a%20tunable%20optical%20filter%20by%20using%20one-dimensional%20ternary%20photonic%20band%20gap%20material&author=SK.%20Awasthi&author=SP.%20Ojha&journal=Prog.%20Electromagn.%20Res.%20M&volume=4&pages=117-132&publication_year=2008)
- Awasthi, S.K., Malaviya, U., Ojha, S.P.: Enhancement of omnidirectional total-reflection wavelength range by using one dimensional ternary photonic band gap material. *J. Opt. Soc. Am. B* **23**, 2566–2571 (2006)
[ADS](http://adsabs.harvard.edu/cgi-bin/nph-data_query?link_type=ABSTRACT&bibcode=2006JOSAB..23.2566A) (http://adsabs.harvard.edu/cgi-bin/nph-data_query?link_type=ABSTRACT&bibcode=2006JOSAB..23.2566A)
[CrossRef](https://doi.org/10.1364/JOSAB.23.002566) (<https://doi.org/10.1364/JOSAB.23.002566>)
[Google Scholar](http://scholar.google.com) (<http://scholar.google.com>)
 /scholar_lookup?title=Enhancement%20of%20omnidirectional%20total-reflection%20wavelength%20range%20by%20using%20one%20dimensional%20ternary%20photonic%20band%20gap%20material&author=SK.%20Awasthi&author=U.%20Malaviya&author=SP.%20Ojha&journal=J.%20Opt.%20Soc.%20Am.%20B&volume=23&pages=2566-2571&publication_year=2006)
- Banerjee, A.: Enhanced refractometric optical sensing by using one-dimensional ternary photonic crystals. *Prog. Electromagn. Res. PIER* **89**, 11–22 (2009a)
[CrossRef](https://doi.org/10.2528/PIERO8112105) (<https://doi.org/10.2528/PIERO8112105>)
[Google Scholar](http://scholar.google.com) (<http://scholar.google.com>)
 /scholar_lookup?title=Enhanced%20refractometric%20optical%20sensing%20by%20using%20one-dimensional%20ternary%20photonic%20crystals&author=A.%20Banerjee&journal=Prog.%20Electromagn.%20Res.%20PIER&volume=89&pages=11-22&publication_year=2009)
- Banerjee, A.: Enhanced temperature sensing by using one-dimensional ternary photonic band gap structures. *Prog. Electromagn. Res. Lett.* **11**, 129–137 (2009b)
[CrossRef](https://doi.org/10.2528/PIERLO9080101) (<https://doi.org/10.2528/PIERLO9080101>)
[Google Scholar](http://scholar.google.com) (<http://scholar.google.com>)
 /scholar_lookup?title=Enhanced%20temperature%20sensing%20by%20using%2

[one-dimensional%20ternary%20photonic%20band%20gap%20structures&author=A.%20Banerjee&journal=Prog.%20Electromagn.%20Res.%20Lett.&volume=11&pages=129-137&publication_year=2009](#))

Densmore, A., Xu, D.X., Waldron, P., Janz, S., Cheben, P., Lapointe, J., et al.: A silicon-on-insulator photonic wire based evanescent field sensor. *IEEE Photonics Technol. Lett.* **18**, 2520–2522 (2006)

[ADS](#) ([http://adsabs.harvard.edu/cgi-bin/nph-](http://adsabs.harvard.edu/cgi-bin/nph-data_query?link_type=ABSTRACT&bibcode=2006IPTL...18.2520D)

[data_query?link_type=ABSTRACT&bibcode=2006IPTL...18.2520D](#))

[CrossRef](#) (<https://doi.org/10.1109/LPT.2006.887374>)

[Google Scholar](#) (http://scholar.google.com/scholar_lookup?title=A%20silicon-on-insulator%20photonic%20wire%20based%20evanescent%20field%20sensor&author=A.%20Densmore&author=DX.%20Xu&author=P.%20Waldron&author=S.%20Janz&author=P.%20Cheben&author=J.%20Lapointe&journal=IEEE%20Photonics%20Technol.%20Lett.&volume=18&pages=2520-2522&publication_year=2006)

El-Agez, T.M., Taya, S.A.: Theoretical spectroscopic scan of the sensitivity of asymmetric slab waveguide sensors. *Opt. Appl.* **41**, 89–95 (2011)

[Google Scholar](#) (<http://scholar.google.com>

[/scholar_lookup?title=Theoretical%20spectroscopic%20scan%20of%20the%20sensitivity%20of%20asymmetric%20slab%20waveguide%20sensors&author=TM.%20El-Agez&author=SA.%20Taya&journal=Opt.%20Appl.&volume=41&pages=89-95&publication_year=2011](#))

Homola, J., Yee, S.S., Gauglitz, G.: Surface plasmon resonance sensors: review. *Sensors Actuators B* **54**, 3–15 (1999)

[CrossRef](#) ([https://doi.org/10.1016/S0925-4005\(98\)00321-9](https://doi.org/10.1016/S0925-4005(98)00321-9))

[Google Scholar](#) (<http://scholar.google.com>

[/scholar_lookup?title=Surface%20plasmon%20resonance%20sensors%3A%20review&author=J.%20Homola&author=SS.%20Yee&author=G.%20Gauglitz&journal=Sensors%20Actuators%20B&volume=54&pages=3-15&publication_year=1999](#))

Horvath, R., Fricsovszky, G., Pap, E.: Application of the optical waveguide light mode spectroscopy to monitor lipid bilayer phase transition. *Biosensors Bioelectron.* **18**, 415–428 (2003)

[CrossRef](#) ([https://doi.org/10.1016/S0956-5663\(02\)00154-9](https://doi.org/10.1016/S0956-5663(02)00154-9))

[Google Scholar](#) (<http://scholar.google.com>

[/scholar_lookup?title=Application%20of%20the%20optical%20waveguide%20light%20mode%20spectroscopy%20to%20monitor%20lipid%20bilayer%20phase%20transition&author=R.%20Horvath&author=G.%20Fricsovszky&author=E.%20Pap&journal=Biosensors%20Bioelectron.&volume=18&pages=415-428&publication_year=2003](#))

Kriegel, I., Scotognella, F.: Disordered one-dimensional photonic structures composed by more than two materials with the same optical thickness. *Opt. Commun.* **338**, 523–527 (2015)

[ADS](#) ([http://adsabs.harvard.edu/cgi-bin/nph-](http://adsabs.harvard.edu/cgi-bin/nph-data_query?link_type=ABSTRACT&bibcode=2015OptCo.338..523K)

[data_query?link_type=ABSTRACT&bibcode=2015OptCo.338..523K](#))

[CrossRef](#) (<https://doi.org/10.1016/j.optcom.2014.10.045>)

[Google Scholar](#) (<http://scholar.google.com>

[/scholar_lookup?title=Disordered%20one-dimensional%20photonic%20structures%20composed%20by%20more%20than%20two%20materials%20with%20the%20same%20optical%20thickness&author=I.%20Kriegel&author=F.%20Scotognella&journal=Opt.%20Commun.&volume=338&pages=523-527&publication_year=2015](#))

Kullab, H.M., Taya, S.A.: Peak type metal-clad waveguide sensor using negative index materials. *Int. J. Electron. Commun. (AEÜ)* **67**, 905–992 (2013)

[CrossRef](https://doi.org/10.1016/j.aeue.2013.05.012) (<https://doi.org/10.1016/j.aeue.2013.05.012>)

[Google Scholar](http://scholar.google.com) (<http://scholar.google.com>)

[/scholar_lookup?title=Peak%20type%20metal-clad%20waveguide%20sensor%20using%20negative%20index%20materials&author=HM.%20Kullab&author=SA.%20Taya&journal=Int.%20J.%20Electron.%20Commun.%20%28AE%C3%9C%29&volume=67&pages=905-992&publication_year=2013](http://scholar_lookup?title=Peak%20type%20metal-clad%20waveguide%20sensor%20using%20negative%20index%20materials&author=HM.%20Kullab&author=SA.%20Taya&journal=Int.%20J.%20Electron.%20Commun.%20%28AE%C3%9C%29&volume=67&pages=905-992&publication_year=2013))

Kullab, H.M., Taya, S.A.: Transverse magnetic peak type metal-clad optical waveguide sensor. *Optik Int. J. Light Electron. Opt.* **145**, 97–100 (2014)

[CrossRef](https://doi.org/10.1016/j.ijleo.2013.06.029) (<https://doi.org/10.1016/j.ijleo.2013.06.029>)

[Google Scholar](http://scholar.google.com) (<http://scholar.google.com>)

[/scholar_lookup?title=Transverse%20magnetic%20peak%20type%20metal-clad%20optical%20waveguide%20sensor&author=HM.%20Kullab&author=SA.%20Taya&journal=Optik%20Int.%20J.%20Light%20Electron.%20Opt.&volume=145&pages=97-100&publication_year=2014](http://scholar_lookup?title=Transverse%20magnetic%20peak%20type%20metal-clad%20optical%20waveguide%20sensor&author=HM.%20Kullab&author=SA.%20Taya&journal=Optik%20Int.%20J.%20Light%20Electron.%20Opt.&volume=145&pages=97-100&publication_year=2014))

Kullab, H.M., Taya, S.A., El-Agez, T.M.: Metal-clad waveguide sensor using a left-handed material as a core layer. *J. Opt. Soc. Am. B* **29**, 959–964 (2012)

[ADS](http://adsabs.harvard.edu/cgi-bin/nph-data_query?link_type=ABSTRACT&bibcode=2012JOSAB..29..959K) (http://adsabs.harvard.edu/cgi-bin/nph-data_query?link_type=ABSTRACT&bibcode=2012JOSAB..29..959K)

[CrossRef](https://doi.org/10.1364/JOSAB.29.000959) (<https://doi.org/10.1364/JOSAB.29.000959>)

[Google Scholar](http://scholar.google.com/scholar_lookup?title=Metal-clad%20waveguide%20sensor%20using%20a%20left-handed%20material%20as%20a%20core%20layer&author=HM.%20Kullab&author=SA.%20Taya&author=TM.%20El-Agez&journal=J.%20Opt.%20Soc.%20Am.%20B&volume=29&pages=959-964&publication_year=2012) ([http://scholar.google.com/scholar_lookup?title=Metal-clad%20waveguide%20sensor%20using%20a%20left-](http://scholar.google.com/scholar_lookup?title=Metal-clad%20waveguide%20sensor%20using%20a%20left-handed%20material%20as%20a%20core%20layer&author=HM.%20Kullab&author=SA.%20Taya&author=TM.%20El-Agez&journal=J.%20Opt.%20Soc.%20Am.%20B&volume=29&pages=959-964&publication_year=2012)

[handed%20material%20as%20a%20core%20layer&author=HM.%20Kullab&author=SA.%20Taya&author=TM.%20El-Agez&journal=J.%20Opt.%20Soc.%20Am.%20B&volume=29&pages=959-964&publication_year=2012](http://scholar_lookup?title=Metal-clad%20waveguide%20sensor%20using%20a%20left-handed%20material%20as%20a%20core%20layer&author=HM.%20Kullab&author=SA.%20Taya&author=TM.%20El-Agez&journal=J.%20Opt.%20Soc.%20Am.%20B&volume=29&pages=959-964&publication_year=2012))

Kullab, H.M., Qadoura, I.M., Taya, S.A.: Slab waveguide sensor with left-handed material core layer for detection an adlayer thickness and index. *J. Nano Electron. Phys.* **7**, 2039–2041 (2015)

[Google Scholar](http://scholar.google.com) (<http://scholar.google.com>)

[/scholar_lookup?title=Slab%20waveguide%20sensor%20with%20left-handed%20material%20core%20layer%20for%20detection%20an%20adlayer%20thickness%20and%20index&author=HM.%20Kullab&author=IM.%20Qadoura&author=SA.%20Taya&journal=J.%20Nano%20Electron.%20Phys.&volume=7&pages=2039-2041&publication_year=2015](http://scholar_lookup?title=Slab%20waveguide%20sensor%20with%20left-handed%20material%20core%20layer%20for%20detection%20an%20adlayer%20thickness%20and%20index&author=HM.%20Kullab&author=IM.%20Qadoura&author=SA.%20Taya&journal=J.%20Nano%20Electron.%20Phys.&volume=7&pages=2039-2041&publication_year=2015))

Kuswandi, B.: Simple optical fiber biosensor based on immobilized enzyme for monitoring of trace having metal ions. *Anal. Bioanal. Chem.* **376**, 1104–1110 (2003)

[CrossRef](https://doi.org/10.1007/s00216-003-2001-3) (<https://doi.org/10.1007/s00216-003-2001-3>)

[Google Scholar](http://scholar.google.com) (<http://scholar.google.com>)

[/scholar_lookup?title=Simple%20optical%20fiber%20biosensor%20based%20on%20immobilized%20enzyme%20for%20monitoring%20of%20trace%20having%20metal%20ions&author=B.%20Kuswandi&journal=Anal.%20Bioanal.%20Chem.&volume=376&pages=1104-1110&publication_year=2003](http://scholar_lookup?title=Simple%20optical%20fiber%20biosensor%20based%20on%20immobilized%20enzyme%20for%20monitoring%20of%20trace%20having%20metal%20ions&author=B.%20Kuswandi&journal=Anal.%20Bioanal.%20Chem.&volume=376&pages=1104-1110&publication_year=2003))

Pendry, J.B., Holden, A.J., Stewart, W.J., Youngs, I.: Extremely low frequency plasmons in mettalic mesostructures. *Phys. Rev. Lett.* **76**, 4773–4776 (1996)

[ADS](http://adsabs.harvard.edu/cgi-bin/nph-data_query?link_type=ABSTRACT&bibcode=1996PhRvL..76.4773P) (http://adsabs.harvard.edu/cgi-bin/nph-data_query?link_type=ABSTRACT&bibcode=1996PhRvL..76.4773P)

[CrossRef](https://doi.org/10.1103/PhysRevLett.76.4773) (<https://doi.org/10.1103/PhysRevLett.76.4773>)

Google Scholar (<http://scholar.google.com>)

/scholar_lookup?title=Extremely%20low%20frequency%20plasmons%20in%20metamaterial%20mesostructures&author=JB.%20Pendry&author=AJ.%20Holden&author=WJ.%20Stewart&author=I.%20Youngs&journal=Phys.%20Rev.%20Lett.&volume=76&pages=4773-4776&publication_year=1996)

Pendry, J.B., Holden, A.J., Robbins, D.J., Stewart, W.J.: Magnetism from conductors and enhanced nonlinear phenomena. *IEEE Trans. Microw. Theory Tech.* **47**, 2075–2090 (1999)

ADS (http://adsabs.harvard.edu/cgi-bin/nph-data_query?link_type=ABSTRACT&bibcode=1999ITMTT..47.2075P)

CrossRef (<https://doi.org/10.1109/22.798002>)

Google Scholar (<http://scholar.google.com>)

/scholar_lookup?title=Magnetism%20from%20conductors%20and%20enhanced%20nonlinear%20phenomena&author=JB.%20Pendry&author=AJ.%20Holden&author=DJ.%20Robbins&author=WJ.%20Stewart&journal=IEEE%20Trans.%20Microw.%20Theory%20Tech.&volume=47&pages=2075-2090&publication_year=1999)

Ramanujam, N.R., Joseph Wilson, K.S.: Optical properties of silver nanocomposites and photonic band gap—pressure dependence. *Opt. Commun.* **368**, 174–179 (2016)

ADS (http://adsabs.harvard.edu/cgi-bin/nph-data_query?link_type=ABSTRACT&bibcode=2016OptCo.368..174R)

CrossRef (<https://doi.org/10.1016/j.optcom.2016.02.018>)

Google Scholar (<http://scholar.google.com>)

/scholar_lookup?title=Optical%20properties%20of%20silver%20nanocomposites%20and%20photonic%20band%20gap%E2%80%94pressure%20dependence&author=NR.%20Ramanujam&author=KS.%20Joseph%20Wilson&journal=Opt.%20Commun.&volume=368&pages=174-179&publication_year=2016)

Sandhu, S., Fan, S., Yanik, M., Povinelli, M.: Advances in theory of photonic crystal. *J. Light Wave Technol.* **24**, 4493–4501 (2006)

ADS (http://adsabs.harvard.edu/cgi-bin/nph-data_query?link_type=ABSTRACT&bibcode=2006JLwT...24.4493F)

CrossRef (<https://doi.org/10.1109/JLT.2006.886061>)

Google Scholar (<http://scholar.google.com>)

/scholar_lookup?title=Advances%20in%20theory%20of%20photonic%20crystal&author=S.%20Sandhu&author=S.%20Fan&author=M.%20Yanik&author=M.%20Povinelli&journal=J.%20Light%20Wave%20Technol.&volume=24&pages=4493-4501&publication_year=2006)

Shelby, R.A., Smith, D.R., Schultz, S.: Experimental verification of a negative index of refraction. *Science* **292**, 77–79 (2001)

ADS (http://adsabs.harvard.edu/cgi-bin/nph-data_query?link_type=ABSTRACT&bibcode=2001Sci...292...77S)

CrossRef (<https://doi.org/10.1126/science.1058847>)

Google Scholar (<http://scholar.google.com>)

/scholar_lookup?title=Experimental%20verification%20of%20a%20negative%20index%20of%20refraction&author=RA.%20Shelby&author=DR.%20Smith&author=S.%20Schultz&journal=Science&volume=292&pages=77-79&publication_year=2001)

Singh, V., Kumar, D.: Theoretical modeling of a metal-clad planar waveguide based biosensors for the detection of pseudomonas-like bacteria. *Prog. Electromagn. Res. M* **6**, 167–184 (2009)

[CrossRef \(https://doi.org/10.2528/PIERM09021701\)](https://doi.org/10.2528/PIERM09021701)

[Google Scholar \(http://scholar.google.com\)](http://scholar.google.com)

/scholar_lookup?title=Theoretical%20modeling%20of%20a%20metal-clad%20planar%20waveguide%20based%20on%20biosensors%20for%20the%20detection%20of%20pseudomonas-like%20bacteria&author=V.%20Singh&author=D.%20Kumar&journal=Prog.%20Electromagn.%20Res.%20M&volume=6&pages=167-184&publication_year=2009)

Taya, S.A.: Slab waveguide with air core layer and anisotropic left-handed material claddings as a sensor. *Opto-Electron. Rev.* **22**, 252–257 (2014)

[ADS \(http://adsabs.harvard.edu/cgi-bin/nph-](http://adsabs.harvard.edu/cgi-bin/nph-data_query?link_type=ABSTRACT&bibcode=2014OERv...22..252T)

[data_query?link_type=ABSTRACT&bibcode=2014OERv...22..252T\)](http://adsabs.harvard.edu/cgi-bin/nph-data_query?link_type=ABSTRACT&bibcode=2014OERv...22..252T)

[CrossRef \(https://doi.org/10.2478/s11772-014-0201-3\)](https://doi.org/10.2478/s11772-014-0201-3)

[Google Scholar \(http://scholar.google.com\)](http://scholar.google.com)

/scholar_lookup?title=Slab%20waveguide%20with%20air%20core%20layer%20and%20anisotropic%20left-handed%20material%20claddings%20as%20a%20sensor&author=SA.%20Taya&journal=Opto-Electron.%20Rev.&volume=22&pages=252-257&publication_year=2014)

Taya, S.A.: Dispersion properties of lossy, dispersive, and anisotropic left-handed material slab waveguide. *Optik Int. J. Light Electron. Opt.* **126**, 1319–1323 (2015a)
[CrossRef \(https://doi.org/10.1016/j.ijleo.2015.04.013\)](https://doi.org/10.1016/j.ijleo.2015.04.013)

[Google Scholar \(http://scholar.google.com\)](http://scholar.google.com)

/scholar_lookup?title=Dispersion%20properties%20of%20lossy%20and%20dispersive%20and%20anisotropic%20left-handed%20material%20slab%20waveguide&author=SA.%20Taya&journal=Optik%20Int.%20J.%20Light%20Electron.%20Opt.&volume=126&pages=1319-1323&publication_year=2015)

Taya, S.A.: P-polarized surface waves in a slab waveguide with left-handed material for sensing applications. *J. Magn. Mater.* **377**, 281–285 (2015b)

[ADS \(http://adsabs.harvard.edu/cgi-bin/nph-](http://adsabs.harvard.edu/cgi-bin/nph-data_query?link_type=ABSTRACT&bibcode=2015JMMM...377..281T)

[data_query?link_type=ABSTRACT&bibcode=2015JMMM...377..281T\)](http://adsabs.harvard.edu/cgi-bin/nph-data_query?link_type=ABSTRACT&bibcode=2015JMMM...377..281T)

[CrossRef \(https://doi.org/10.1016/j.jmmm.2014.10.126\)](https://doi.org/10.1016/j.jmmm.2014.10.126)

[Google Scholar \(http://scholar.google.com/scholar_lookup?title=P-](http://scholar.google.com/scholar_lookup?title=P-polarized%20surface%20waves%20in%20a%20slab%20waveguide%20with%20left-handed%20material%20for%20sensing%20applications&author=SA.%20Taya&journal=J.%20Magn.%20Mater.&volume=377&pages=281-285&publication_year=2015)

[polarized%20surface%20waves%20in%20a%20slab%20waveguide%20with%20left-handed%20material%20for%20sensing%20applications&author=SA.%20Taya&journal=J.%20Magn.%20Mater.&volume=377&pages=281-285&publication_year=2015\)](http://scholar.google.com/scholar_lookup?title=P-polarized%20surface%20waves%20in%20a%20slab%20waveguide%20with%20left-handed%20material%20for%20sensing%20applications&author=SA.%20Taya&journal=J.%20Magn.%20Mater.&volume=377&pages=281-285&publication_year=2015)

Taya, S.A.: Theoretical investigation of slab waveguide sensor using anisotropic metamaterials. *Opt. Appl.* **45**, 405–417 (2015c)

[Google Scholar \(http://scholar.google.com\)](http://scholar.google.com)

/scholar_lookup?title=Theoretical%20investigation%20of%20slab%20waveguide%20sensor%20using%20anisotropic%20metamaterials&author=SA.%20Taya&journal=Opt.%20Appl.&volume=45&pages=405-417&publication_year=2015)

Taya, S.A., Alamassi, D.M.: Reflection and transmission from left-handed material structures using Lorentz and Drude medium models. *Opto-Electron. Rev.* **23**, 214–221 (2015)

[CrossRef \(https://doi.org/10.1515/oere-2015-0031\)](https://doi.org/10.1515/oere-2015-0031)

[Google Scholar \(http://scholar.google.com\)](http://scholar.google.com)

/scholar_lookup?title=Reflection%20and%20transmission%20from%20left-handed%20material%20structures%20using%20Lorentz%20and%20Drude%20medium%20models&author=SA.%20Taya&author=DM.%20Alamassi&journal=Opto-Electron.%20Rev.&volume=23&pages=214-221&

[publication_year=2015\)](#)

Taya, S.A., El-Agez, T.M.: Comparing optical sensing using slab waveguides and total internal reflection ellipsometry. *Turk. J. Phys.* **35**, 31–36 (2011a)

[Google Scholar](#) (<http://scholar.google.com>

[/scholar_lookup?title=Comparing%20optical%20sensing%20using%20slab%20waveguides%20and%20total%20internal%20reflection%20ellipsometry&author=SA.%20Taya&author=TM.%20El-Agez&journal=Turk.%20J.%20Phys.&volume=35&pages=31-36&publication_year=2011\)](#)

Taya, S.A., El-Agez, T.M.: Reverse symmetry optical waveguide sensor using plasma substrate. *J. Opt.* **13**, 075701-1–075701-6 (2011b)

[ADS](#) ([http://adsabs.harvard.edu/cgi-bin/nph-](http://adsabs.harvard.edu/cgi-bin/nph-data_query?link_type=ABSTRACT&bibcode=2011JOpt...13g5701T)

[data_query?link_type=ABSTRACT&bibcode=2011JOpt...13g5701T\)](#)

[CrossRef](#) (<https://doi.org/10.1088/2040-8978/13/7/075701>)

[Google Scholar](#) (<http://scholar.google.com>

[/scholar_lookup?title=Reverse%20symmetry%20optical%20waveguide%20sensor%20using%20plasma%20substrate&author=SA.%20Taya&author=TM.%20El-Agez&journal=J.%20Opt.&volume=13&pages=075701-1-075701-6&publication_year=2011\)](#)

Taya, S.A., El-Agez, T.M.: Slab waveguide sensor based on amplified phase change due to multiple total internal reflections. *Turk. J. Phys.* **36**, 67–76 (2012a)

[Google Scholar](#) (<http://scholar.google.com>

[/scholar_lookup?title=Slab%20waveguide%20sensor%20based%20on%20amplified%20phase%20change%20due%20to%20multiple%20total%20internal%20reflections&author=SA.%20Taya&author=TM.%20El-Agez&journal=Turk.%20J.%20Phys.&volume=36&pages=67-76&publication_year=2012\)](#)

Taya, S.A., El-Agez, T.M.: Optical sensors based on Fabry-Perot resonator and fringes of equal thickness structure. *Optik Int. J. Light Electron. Opt.* **123**, 417–421 (2012b)

[CrossRef](#) (<https://doi.org/10.1016/j.ijleo.2011.04.020>)

[Google Scholar](#) (<http://scholar.google.com>

[/scholar_lookup?title=Optical%20sensors%20based%20on%20Fabry-Perot%20resonator%20and%20fringes%20of%20equal%20thickness%20structure&author=SA.%20Taya&author=TM.%20El-Agez&journal=Optik%20Int.%20J.%20Light%20Electron.%20Opt.&volume=123&pages=417-421&publication_year=2012\)](#)

Taya, S.A., Elwasife, K.Y.: Field profile of asymmetric slab waveguide structure with LHM layers. *J. Nano Electron. Phys.* **6**, 02007-1–02007-5 (2014)

[Google Scholar](#) (<http://scholar.google.com>

[/scholar_lookup?title=Field%20profile%20of%20asymmetric%20slab%20waveguide%20structure%20with%20LHM%20layers&author=SA.%20Taya&author=KY.%20Elwasife&journal=J.%20Nano%20Electron.%20Phys.&volume=6&pages=02007-1-02007-5&publication_year=2014\)](#)

Taya, S.A., Kullab, H.M.: Optimization of transverse electric peak type metal-clad waveguide sensor using double negative materials. *Appl. Phys. A* **116**, 1841–1846 (2014)

[ADS](#) ([http://adsabs.harvard.edu/cgi-bin/nph-](http://adsabs.harvard.edu/cgi-bin/nph-data_query?link_type=ABSTRACT&bibcode=2014ApPhA.116.1841T)

[data_query?link_type=ABSTRACT&bibcode=2014ApPhA.116.1841T\)](#)

[CrossRef](#) (<https://doi.org/10.1007/s00339-014-8338-y>)

[Google Scholar](#) (<http://scholar.google.com>

[/scholar_lookup?title=Optimization%20of%20transverse%20electric%20peak%2](#)

[otype%20metal-](#)

[clad%20waveguide%20sensor%20using%20double%20negative%20materials&author=SA.%20Taya&author=HM.%20Kullab&journal=Appl.%20Phys.%20A&volume=116&pages=1841-1846&publication_year=2014\)](#)

Taya, S.A., Qadoura, I.M.: Guided modes in slab waveguides with negative index cladding and substrate. *Optik* **124**, 1431–1436 (2013)

[ADS](#) ([http://adsabs.harvard.edu/cgi-bin/nph-](http://adsabs.harvard.edu/cgi-bin/nph-data_query?link_type=ABSTRACT&bibcode=2013Optik.124.1431T)

[data_query?link_type=ABSTRACT&bibcode=2013Optik.124.1431T\)](#)

[CrossRef](#) (<https://doi.org/10.1016/j.ijleo.2012.03.057>)

[Google Scholar](#) (<http://scholar.google.com>

[/scholar_lookup?title=Guided%20modes%20in%20slab%20waveguides%20with%20negative%20index%20cladding%20and%20substrate&author=SA.%20Taya&author=IM.%20Qadoura&journal=Optik&volume=124&pages=1431-1436&publication_year=2013\)](#)

Taya, S.A., El-Farram, E.J., El-Agez, T.M.: Goos Hänchen shift as a probe in evanescent slab waveguide sensors. *Int. J. Electron. Commun. (AEÜ)* **66**, 204–210 (2012a)

[CrossRef](#) (<https://doi.org/10.1016/j.aeue.2011.07.004>)

[Google Scholar](#) (http://scholar.google.com/scholar_lookup?title=Goos%20H%C3%A4nchen%20shift%20as%20a%20probe%20in%20evanescent%20slab%20waveguide%20sensors&author=SA.%20Taya&author=EJ.%20El-Farram&author=TM.%20El-Agez&journal=Int.%20J.%20Electron.%20Commun.%20%28AE%C3%9C%29&volume=66&pages=204-210&publication_year=2012)

Taya, S.A., El-Farram, E.J., Abadla, M.M.: Symmetric multilayer slab waveguide structure with a negative index material: TM case. *Optik* **123**, 2264–2268 (2012b)

[ADS](#) ([http://adsabs.harvard.edu/cgi-bin/nph-](http://adsabs.harvard.edu/cgi-bin/nph-data_query?link_type=ABSTRACT&bibcode=2012Optik.123.2264T)

[data_query?link_type=ABSTRACT&bibcode=2012Optik.123.2264T\)](#)

[CrossRef](#) (<https://doi.org/10.1016/j.ijleo.2011.11.016>)

[Google Scholar](#) (<http://scholar.google.com>

[/scholar_lookup?title=Symmetric%20multilayer%20slab%20waveguide%20structre%20with%20a%20negative%20index%20material%3A%20TM%20case&author=SA.%20Taya&author=EJ.%20El-Farram&author=MM.%20Abadla&journal=Optik&volume=123&pages=2264-2268&publication_year=2012\)](#)

Taya, S.A., Kullab, H.M., Qadoura, I.M.: Dispersion properties of slab waveguides with double negative material guiding layer and nonlinear substrate. *J. Opt. Soc. Am. B* **30**, 2008–2013 (2013a)

[ADS](#) ([http://adsabs.harvard.edu/cgi-bin/nph-](http://adsabs.harvard.edu/cgi-bin/nph-data_query?link_type=ABSTRACT&bibcode=2013JOSAB..30.2008T)

[data_query?link_type=ABSTRACT&bibcode=2013JOSAB..30.2008T\)](#)

[CrossRef](#) (<https://doi.org/10.1364/JOSAB.30.002008>)

[Google Scholar](#) (<http://scholar.google.com>

[/scholar_lookup?title=Dispersion%20properties%20of%20slab%20waveguides%20with%20double%20negative%20material%20guiding%20layer%20and%20nonlinear%20substrate&author=SA.%20Taya&author=HM.%20Kullab&author=IM.%20Qadoura&journal=J.%20Opt.%20Soc.%20Am.%20B&volume=30&pages=2008-2013&publication_year=2013\)](#)

Taya, S.A., Elwasife, K.Y., Kullab, H.M.: Dispersion properties of anisotropic-metamaterial slab waveguide structure. *Opt. Appl.* **43**, 857–869 (2013b)

[Google Scholar](#) (<http://scholar.google.com>

[/scholar_lookup?title=Dispersion%20properties%20of%20anisotropic-metamaterial%20slab%20waveguide%20structure&author=SA.%20Taya&author=KY.%20Elwasife&author=HM.%20Kullab&journal=Opt.%20Appl.&volume=43&pages=857-869&publication_year=2013\)](#)

- Taya, S.A., Jarada, A.A., Kullab, H.M.: Slab waveguide sensor utilizing left-handed material core and substrate layers. *Optik Int. J. Light Electron. Opt.* **127**, 7732–7739 (2016)
[CrossRef](https://doi.org/10.1016/j.ijleo.2016.05.095) (<https://doi.org/10.1016/j.ijleo.2016.05.095>)
[Google Scholar](http://scholar.google.com/scholar_lookup?title=Slab%20waveguide%20sensor%20utilizing%20left-handed%20material%20core%20and%20substrate%20layers&author=SA.%20Taya&author=AA.%20Jarada&author=HM.%20Kullab&journal=Optik%20Int.%20J.%20Light%20Electron.%20Opt.&volume=127&pages=7732-7739&publication_year=2016) (http://scholar.google.com/scholar_lookup?title=Slab%20waveguide%20sensor%20utilizing%20left-handed%20material%20core%20and%20substrate%20layers&author=SA.%20Taya&author=AA.%20Jarada&author=HM.%20Kullab&journal=Optik%20Int.%20J.%20Light%20Electron.%20Opt.&volume=127&pages=7732-7739&publication_year=2016)
- Taya, S.A., Shaheen, S.A., Alkanoo, A.A.: Photonic crystal as a refractometric sensor operated in reflection mode. *Superlattices Microstruct.* **101**, 299–305 (2017a)
[ADS](http://adsabs.harvard.edu/cgi-bin/nph-data_query?link_type=ABSTRACT&bibcode=2017SuMi..101..299T) (http://adsabs.harvard.edu/cgi-bin/nph-data_query?link_type=ABSTRACT&bibcode=2017SuMi..101..299T)
[CrossRef](https://doi.org/10.1016/j.spmi.2016.11.057) (<https://doi.org/10.1016/j.spmi.2016.11.057>)
[Google Scholar](http://scholar.google.com/scholar_lookup?title=Photonic%20crystal%20as%20a%20refractometric%20sensor%20operated%20in%20reflection%20mode&author=SA.%20Taya&author=SA.%20Shaheen&author=AA.%20Alkanoo&journal=Superlattices%20Microstruct.&volume=101&pages=299-305&publication_year=2017) (http://scholar.google.com/scholar_lookup?title=Photonic%20crystal%20as%20a%20refractometric%20sensor%20operated%20in%20reflection%20mode&author=SA.%20Taya&author=SA.%20Shaheen&author=AA.%20Alkanoo&journal=Superlattices%20Microstruct.&volume=101&pages=299-305&publication_year=2017)
- Taya, S.A., Mahdi, S.S., Alkanoo, A.A., Qadoura, I.M.: Slab waveguide with conducting interfaces as an efficient optical sensor: TE case. *J. Mod. Opt.* **64**, 836–843 (2017b)
[ADS](http://adsabs.harvard.edu/cgi-bin/nph-data_query?link_type=ABSTRACT&bibcode=2017JMOp...64..836T) (http://adsabs.harvard.edu/cgi-bin/nph-data_query?link_type=ABSTRACT&bibcode=2017JMOp...64..836T)
[CrossRef](https://doi.org/10.1080/09500340.2016.1262072) (<https://doi.org/10.1080/09500340.2016.1262072>)
[Google Scholar](http://scholar.google.com/scholar_lookup?title=Slab%20waveguide%20with%20conducting%20interfaces%20as%20an%20efficient%20optical%20sensor%3A%20TE%20case&author=SA.%20Taya&author=SS.%20Mahdi&author=AA.%20Alkanoo&author=IM.%20Qadoura&journal=J.%20Mod.%20Opt.&volume=64&pages=836-843&publication_year=2017) (http://scholar.google.com/scholar_lookup?title=Slab%20waveguide%20with%20conducting%20interfaces%20as%20an%20efficient%20optical%20sensor%3A%20TE%20case&author=SA.%20Taya&author=SS.%20Mahdi&author=AA.%20Alkanoo&author=IM.%20Qadoura&journal=J.%20Mod.%20Opt.&volume=64&pages=836-843&publication_year=2017)
- Tiefenthaler, K., Lukosz, W.: Sensitivity of grating couplers as integrated-optical chemical sensors. *J. Opt. Soc. Am. B* **6**, 209–220 (1989)
[ADS](http://adsabs.harvard.edu/cgi-bin/nph-data_query?link_type=ABSTRACT&bibcode=1989OSAJB...6..209T) (http://adsabs.harvard.edu/cgi-bin/nph-data_query?link_type=ABSTRACT&bibcode=1989OSAJB...6..209T)
[CrossRef](https://doi.org/10.1364/JOSAB.6.000209) (<https://doi.org/10.1364/JOSAB.6.000209>)
[Google Scholar](http://scholar.google.com/scholar_lookup?title=Sensitivity%20of%20grating%20couplers%20as%20integrated-optical%20chemical%20sensors&author=K.%20Tiefenthaler&author=W.%20Lukosz&journal=J.%20Opt.%20Soc.%20Am.%20B&volume=6&pages=209-220&publication_year=1989) (http://scholar.google.com/scholar_lookup?title=Sensitivity%20of%20grating%20couplers%20as%20integrated-optical%20chemical%20sensors&author=K.%20Tiefenthaler&author=W.%20Lukosz&journal=J.%20Opt.%20Soc.%20Am.%20B&volume=6&pages=209-220&publication_year=1989)
- Udd, E.: An overview of fiber optic sensors. *Rev. Sci. Instrum.* **66**, 4015–4030 (1995)
[ADS](http://adsabs.harvard.edu/cgi-bin/nph-data_query?link_type=ABSTRACT&bibcode=1995RSci...66.4015U) (http://adsabs.harvard.edu/cgi-bin/nph-data_query?link_type=ABSTRACT&bibcode=1995RSci...66.4015U)
[CrossRef](https://doi.org/10.1063/1.1145411) (<https://doi.org/10.1063/1.1145411>)
[Google Scholar](http://scholar.google.com/scholar_lookup?title=An%20overview%20of%20fiber%20optic%20sensors&author=E.%20Udd&journal=Rev.%20Sci.%20Instrum.&volume=66&) (http://scholar.google.com/scholar_lookup?title=An%20overview%20of%20fiber%20optic%20sensors&author=E.%20Udd&journal=Rev.%20Sci.%20Instrum.&volume=66&)

[pages=4015-4030&publication_year=1995\)](#)

Veselago, V.G.: The electrodynamics of substances with simultaneously negative values of ϵ and μ . *Sov. Phys. Usp.* **10**, 509–514 (1968)

[ADS](#) ([http://adsabs.harvard.edu/cgi-bin/nph-](http://adsabs.harvard.edu/cgi-bin/nph-data_query?link_type=ABSTRACT&bibcode=1968SvPhU..10..509V)

[data_query?link_type=ABSTRACT&bibcode=1968SvPhU..10..509V](#))

[CrossRef](#) (<https://doi.org/10.1070/PU1968v01on04ABEH003699>)

[Google Scholar](#) (<http://scholar.google.com>

[/scholar_lookup?title=The%2oelectrodynamics%20of%20substances%20with%20simultaneously%20negative%20values%20of%20%CE%B5%20and%20%C2%B5&author=VG.%20Veselago&journal=Sov.%20Phys.%20Usp.&volume=10&pages=509-514&publication_year=1968](#))

Wahab, M., Saputera, Y., Wahyu, Y.: Design and realization of archimedes spiral antenna for Radar detector at 2–18 GHz frequencies. In: 19th Asia-Pacific Conference on Communications (APCC), Denpasar, Indonesia Aug. 29–31, pp. 304–309 (2013). <https://doi.org/10.1109/apcc.2013.6765961> (<https://doi.org/10.1109/apcc.2013.6765961>)

Wu, C.J., Chung, Y.H., Yang, T.J., Syu, B.J.: Band gap extension in a one-dimensional ternary metal-dielectric photonic crystal. *Prog. Electromagn. Res.* **102**, 81–93 (2010)

[CrossRef](#) (<https://doi.org/10.2528/PIER10012004>)

[Google Scholar](#) (<http://scholar.google.com>

[/scholar_lookup?title=Band%20gap%20extension%20in%20a%20one-dimensional%20ternary%20metal-dielectric%20photonic%20crystal&author=CJ.%20Wu&author=YH.%20Chung&author=TJ.%20Yang&author=BJ.%20Syu&journal=Prog.%20Electromagn.%20Res.&volume=102&pages=81-93&publication_year=2010](#))

Zare, Z., Gharaati, A.: Investigation of band gap width in ternary 1D photonic crystal with left-handed layer. *Acta Phys. Pol. A* **125**, 36–38 (2014)

[CrossRef](#) (<https://doi.org/10.12693/APhysPolA.125.36>)

[Google Scholar](#) (<http://scholar.google.com>

[/scholar_lookup?title=Investigation%20of%20band%20gap%20width%20in%20ternary%201D%20photonic%20crystal%20with%20left-handed%20layer&author=Z.%20Zare&author=A.%20Gharaati&journal=Acta%20Phys.%20Pol.%20A&volume=125&pages=36-38&publication_year=2014](#))

Copyright information

© Springer Science+Business Media, LLC,
part of Springer Nature 2018

About this article

Cite this article as:

Taya, S.A., Alkanoo, A.A., Ramanujam, N.R. et al. Opt Quant Electron (2018) 50: 222. <https://doi.org/10.1007/s11082-018-1487-z>

Received

07 November 2017

Accepted

29 April 2018

First Online

11 May 2018

DOI

<https://doi.org/10.1007/s11082-018-1487-z>

Publisher Name

Springer US

Print ISSN

0306-8919

Online ISSN

1572-817X

[About this journal](#)

[Reprints and Permissions](#)

SPRINGER NATURE

© 2019 Springer Nature Switzerland AG. Part of [Springer Nature](#).

Not logged in · Not affiliated · 49.39.199.82

Institutional Sign In

Browse

My Settings

Get Help

Subscribe

Advertisement

Advertisement

Conferences > 2017 International Conference...

Survey on similar object detection in H.264 compressed video

Publisher: IEEE

3 Author(s)

K. Srinivasan ; P. Balamurugan ; V. R. Azhaguramyaa [View All Authors](#)

128

[Full Text Views](#)

Abstract

Document Sections

I Introduction

II Literature Survey

III Features of Self-Similarity

IV Conclusion

Authors

References

Keywords

Metrics

More Like This

More Like This

Performance Evaluation of Object Detection Algorithm Using Ant Colony Optimization Based Image Segmentation
2017 International Conference on Computing, Communication, Control and Automation (ICCUBEA)
Published: 2017

Moving object tracking using PTZ camera in video surveillance system
2017 International Conference on Energy, Communication, Data Analytics and Soft Computing (ICECDS)
Published: 2017

[View More](#)

Top Organizations with Patents on Technologies Mentioned in This Article



Advertisement

[Journals](#) [Magazines](#) [Proceedings](#) [Books](#) [SIGs](#) [Conferences](#) [People](#)





Proceedings ▼

[Home](#) > [ICPS Proceedings](#) > [ICCCNT '16](#) > [Power model analysis using variable rate clock network in CMOS processor](#)

RESEARCH-ARTICLE

Power model analysis using variable rate clock network in CMOS processor



Authors:  [T. Joby Titus](#),  [V. Vijayakumari](#),
 [B. Saranya](#),  [V.S. Sanjana Devi](#)

[Authors Info & Affiliations](#)

Publication: ICCCNT '16: Proceedings of the 7th International Conference on Computing Communication and Networking Technologies • July 2016 • Article No.: 33 • Pages 1–5 • <https://doi.org/10.1145/2967878.2967915>



About Cookies On This Site

We use cookies to ensure that we give you the best experience on our website.

[Learn more](#)

Got it!



Feedback

Journals Magazines Proceedings Books SIGs Conferences People

Proceedings ▼


References

Index Terms

Comments

problem. A variable rate clock network is provided to reduce unwanted switching as well as to limit active clock routing network. We propose two power models to estimate processor performance under variable rate clock signal. Overall this optimization method provides improved in power and performance in current CMOS processor.

References

1. Ying Teng and BarisTaskin 2015, ROA-Brick Topology for Low-Skew Rotary Resonant Clock Network Design, IEEE Transactions on very large scale Integration (VLSI) Systems, 23, 11, (NOVEMBER 2015), 2519--2530 
2. Pierre-Emmanuel Gaillardon, Xifan Tang, Gain Kim, and Giovanni De Micheli, 2015, A Novel FPGA



About Cookies On This Site

We use cookies to ensure that we give you the best experience on our website.

[Learn more](#)

Got it!



Feedback

Journals Magazines Proceedings Books SIGs Conferences People

Proceedings ▼

Index Terms (auto-classified)

**Power model analysis using variable rate clock
network in CMOS processor**



Hardware



Hardware validation



Very large scale integration design

Comments



About Cookies On This Site

We use cookies to ensure that we give you the best experience on our website.

[Learn more](#)

Got it!



Feedback

Journals Magazines Proceedings Books SIGs Conferences People

Proceedings ▼

 Tweet

 Share

Sort by Newest ▼

Nothing in this discussion yet.

[View Table Of Contents](#)

Categories

Journals

Magazines

Books

Proceedings

SIGs

Conferences

Collections

People

About

About ACM Digital Library

Subscription Information

Author Guidelines

Using ACM Digital Library

All Holdings within the ACM

Digital Library

ACM Computing Classification

System

Join

Join ACM

Join SIGs

Subscribe to

Publications

Institutions and

Libraries

Connect

 Contact

 Facebook

 Twitter

 LinkedIn



About Cookies On This Site

We use cookies to ensure that we give you the best experience on our website.

[Learn more](#)

Got it!



Association for
Computing Machinery



Feedback

Institutional Sign In

Browse

My Settings

Get Help

Subscribe

Advertisement

Advertisement

Conferences > TENCON 2015 - 2015 IEEE Regio...

An online task placement algorithm using Hilbert curve for a partially reconfigurable field programmable gate array

Publisher: IEEE

2 Author(s)

Senoj Joseph ; K. Baskaran

View All Authors

66

Full
Text Views

Abstract

Document Sections

- I. Introduction
- II. System Model
- III. Related Works
- IV. Proposed Technique
- V. Experimental Setup

Authors

Figures

References

Keywords

Metrics

More Like This

Abstract: With the arrival of partial reconfiguration technology, modern FPGAs support tasks that can be loaded in (removed from) the FPGA individually without interrupting other t... **View more**

Metadata

Abstract:

With the arrival of partial reconfiguration technology, modern FPGAs support tasks that can be loaded in (removed from) the FPGA individually without interrupting other tasks already running on the same FPGA. Many online task placement algorithms designed for such partially reconfigurable systems have been proposed to provide efficient and fast task placement. A new approach for online placement of modules on reconfigurable devices, by managing the free space using a run-length based representation. This representation allows the algorithm to insert or delete tasks quickly and also to calculate the fragmentation easily. In the proposed FPGA model the CLBs are numbered according to Hilbert space filling curve model. The search algorithm will quickly identify a placement for the incoming task based on first fit mode or a fragmentation aware best Fit mode. Simulation experiments indicate that proposed techniques result in low ratio of task rejection and high FPGA utilization compared to existing techniques.

Published in: TENCON 2015 - 2015 IEEE Region 10 Conference

Date of Conference: 1-4 Nov. 2015

INSPEC Accession Number: 15698431

Date Added to IEEE Xplore: 07 January 2016

DOI: 10.1109/TENCON.2015.7373169

Publisher: IEEE

ISBN Information:

Conference Location: Macao, China

ISSN Information:

More Like This

A Real-Time NetFlow-based Intrusion Detection System with Improved BBNN and High-Frequency Field Programmable Gate Arrays
2012 IEEE 11th International Conference on Trust, Security and Privacy in Computing and Communications
Published: 2012

Single Event Effects Test Results for Advanced Field Programmable Gate Arrays
2006 IEEE Radiation Effects Data Workshop
Published: 2006

View More

Top Organizations with Patents on Technologies Mentioned in This Article



Advertisement

Advertisement

Contents

I. Introduction

Reconfigurable devices with partial reconfiguration capabilities allow multitasking applications on a single chip. Embedded applications like cryptography, video communication, image processing etc. can exploit this capability. Efficient placement and scheduling algorithm can improve

Materials Research Express



PAPER

Green mediated fabrication and characterization of ZnO/Ag nanocomposite for energy storage applications

RECEIVED
1 April 2019

REVISED
2 July 2019

ACCEPTED FOR PUBLICATION
17 July 2019

PUBLISHED
24 July 2019

K Rajangam¹, K Swetha Gowri¹, R Prem Kumar¹, L M Surriya¹, S Vishnu Raj¹, B Balraj¹  and S Thangavel²

¹ Department of Electrical and Electronics Engineering, Sri Krishna College of Technology, Coimbatore-641042, India

² Department of Electrical and Electronics Engineering, National Institute of Technology Puducherry, Karaikal-609605, India

E-mail: balrajphd@hotmail.com

Keywords: zin oxide, Nanocomposites, electrochemical studies, green mediated fabrication

Abstract

The present work is intended to investigate the charge carrying properties of nanomaterials for super capacitor applications by electrochemical studies. The nanomaterials were fabricated by green route process by the rhizome of *Corallo carpus epigaeus* for the first time. The silver nanomaterials were composited over the zinc oxide nanomaterial to improve the efficiency of the energy storage system. The Fourier Transform Infrared spectrum confirm the functional molecules present in the nanomaterial. The Field Emission Scanning Electron Microscopic images evidenced the oval shape of zinc oxide and hexagonal shape of silver nanomaterials. The purity of the nanomaterials was investigated using energy dispersive spectrum. The structural property of the material was studied by x-ray Diffraction. The energy storage capacity was investigated by electrochemical studies. Higher efficiency was observed when the impurity is added with the base material. The specific capacitance was calculated as 160.8 F g^{-1} for ZnO nanomaterials and 189.52 F g^{-1} for ZnO/Ag nanocomposites at the current density of 0.5 A g^{-1} . The electrochemical impedance studies were also carried out for the fabricated nanomaterials. The ZnO nanomaterials possess 603Ω of electron transfer resistance. While adding Ag^+ ions over the ZnO nanomaterials, the conductivity ($\text{Ret} = 489 \Omega$) was remarkably increased.

1. Introduction

The tremendous increase in the growth of the global energy consumption has led to the growth of renewable energy sources for energy generation such as wind and solar power. Since the energy produced by these methods is regionally limited and also intermittent, more research activities are carried out to store the enormous amount of energy. The development of advanced energy storage devices such as super capacitor aids to arrive at the solution for such problems [1–5]. They serve as efficient storage system for electrical energy at all scales range. The super capacitors are the energy storage devices which has very large capacity of storage of energy per unit mass compared to normal electrolytic capacitor [6, 7]. It is known fact that the working and efficiency of energy storage device depends on various factors, which is mainly enhanced by the structure and properties of the material from which it is formed. These supercapacitors are widely used as an alternative to capacitors with high power and energy density. When the super capacitors are coated with nanomaterials they integrate the electrode with higher surface area and much thinner dielectrics that decreases the distance between the electrodes [8]. This helps in increasing both the capacitance and the energy which can be stored. The supercapacitors can be effectively made from materials such as conducting polymers, transition metal oxides and carbon materials with a porous nanomaterial electrode structures. Due to the faradic redox reaction the ion transfer between the electrode and electrolyte leads to enhance the capacitance of the metal oxides. High cost materials like ruthenium oxide provide higher pseudocapacitance [9]. For the large scale production, the material should be cost effective and provide almost similar properties of high cost materials. Usually, the reversible faradic reaction that is taking place at the surface of the electrode yields the pseudocapacitors. These pseudo capacitors exhibit similar behavior like transition metal oxide supercapacitors [10]. Various materials have been investigated for



Green Synthesis and Electrical Properties of p-CuO/n-ZnO Heterojunction Diodes

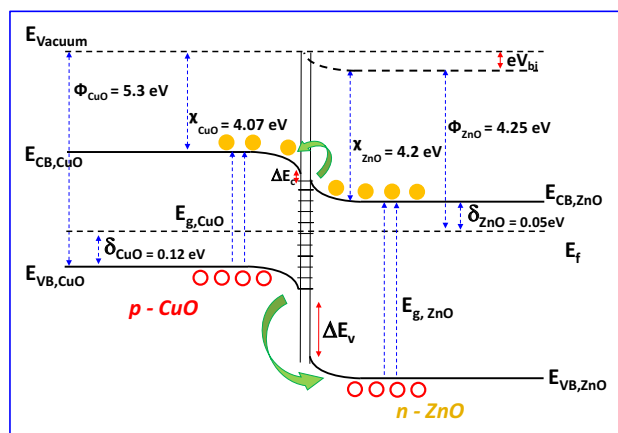
Sridevi Annathurai¹ · Siva Chidambaram² · Balraj Baskaran³ · G. K. D. Prasanna Venkatesan⁴

Received: 10 September 2018 / Accepted: 22 November 2018
 © Springer Science+Business Media, LLC, part of Springer Nature 2018

Abstract

Green production of nanomaterials and their materials properties studies are majorly important for the futuristic development of nanodevices. We had green synthesized the ZnO and CuO nanoparticles using the extract of “*Eucalyptus globulus*” leaves. The obtained ZnO and CuO nanoparticles were studied for their structural, morphological and optical properties. The green synthesized CuO and ZnO nanoparticles have showed the crystalline size of about 12.29 and 10.16 nm. The transmission electron microscopic images of green synthesized ZnO and CuO nanoparticles revealed the morphological information and their respective average sizes of 46 and 32 nm. Optical absorbance spectrum revealed the existence of morphology based quantum confinement in the green ZnO and CuO nanoparticles. Further we have fabricated the p-CuO/n-ZnO heterojunction device using the green synthesized nanoparticles and also evaluated the electrical properties of the p–n junction diode. Under the light illumination the photodiode characteristic were studied for the obtained p–n junction diode. Finally, the energy band diagram of the photodiode responsible for the electronic transport had also discussed.

Graphical Abstract



Keywords Green synthesis · p–n Heterojunction · Electrical properties · Photodiode

✉ Siva Chidambaram
 siva.may3@gmail.com

✉ G. K. D. Prasanna Venkatesan
 prasphd@gmail.com

¹ Department of Electronics and Communication Engineering,
 M. Kumarasamy College of Engineering, Karur 639 113,
 India

² Department of Physics and Nanotechnology, SRM Institute
 of Science and Technology, Chennai 603 203, India

³ Department of Electrical and Electronics Engineering, Sri
 Krishna College of Technology, Coimbatore 641 042, India

⁴ Karpagam Academy of Higher Education,
 Coimbatore 641 021, India

1 Introduction

Copper is an excessively applied in several applications in electronic circuits and heat transfer appliances. The oxides of Cu, such as cuprous oxide (Cu_2O), cupric oxide (CuO) and copper(III) oxide (Cu_4O_3) are most important semiconductors and showed their potential use in electronic and photonic devices. Especially CuO is a p-type semiconductor possessing a narrow—direct band gap ($E_g = \sim 1.4$ eV) and versatile material such as catalyst, energy storage material, superconductor, field emission material and etc. [1, 2]. With high absorption coefficient, CuO is renowned as a suitable solar absorber material over Cu_2O nanostructures. Electrical properties such as majority charge carrier mobility and minority charge carrier diffusion are also adequate in the case CuO compared to the Cu_2O [1].

Likewise, ZnO nanostructures are quite fascinating materials in recent days in biological [3], photocatalytic [4] and electronic applications [5–8]. ZnO is an n-type wide—direct band gap ($E_g = 3.37$ eV) semiconductor, possessing large excitonic binding energy (~ 60 meV compared with ~ 25 meV for GaN). Intrinsic carrier concentration ($< \sim 10^6 \text{ cm}^{-3}$), better electron hall mobility ($200 \text{ cm}^2/\text{V/s}$ for n-type) and hole hall mobility ($5\text{--}50 \text{ cm}^2/\text{V/s}$ for p-type) [5–7]. These exciting properties of the ZnO nanostructures make the ZnO as an unavoidable material in several electronic devices and circuits. Synergistically the combination of n-type ZnO and p-type CuO as p–n heterojunction had showed excellent properties such as hydrogen production electrode [8], self-cleaning device [9], non-enzymatic sensor [10], solar cell [11], gas sensing [12], hydrophobic and anticorrosion devices [13]. The wide range of application features of the p- $\text{CuO}/\text{n-ZnO}$ heterojunction diodes indicate the requirement of more investigations and green development strategies of the diodes.

The CuO and ZnO nanomaterials were developed through several synthetic techniques including sol–gel process, co-precipitation, hydro/solvo thermal techniques, thermal evaporation techniques [1–6]. On other hand, these nanomaterials had also been produced through green synthetic methods, either with phytochemicals obtained from the plant extract, or biochemical reagents obtained from the microorganism. Contrast to abovementioned other synthesis of nanostructure phytochemicals based synthetic strategy is an independent of sophisticated instruments or toxic chemical reagents. Also the phytochemicals are acting as agglomeration preventing agent as an added advantage [14–17]. Considering the aforementioned key factors, we obtained the ZnO and CuO nanoparticles through the phytochemical based green synthesis by using the leaf

extract obtained from *Eucalyptus globulus*. The obtained nanoparticles were characterized for their morphological, structural and optical properties. Also we had developed a p–n heterojunction device with the obtained nanomaterials, for which we have studied the diode properties. In best of our study, we first report the p–n heterojunction diode structure obtained using the green synthesized p- CuO and n- ZnO .

2 Experimental Section

2.1 Preparation of Plant Extract

Fresh *Eucalyptus* leaves were collected from local farm in Karur, Tamilnadu, India. The collected leaves were washed thoroughly with plenty of water and are dried at room temperature. The leaves of about 20 g was taken in 200 ml of deionized water and the mixture was heat treated with reflux condition at 100°C for 30 min. Then the extract solution was collected by filtration process. The collected solution was further utilized to the nanoparticles synthesis reactions without any further purifications.

2.2 Green Synthesis of ZnO Nanoparticles

In a typical green synthesis of ZnO nanoparticles, we have taken zinc acetate of 0.11 g in 100 ml water. The plant extract of 20 ml was added to the zinc acetate solution. The mixture was homogeneously dissolved with ultrasonication for 2 min. The obtained sol was transformed into a Teflon coated stainless steel based autoclave container and then the hydrothermal reaction was executed for 12 h under 150°C . We found the formation of sediments in the autoclave container after the reaction course. The obtained sediments were collected using centrifugation after cooled down to room temperature and then washed with deionized water for several times. The obtained ZnO nanopowder was dried at 60°C and subsequently calcined at 400°C for 5 h. Then the powder was further utilized for characterization without any further process.

2.3 Green Synthesis of CuO Nanoparticles

The green synthesis of CuO nanoparticles was conducted as identical to the above said green synthesis of ZnO nanoparticles. The cupric acetate of 0.091 g was taken in 100 ml as initial precursor for the CuO nanoparticles. Further with 20 ml of plant extract the same synthesis strategy was executed, as utilized for synthesis of ZnO nanoparticles.

2.4 Fabrication of p-CuO/n-ZnO Heterojunction Diodes

The green synthesized nanoparticles of ZnO and CuO nanoparticles were dissolved separately well in 2-mercaptoethanol (0.1 g in 100 ml) using ultra sonication until a homogeneous solution is obtained. The obtained ZnO solution was added in drops on the indium tin oxide coated glass substrate placed in the spin coater unit rotating at 3000 rpm for 30 s, and the ZnO nanoparticles coated substrate was heat treated at 80 °C for 10 min. This process had been repeated for 10 times to achieve a final film. In the same manner CuO suspension also deposited on the ZnO/ITO substrate. After all the obtained device was heat treated at 500 °C for 30 min in Ar gas atmosphere with the gas flow rate of ~30 sccm in to the furnace. And then the silver conductive paste (sheet resistance < 0.025 $\Omega/\text{in.}^2$ at 0.001 m in thick) was utilized to have the ohmic electrical contact in the required places of the device. Further the obtained electrical contacts were dried at 200 °C for 30 min. The schematic of the obtained device illustrated in the following sections.

2.5 Characterization

Structural and elemental studies were studied using the pattern obtained from X-ray diffraction (XRD) using X'pert-pro diffractometer equipped with Cu K α radiation of 1.54060 Å. Transmission electron microscopic images were recorded for the specimens to study their morphological features using the Techno T20 model instrument. Optical absorbance studies of the specimens were recorded in ultraviolet and visible region using the UV-vis spectrophotometer (JASCO V-650 model). The I-V graph of the obtained devices were studied using the instrument Keithley-6517B semiconductor parameter analyzer.

3 Results and Discussion

3.1 Structural Analysis

Figure 1 shows the XRD pattern of the green synthesized ZnO and CuO nanoparticles. The lattice parameters and the d-spacing values of the obtained diffraction peaks of the ZnO pattern were well matched with hexagonal wurtzite structure of ZnO as per the Joint Committee on Powder Diffraction Standards (JCPDS) card number of 36-1451. The lattice constants $a = 0.347$ nm, $c = 0.5156$ nm and $c/a = 0.1485$ nm are calculated from the obtained XRD pattern. Further the average crystalline size of the ZnO nanoparticles is calculated using the Scherrer equation as crystallite size, $D = 0.89\lambda/(\beta \cos\theta)$, where λ is the wavelength of the X-ray used for the diffraction (1.5406 Å), β is full width at half maximum of

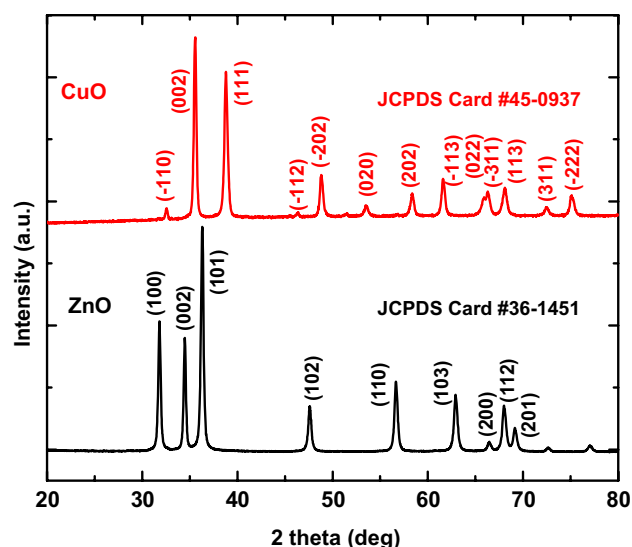


Fig. 1 XRD patterns of green synthesized ZnO and CuO nanoparticles

the peak and θ is the peak position. Thus calculated average crystalline size of the ZnO nanoparticles are 10.16 nm. Figure 1 also shows the diffraction pattern obtained for the CuO nanoparticles indicating the monoclinic structure in accordance to the JCPDS card number 48-1548, having the lattice parameter values as $a = 0.46837$ nm $b = 0.34226$ nm, $c = 0.51288$ nm and $\beta = 99.540^\circ$. The average crystalline size of the CuO nanoparticles was calculated to be 12.29 nm by using the Scherrer equation. Moreover in the obtained patterns, the nonexistence of any other impurity peaks such as zinc hydroxyls, zinc metal, other oxides of copper such as Cu_2O and Cu metal in the case of CuO, indicating the phase purity of the obtained nanomaterials.

3.2 Morphological Analysis

The green synthesized CuO and ZnO specimens were evaluated with the transmission electron microscope (TEM) for their morphological information. The obtained images of ZnO specimens indicated the nanoparticle morphology showing the agglomeration free particles throughout the samples (Fig. 2). From the obtained images, the ZnO nanoparticles of size ranging from 30 to 60 nm could be identified. The particle size distribution graph of the measured ZnO nanoparticles indicating the major number of ZnO nanoparticles are of 41–50 nm. Like the same, green synthesized CuO specimens are also imaged with TEM for their morphological information. The obtained micrographs indicating the particulate-like morphology of CuO, possessing the size from 20 to 50 nm. The size distribution curve of the CuO nanoparticles is indicating the average particle size of 31–35 nm.

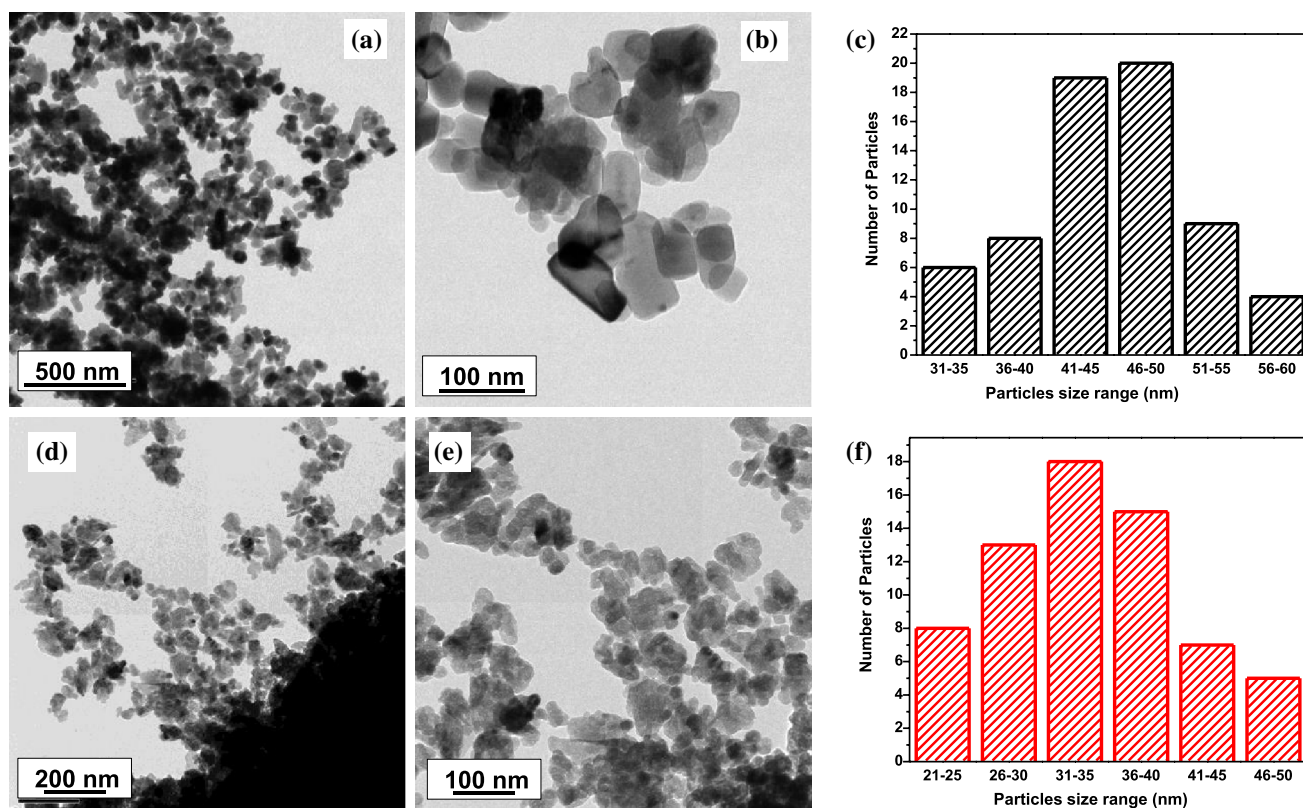


Fig. 2 TEM images of green synthesized ZnO (a, b) and CuO (d, e) nanoparticles and particle size distribution graph of ZnO (c) and CuO (f) nanoparticles

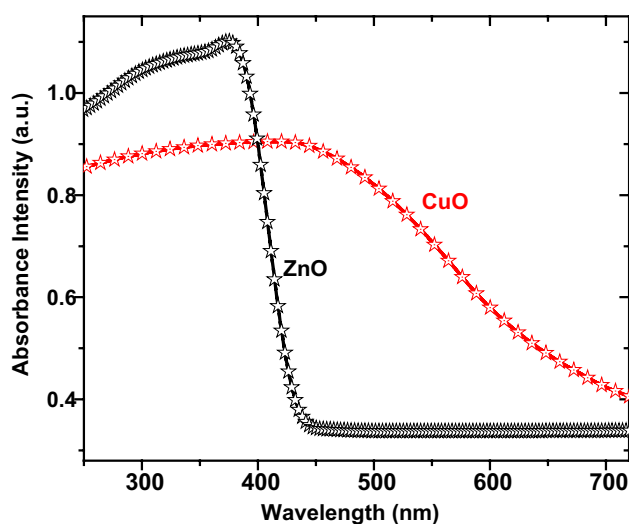


Fig. 3 UV-visible absorption spectrum of green synthesized ZnO and CuO nanoparticles

3.3 UV-Vis Absorption Properties

Figure 3 shows the UV-vis absorption spectra of green synthesized ZnO and CuO nanoparticles. The absorption

spectra of ZnO nanoparticles showed a peak at the wavelength of 368 nm. This peak of the ZnO can be for the characteristic band edge absorption at the ZnO semiconducting systems. The band gap of the ZnO nanoparticles was calculated from the Tauc's plot and is found to be 3.39 eV. The absorption spectra graph of CuO nanoparticles showed an absorption edge at 430 nm. Like the same, the band gap value of the CuO nanoparticles are found to be 1.52 eV.

Interestingly the band gap values obtained for the green synthesized ZnO and CuO nanoparticles have showed moderately enhanced values from the bulk materials ($E_g(\text{bulk CuO}) = 1.4 \text{ eV}$ and $E_g(\text{bulk ZnO}) = 3.32 \text{ eV}$) [1, 6]. The change in the band gap value from the bulk structures generally relies on numerous factors including morphology of the particle (size induced quantum confinement), charge carrier concentration, grain size, lattice strain, orbital hybridization by doping the impurity atoms, etc. In this present study, morphology could be the reason behind the marginally deviated band gap values from the bulk structures in both the nanostructures.

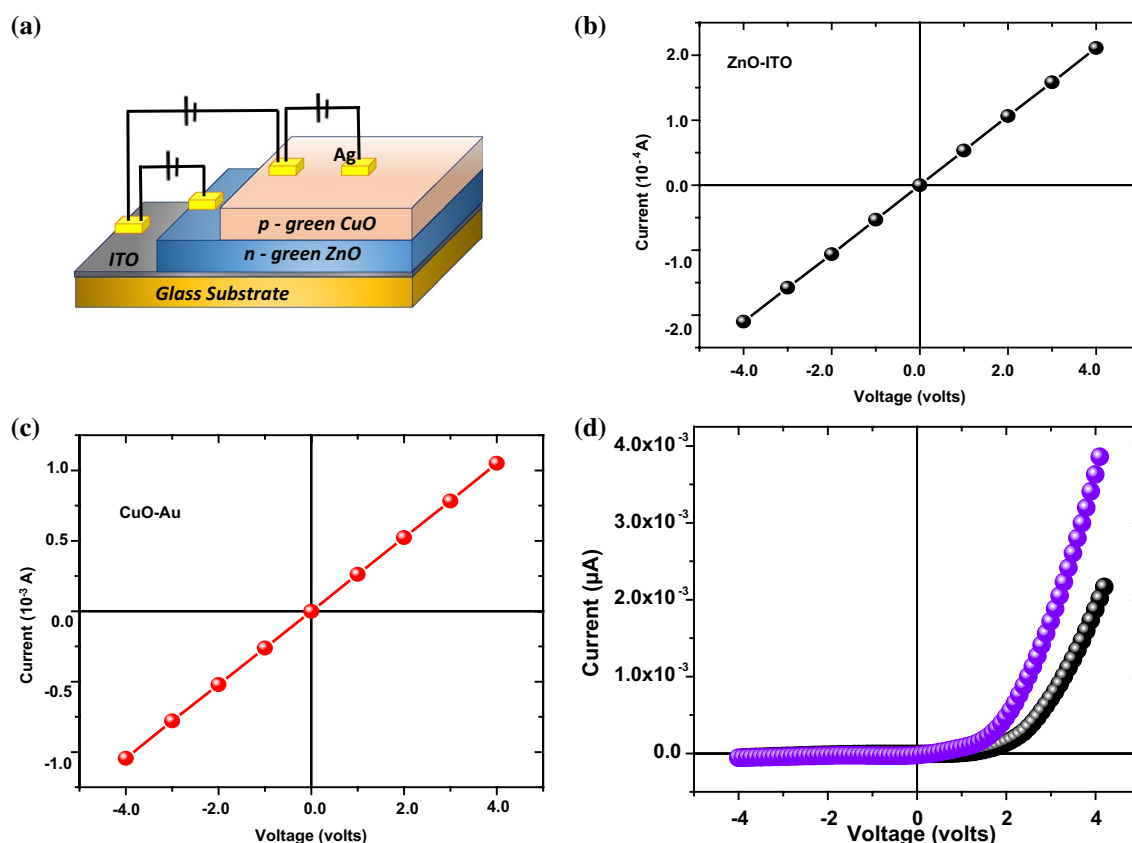


Fig. 4 Schematic representation of the fabricated p-CuO/n-ZnO heterojunction diode structure (a), I–V curves of the obtained ohmic contacts with ZnO (b) and CuO (c) and characteristic rectification curve (I–V) of the p-CuO/n-ZnO heterojunction diode (d)

3.4 Electrical Characteristics of the p-CuO/n-ZnO Diodes

The scheme of the fabricated p-CuO/n-ZnO junction diode using the green synthesized p-CuO and n-ZnO nanomaterials are as shown in Fig. 4a. Figure 4b, c show the I–V characteristics obtained for the interfaces of Ag/CuO and ZnO/ITO, which are linear in nature, indicating the ohmic behavior of the contacts. The obtained I–V graphs (shown in Fig. 4d) for p-CuO/n-ZnO heterojunction have showed the non-linear characteristics, representing the non-ohmic behavior and characteristic rectifying I–V behavior of p–n junction diode. The obtained graph proved the rectifying behavior of the obtained diode structure. The leakage current measured from the diode characteristic curve for 4 V is 5.4×10^{-5} A for reverse bias and 2.2×10^{-3} A for forward bias, resulting the forward-to-reverse bias current ratio of about 40. The resultant current for the applied voltage in the p–n heterojunction device follows the relationship as per the equation, $I = I_0(e^{[q(V-IR_b)/\eta KT]} - 1)$, where I_0 is the reverse saturation current, V is the applied voltage and R_b is the series resistance, which is included to account the bulk resistance of the sample. The resistance of the diode at

the high voltage range of the forward bias (i.e., 2.0–4.0 V) showed the series resistance varies from 14 to 2 mΩ. The built-in potential of the obtained heterojunction diode is about 2 V. All these values of the p-CuO/n-ZnO heterojunction diodes are highly comparable to the existing reported results [12, 13, 18, 19]. In general the ideal diode should possess the ideality factor a 2, however in our case the structural/crystalline mismatch, defect states in the interface would have influenced to have this value. For the illumination of light the drastic change in the current value had been observed, especially from the potential of 1.8–4.0 V. The drastic increase in the current conversion could be reasoned to the photovoltaic effect of the ZnO and CuO semiconductors in the heterojunction system. Moreover the built in potential value had also been improved drastically for the light illumination indicating the potential advantage of the obtained device in the photovoltaic applications.

3.5 Energy Band Structure

Figure 5 show the energy band diagram of the p-CuO/n-ZnO heterojunction at thermal equilibrium condition. The electron affinity (χ_{CuO}) and band gap ($E_{g,\text{CuO}}$) of the p-CuO are

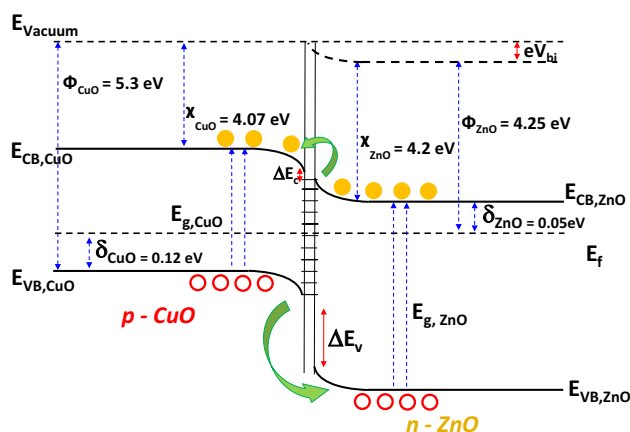


Fig. 5 Energy band diagram of the p-CuO/n-ZnO heterojunction diode under light illumination

4.07 eV, 5.3 eV and 1.35 eV [18]. The Fermi energy level to the valence band distance is 0.12 eV. On other hand, the electron affinity (χ_{ZnO}) and band gap ($E_{g,\text{ZnO}}$) of n-type ZnO as reported are 4.2 and 3.3 eV. Also the energy difference between the Fermi energy level of ZnO and the conduction band is ~ 0.05 eV [20–23].

In general, the work function of p-type semiconductor (Φ_p) and n-type semiconductor (Φ_n) of the semiconductors are calculated from the equations, $\Phi_p = \chi_p + E_{g,p} - \delta_p$ and $\Phi_n = \chi_n + \delta_n$. Thus calculated work function values of CuO ($\Phi_{p,\text{CuO}}$) and ZnO ($\Phi_{n,\text{ZnO}}$) are 5.3 and 4.25 eV, respectively. Further the total built-in-voltage V_{bi} is determined by the equation, $V_{bi} = V_{bip} + V_{bin} = \Phi_p - \Phi_n$, which is 1.05 eV [20, 22]. Upon illumination of light (UV light), the electron-hole pair generation can be realized in both the p-CuO and n-ZnO region. Since ΔE_c possess lower value than ΔE_v , the charge carrier transport through the conduction band is dominant, which generally result a large photocurrent value through this heterojunction device. For the illumination of visible and near-infra red region photons for which ZnO is unable to generate excitons, the accumulation of photogenerated holes in the CuO occurs in the $E_{VB,CuO}$. This accumulation of holes in valence band of CuO may cause only an insignificant photocurrent.

4 Conclusion

Green synthetic approach routed ZnO and CuO nanoparticles were obtained, using the extract of “*Eucalyptus globulus*” leaves. The crystalline size of the ZnO and CuO nanoparticles are of 10.16 and 12.29 nm, respectively. The obtained electron microscope images of the nanoparticles have showed the particles size of about 40 nm for ZnO

nanoparticles and 30 nm for CuO nanoparticles. Optical absorbance spectrum of the nanoparticles indicated the existence of quantum confinement effect. The I–V measurements were obtained for the obtained p-CuO/n-ZnO heterojunction diodes under both dark and light illuminations. Significant increase in the current value for the light illumination over the dark condition indicate the technological importance of the obtained device. Also we have studied the energy band diagram of the heterojunction.

References

1. T.K.S. Wong, S. Zhuk, S.M. Panah, G.K. Dalapati, *Materials* **9**, 271 (2016)
2. A. Bhaumik, A.M. Shearin, R. Patel, K. Ghosh, *Phys. Chem. Chem. Phys.* **16**, 11054 (2014)
3. Ü Özgür, Y.I. Alivov, C. Liu, A. Teke, M.A. Reshchikov, S. Doğan, V.C.S.J. Avrutin, S.-J. Cho, H. Morkoç, *J. Appl. Phys.* **98**, 11 (2005)
4. M. Jayapriya, M. Arulmozhi, B. Balraj, *Ceram. Int.* **44**, 13152 (2018)
5. C. Vivek, C. Siva, G. Mohan Kumar, *J. Mater. Sci. Mater. Electron.* **29**, 667 (2018)
6. O.C. Boon, L.Y. Ng, A.W. Mohammad, *Renew. Sustain. Energy Rev.* **81**, 536 (2018)
7. P. Mahsa, A. Habibi-Yangjeh, S.R. Pouran, *J. Ind. Eng. Chem.* **62**, 1 (2018)
8. L. Zhengxin, M. Jia, B. Abraham, J.C. Blake, D. Bodine, J.T. Newberg, L. Gundlach, *Langmuir* **34**, 961 (2017)
9. G. Zheng, X. Chen, J. Li, J.-H. Liu, X.-J. Huang, *Langmuir* **27**, 6193 (2011)
10. A. Rafiq, N. Tripathy, M.S. Ahn, K.S. Bhat, T. Mahmoudi, Y. Wang, J.Y. Yoo, D.W. Kwon, H.Y. Yang, Y.-B. Hahn, *Sci. Rep.* **7**, 5715 (2017)
11. H. Sajad, C. Cao, G. Nabi, W.S. Khan, M. Tahir, M. Tanveer, I. Aslam, *Opt. Int. J. Light Electron Opt.* **130**, 372 (2017)
12. S. Mridha, D. Basak, *Semicond. Sci. Technol.* **21**, 928 (2006)
13. B. Farshad, H. Khojasteh, M.S. Niasari, *Materials* **10**, 697 (2017)
14. G. Sangeetha, S. Rajeshwari, R. Venkatesh, *Mater. Res. Bull.* **46**, 2560 (2011)
15. S.S.M.S. Arif, A.R. Park, K. Zhang, J.H. Park, P.J. Yoo, *ACS Appl. Mater. Interface* **4**, 3893 (2012)
16. M.A. Hussein, M.L. Baynosa, D. Tuma, J.J. Shim, *Appl. Catal. B* **203**, 416 (2017)
17. X. Yifeng, G. Yu, Z. Shan, Z. Li, *J. Photochem. Photobiol. B* **186**, 131 (2018)
18. R.R. Prabhu, A.C. Saritha, M.R. Shijeesh, M.K. Jayaraj, *Mater. Sci. Eng. B* **220**, 82 (2017)
19. G. Amrita, B.B. Show, S. Ghosh, N. Mukherjee, G. Bhattacharya, S.K. Datta, A. Mondal, *RSC Adv.* **4**(93), 51569–51575 (2014)
20. K.M. Arif, Y. Wahab, R. Muhammad, M. Tahir, S. Sakrani, *Appl. Surf. Sci.* **435**, 718 (2018)
21. R. Krithikadevi, M. Arulmozhi, C. Siva, B. Balraj, G. Mohan Kumar, *J. Mater. Sci. Mater. Electron.* **28**, 5440 (2017)
22. C. Siva, G. Ganga, G. Mohan Kumar, P. Baraneedharan, B. Karthikeyan, M. Sivakumar, *J. Colloid Interface Sci.* **452**, 169 (2015)
23. H.T. Hsueh, S.J. Chang, W.Y. Weng, C.L. Hsu, T.J. Hsueh, F.Y. Hung, S.L. Wu, B.T. Dai, *IEEE Trans. Nanotechnol.* **11**, 127 (2012)

Fabrication and characterisation of silver nanoparticles using bract extract of *Musa paradisiaca* for its synergistic combating effect on phytopathogens, free radical scavenging activity, and catalytic efficiency

ISSN 1751-8741

Received on 22nd May 2018

Accepted on 05th September 2018

doi: 10.1049/iet-nbt.2018.5136

www.ietdl.org

Jayapriya Maruthai¹, Arulmozhi Muthukumarasamy¹ ✉, Balraj Baskaran²¹Department of Petrochemical Technology, Bharathidasan Institute of Technology Campus, Anna University, Tiruchirappalli – 620 024, India²Department of Electrical and Electronics Engineering, Sri Krishna College of Technology, Coimbatore - 641042, India

✉ E-mail: arulmozhiphd@hotmail.com

Abstract: This work explores the rapid synthesis of silver nanoparticles (AgNPs) from *Musa paradisiaca* (*M. paradisiaca*) bract extract. The bio-reduction of Ag⁺ ion was recorded using ultraviolet–visible spectroscopy by a surface plasmon resonance extinction peak with an absorbance at 420 nm. The phytoconstituents responsible for the reduction of AgNPs was probed using Fourier transform infrared spectroscopy. The X-ray diffraction pattern confirmed the formation of crystalline AgNPs that were analogous to selected area electron diffraction patterns. Morphological studies showed that the obtained AgNPs were monodispersed with an average size of 15 nm. The biologically synthesised AgNPs showed higher obstruction against tested phytopathogens. The synthesised AgNPs exhibited higher inhibitory zone against fungal pathogen *Alternaria alternata* and bacterial pathogen *Pseudomonas syringae*. Free radical scavenging potential of AgNPs was investigated using 1,1-diphenyl-2-picryl hydroxyl and 2,2-azinobis (3-ethylbenzothiazoline)-6-sulphonic acid assays which revealed that the synthesised AgNPs act as a potent radical scavenger. The catalytic efficiency of the synthesised AgNPs was investigated for azo dyes, methyl orange (MO), methylene blue (MB) and reduction of o-nitrophenol to o-aminophenol. The results portrayed that AgNPs act as an effective nanocatalyst to degrade MO to hydrazine derivatives, MB to leucomethylene blue, and o-nitro phenol to o-amino phenol

1 Introduction

Nanoparticles (NPs) contain unique characteristic features of having ultra-small size and huge bioactive surface area that make them potential candidates for microbial colonisation [1]. Metal NPs are well-known for their versatile application in the multidisciplinary field. Silver NPs (AgNPs) have garnered a lot of deliberation due to their capacious spectrum of microbicidal activity, free radical scavenging, anti-inflammatory activity and the minimum propensity of bacterial resistance. The remarkable characteristic feature of AgNPs is that at the minimum dosage, they are harmful to microbes, especially more effective against multidrug-resistant bacteria, but safe to human cells [2]. There are numerous physiochemical techniques that have been employed to synthesise AgNPs. All those techniques have several shortcomings such as the use of hazardous chemicals, and rigorous energy that makes these procedures expensive and harmful to the environment [3–5]. With increasing concerns on the biological and environmental impact of AgNPs, there is a significant need to create a non-toxic ‘biogenic’ synthesis which provides a superior platform of expected product at low cost [6, 7]. However, microbe-mediated synthesis has a major drawback because it is not feasible for pilot scale production due to the maintenance of cell culture under aseptic condition. However, the plant-mediated synthesis offers several advantages such as the phytoconstituents present in plant extract have bifunctional role, i.e. they act as both reducing and capping mediators and the AgNPs thus formed are more stable with different shapes and dimensions making the plant-mediated synthesis more efficient than other synthesis methods [8–11]. Microorganisms cause several catastrophic diseases in commercial crops and are responsible for remarkable losses to farmers. Among the phytopathogens, some of the bacteria and fungi have high devastating effect causing various blight and wilt diseases. Today, it is laborious to reduce diseases caused by the bacteria and fungi

due to the development of bactericide and fungicide-resistant. Current control measure includes prevention of the propagation of diseases to uninfected plants. Several reports suggested that AgNPs act as both bactericidal and fungicidal agent. They damage the bacterial cell wall and intercalate the nitrogenous base pairs to abstain hydrogen bond formation which ultimately leads to DNA repair and in fungus AgNPs damage hyphae, cause breakage of cytoplasm, and eventually lead to the destruction of the fungi [12].

During metabolism, free radicals and reactive oxygen species (ROS) are produced, as they are toxic substances that lead to tissue damage resulting in various diseases such as cancer, diabetes, Alzheimer's disease, and neurodegenerative disorders. Hence, antioxidants are substances that block or inhibit radicals initiated reactions. Therefore, functionalisation of AgNPs with natural antioxidants could reduce ROS production, protect the cell proteins and lipids, and hence counteract the undesirable reactions [13]. A broad spectrum of azo dyes and nitroaromatic compounds has been used in various industries such as textile manufacturing, foodstuff, paper, pharmaceuticals, and pesticides. Despite the direct disposal of these dyes and aromatic compounds into the environment, it may cause severe destruction to the aquatic ecosystem. The abundant exposure of these azo dyes and aromatic compounds into the environment is frightening owing to their hazardous, mutagenic, and carcinogenic properties. Amidst the group of azo dyes, methylene blue (MB) and methyl orange (MO) were considered as highly toxic components in the environment which was not readily biodegradable [14]. Inorganic pollutants, such as nitrophenols are considered as major pollutants and indexed in the top 114 pollutants scrutinised by the US environmental protection agency. It is clearly evident that catalytic conversion of nitrophenol to aminophenol is a prominent and environmentally benign approach that turns a hazardous pollutant to a valuable by-product which has been further employed for producing antipyretic drugs and acts as a reducing mediator for photographic developers [15].

In order to amputate these pollutants from the environment, several techniques notably adsorption, flocculation, ion exchange, and colonisation have been put forward. However, these techniques have several deprivations such as high cost and generation of secondary pollutants due to the usage of an excess amount of chemicals. Hence, the development of a facile and rapid method for the degradation of these anthropogenic pollutants is a challenging task. Among the noble metal NPs, AgNPs are of greater significance because of their elevated photo stability, economical, and enhanced catalytic activity [16].

Hence, the current study contains a depiction of our efforts to synthesise AgNPs through the factual doctrine of green chemistry using the plant *Musa paradisiaca* (*M. paradisiaca*). It is one of the illustrious plants of the Musaceae family used in the conventional therapeutic system to alleviate an assortment of health disorder. Active phytoconstituents recognised in this plant are alkaloids, flavonoids, tannins, and phenolic compounds. The bract part of *M. paradisiaca* contains anthocyanins such as delphinidin, pelargonidin, peonidin, and malvidin, which are well-known for their various bioactivities such as antioxidant, microbicidal, and anticancer activities. The enhanced contents of anthocyanins, polyphenols, and other antioxidant compounds encouraged us to select *M. paradisiaca* bract extract (MPBE) as a standalone reducing and capping mediator for the biogenic synthesis of AgNPs [17, 18]. The main focus of this study is synthesis, optimisation, characterisation, evaluation of free radical scavenging activity, microbicidal activity against phytopathogenic bacteria (*Xanthomonas campestris*, *Clavibacter michiganensis*, *Pseudomonas syringae*, and *Burkholderia glumae*) and fungal strains (*Alternaria alternata*, *Sclerotinia sclerotiorum*, *Macrophomina phaseolina*, and *Botrytis cinerea*) of AgNPs and the study also illustrates the catalytic efficiency of the fabricated Ag nanocatalyst for the wide range of anthropogenic pollutants.

2 Experimental

2.1 Materials

M. paradisiaca bract was procured from a nearby local market, Tiruchirappalli, Tamil Nadu, India. The phytopathogenic strains were obtained from the Mycology Laboratory, Centre for Advance Studies in Botany, University of Madras, Chennai. Silver nitrate (AgNO_3) and other chemicals were procured from Sigma Aldrich, India.

2.2 Preparation of MPBE

M. paradisiaca bract was washed systematically with tap water to get rid of dust particles and rinsed thoroughly with double distilled water ($\text{DD-H}_2\text{O}$). The MPBE was prepared by taking 10 g of washed and finely cut bract in a 250 ml Erlenmeyer flask with 100 ml of $\text{DD-H}_2\text{O}$ and then boiling the mixture at 60°C for 1 h under reflux conditions. Then the solution was decanted through Whatmann No. 1 filter paper. The resulting filtrate was stored at 4°C for further use as a reducing and stabilising agent.

2.3 Phytosynthesis of AgNPs

AgNPs were synthesised by adding 8 ml of MPBE to 92 ml of AgNO_3 solution. The phytofabrication of AgNPs was visually confirmed by the change of colour from light red to dark reddish brown caused by the excitation of surface plasmon vibrations in the AgNPs. Various process parameters that influence the reaction such as temperature, pH, the stoichiometric proportion of the reaction mixture and incubation time were investigated by preliminary ultraviolet (UV) spectroscopic analysis.

2.4 Characterisation of AgNPs

The obtained AgNPs were primarily screened by sampling the reaction mixture at regular intervals and the absorption maxima were scanned using a Shimadzu UV-2450 pc spectrophotometer at the wavelength of 200–800 nm. The samples for Fourier transform infrared (FTIR) spectroscopic analysis were prepared by mixing

AgNPs with KBr powder and then pelletised. The spectra were recorded using a Perkin Elmer make model spectrum RX1 (wavelength range between 4000 and 400 cm^{-1}). Crystalline metallic silver was determined using an X'Pert-PRO diffractometer. The high-resolution X-ray diffraction (XRD) patterns were measured at 3 kW with Cu target using a scintillation counter ($\lambda = 1.5406\text{ \AA}$) at 40 kV and 40 mA were recorded in the range of $2\theta = 30^\circ\text{--}80^\circ$. The images attained were compared with the Joint Committee on Powder Diffraction Standards (JCPDS) library to describe the crystalline structure. The elemental atom of the NPs was observed by using a field emission scanning electron microscope (FE-SEM) (JEOL-JSM-7600F) equipped with energy dispersive X-ray (XL 30 Philips instruments). The morphological and topographical investigation of NPs was carried out by transmission electron microscopy (TEM) using CM 200 (Philips) operating at an accelerated voltage of 200 kV. Zeta potential measurements were carried out using Malvern instruments. The free radical formation was measured by using an electron spin resonance (ESR) spectrometer Bruker EMX Plus.

2.5 Phytopathogenic activity of AgNPs

AgNPs synthesised using aqueous MPBE were investigated for their potent microbicidal activity against a few phytopathogens. All glassware, media, and reagents were sterilised in an autoclave at 121°C for 20 min.

2.5.1 Antibacterial susceptibility test: The disc diffusion method was used to evaluate the antibacterial activity. In vitro antibacterial activity was screened by using Luria–Bertani agar plates. Bacterial suspensions such as *X. campestris*, *C. michiganensis*, *P. syringae*, and *B. glumae* were used as model test strains. Different concentrations of AgNPs such as 10 μl of 5, 10, and 15 mg, MPBE extract, AgNO_3 , known standard (chloramphenicol) were loaded on a 6 mm sterile disc. The loaded disc was placed on the surface of the medium; the extract was allowed to diffuse for 5 min, and then the plates were incubated at 37°C for 24 h in an incubator. The well without any treatment was served as control throughout the experiment. At the end of incubation, the zone of inhibition formed around the disc was measured with a transparent ruler in millimetre [13].

2.5.2 Antifungal susceptibility test: The fungal pathogens such as *A. alternata*, *S. sclerotiorum*, *M. phaseolina*, and *B. cinerea* were used as model test strains and were cultured in potato dextrose agar medium. Different concentrations of AgNPs such as 10 μl of 5, 10, and 15 mg, MPBE extract, (AgNO_3), known standard (iprodione) were loaded on a 6 mm sterile disc. The loaded disc was placed on the surface of the medium; the extract was allowed to diffuse for 5 min, and the plates were incubated at $25 \pm 2^\circ\text{C}$ for 3 days. The well without any treatment was served as control throughout the experiment. After the completion of the incubation period, the zone of inhibition formed around the disc was measured with a transparent ruler in millimetre [16].

2.6 Free radical scavenging assay

2.6.1 1,1-Diphenyl-2-picryl hydroxyl (DPPH) assay: The free radical scavenging assay was evaluated for biologically synthesised AgNPs and MPBE in terms of hydrogen donating efficiency using the stable radical DPPH. It accepts an electron or a hydrogen radical with an antioxidant compound to become a stable diamagnetic molecule. In this study, different concentration (20–100 μl) of MPBE and biologically fabricated AgNPs were mixed with an equal volume of 0.1 mM methanolic DPPH solution [17]. Finally, the reaction mixture was kept at room temperature for 30 min under shaking condition and the absorbance was measured at 517 nm. Ascorbic acid was used as a standard.

2.6.2 2,2-Azinobis (3-ethylbenzothiazoline)-6-sulphonic acid (ABTS) assay: ABTS aqueous solution was prepared by mixing 7 mM of ABTS solution with 2.4 mM of potassium persulphate

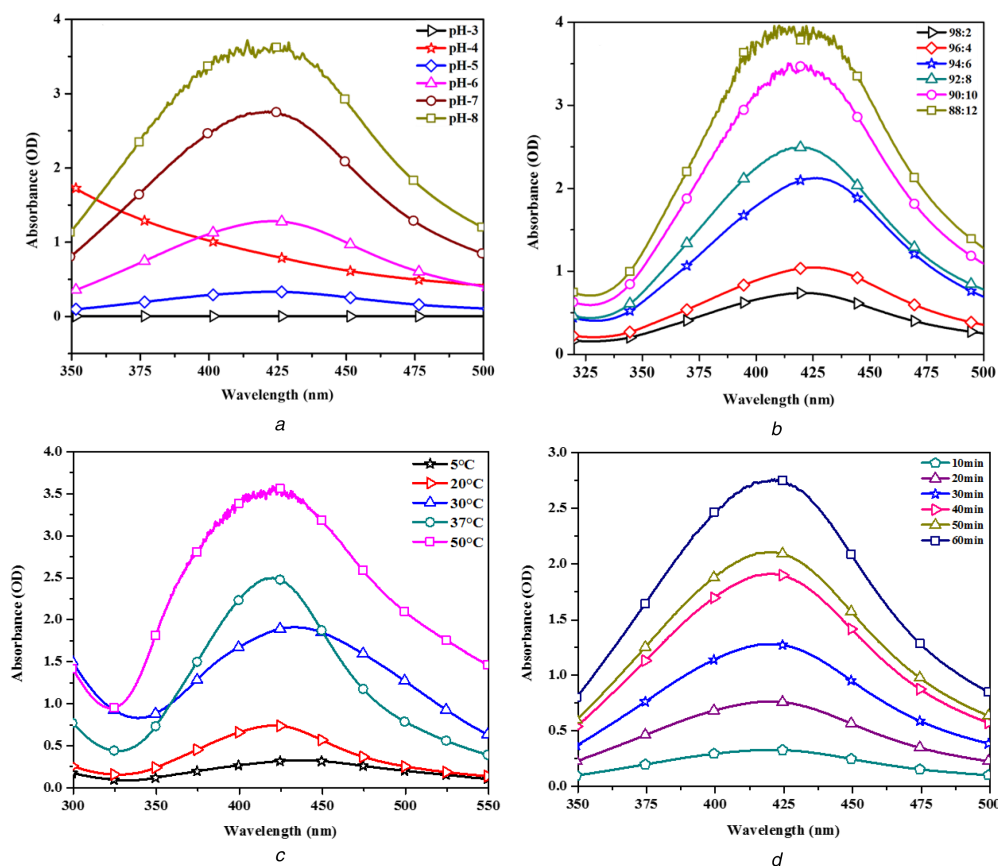


Fig. 1 UV-visible spectra of synthesised AgNPs

(a) pH optimisation studies, (b) Stoichiometric proportion, (c) Temperature optimisation studies, (d) Studies with different incubation periods

and incubated in the dark for 12–16 h at room temperature. Then the aliquot of 2 ml of ABTS solution was mixed with an equal amount of various concentrations of AgNPs and MPBE (20–100 μ l) solution. The absorbance was recorded at 734 nm after 30 min of incubation. Butylatedhydroxytoluene was used as a standard [18].

2.7 Catalytic reduction of MB, MO, and o-nitro phenol by MBPE-mediated nanocatalyst

The catalytic reduction of MB and MO was performed in aqueous solution with a standard quartz cell (1 cm path and 4 ml volume). To 1 ml of 10^{-3} M MO and MB aqueous solution, 100 mM of 1 ml freshly prepared NaBH_4 solution was added and the final volume was made up to 10 ml with double distilled water. The solution was stirred vigorously for 5 min. Then 0.5 ml of AgNPs was added to the solution and stirred for 2 min. The dye degradation was betokening by the decolorisation of the solution. In addition, the reduction of o-nitro phenol was carried out with the mixture of 1.5 ml (1 mM) of o-nitro phenol and 1.5 ml double distilled water. Then 1 mg of solid NaBH_4 was added to the aforesaid mixture. Finally, 10 μ l of Ag nanocatalyst was added and decolorisation of the yellowish solution to colourless was visually monitored. All the degradation process was monitored using UV-visible spectroscopy.

2.8 Statistical analysis

The zone of inhibition for antimicrobial activity and the percentage of inhibition for antioxidant activity were expressed as the mean and standard deviation (SD) of triplicate determinations. The statistical analysis (one way analysis of variance (ANOVA), two tailed paired *t*-test) was performed in GraphPad Prism V 7.04 (GraphPad Software, Inc., La Jolla, CA, USA). Differences were considered statistically significant at $p < 0.05$.

3 Results and discussion

3.1 Synthesis of AgNPs

The present study illustrated the expeditious formation of AgNPs synthesised from MPBE. The aqueous AgNO_3 solution acts as a reservoir of silver ions for the production of AgNPs. A decoction of MPBE was mixed with 1 mM AgNO_3 solution leads to the reduction of silver ions to silver atoms that further nucleates to form nanocrystallites that were visually confirmed by the change of colour from light red to dark reddish brown.

3.2 Characterisation of AgNPs

3.2.1 Optimisation studies: The ideal medium exposed for the bottleneck synthesis of AgNPs from MPBE was found to be (temperature: 37°C , pH: 7, the stoichiometric proportion of 1 mM AgNO_3 and reducing agent 92:8, and incubation time of 60 min). Synthesised AgNPs show a well-defined sharp peak with absorbance maxima at 420 nm under optimised conditions. Bioreduction of AgNPs due to the consequence of changing different pHs from 3 to 8 by MPBE was depicted in Fig. 1a. At pH 3 and 4 visual changes in colour were not observed and at pH 5 and 6 lower absorption spectra and broadening of the peak were observed.

Colour development was expeditious at alkaline pH but agglomeration was observed. At neutral pH, the reaction was initiated as soon as the reducing agent was added to the reaction medium and the absorption spectra were observed at 420 nm. This may be due to the ionisation of the phenolic group present in MPBE [19]. Then, the stoichiometric proportion of MPBE and AgNO_3 was also examined for the synthesis of AgNPs. From the results, it was portrayed that the optimal proportion was found to be 92 ml of 1 mM AgNO_3 with 8 ml of MPBE and the absorption spectra became sharper and increase in absorption was observed at 418 nm (Fig. 1b). When the extract proportion was further raised, agglomeration of the particles was observed [20]. The significant impact of temperature on the formation of AgNPs was examined which revealed the variation of plasmon band intensity. A sharp

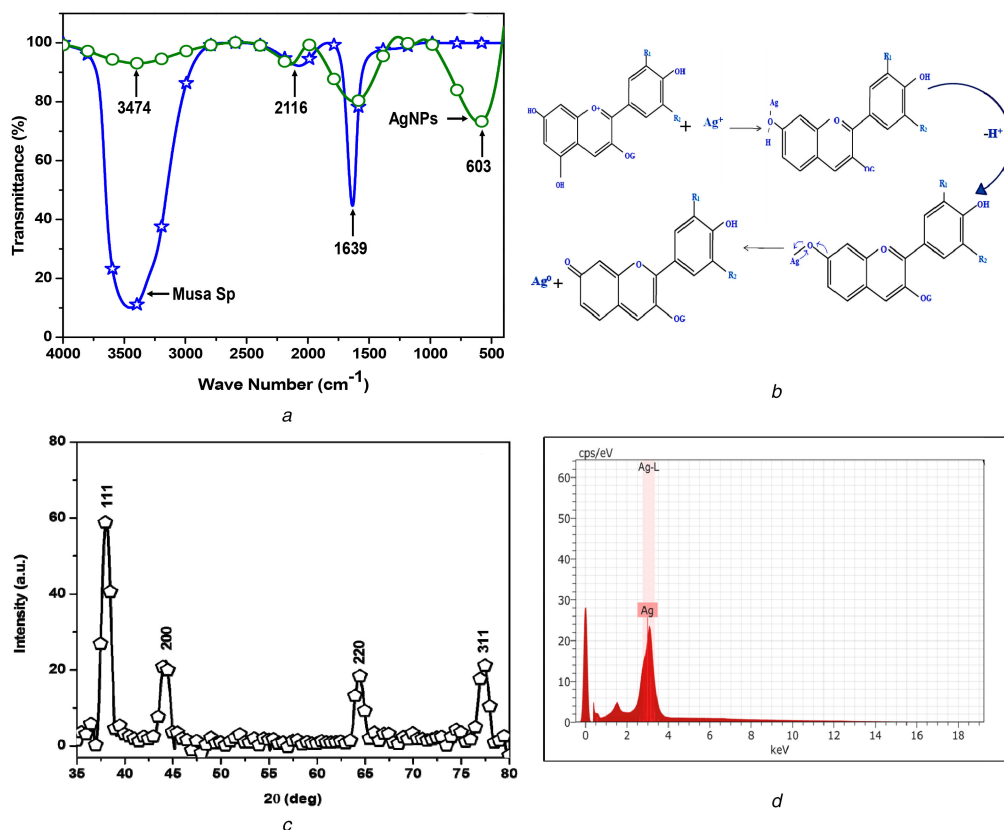


Fig. 2 Characterisation of AgNPs

(a) FTIR analysis of AgNPs and MPBE, (b) Plausible mechanism of AgNPs synthesis by anthocyanin from MPBE, (c) XRD spectrum for AgNPs, (d) Elemental analysis for AgNPs

rise in surface plasmon resonance (SPR) spectra was monitored at 420 nm at room temperature due to the favourable interaction between metal ions and anthocyanins in the decoction [21]. Consecutively a higher agglomeration rate was observed owing to the nucleation of particles with the rise in temperature (Fig. 1c). The incubation period for the production of stable colloidal NPs was also optimised. The UV-visible spectrum of AgNPs synthesised from the MPBE signifies that the absorbance of AgNPs is raised from 10 to 60 min and the sharp band was attained at 60 min which indicates the sufficient time for the controlled synthesis of AgNPs (Fig. 1d). After the incubation period, no further change in the SPR was observed denoting that the precursors had been fully consumed [22].

3.2.2 Mechanism for the reduction of Ag^+ ions: The obtained FTIR spectrum of the AgNPs indicated the existence of the reducing agent along with AgNPs (Fig. 2a). Intensive vibrations were received at the band positions of 603, 1639, 2116, and 3474 cm^{-1} . The vibration bands received at 3474, 2116, and 1639 cm^{-1} could be attributed to N–H, N=C=S vibrations and –C=C– vibrations, respectively, which could also be assigned to the phytochemicals present in MPBE extract [23]. The same vibrations with reduced intensity observed in the Ag colloid as well as the functional group vibrations shift are indicating the surface functionalised phytochemicals of AgNPs. The distinctive vibration observed at $\sim 600 \text{ cm}^{-1}$ could be assigned to the Ag–O bonding. The existence of the reducing agent along with AgNPs also confirms the biosynthesis-assisted formation of AgNPs. The reduction of AgNPs by MPBE is due to the presence of alkaloids, flavonoids, tannins, phenolic compounds, and anthocyanins. It is an entrenched fact that anthocyanin plays a dominant role in the reduction of silver ions. The feasible mechanism proposed for the reduction of Ag^+ to Ag^0 is depicted in Fig. 2b. Previous studies reported the presence of phytoconstituents such as alkaloids, flavonoids, tannins, phenolic compounds, and anthocyanin in MPBE. It was believed that anthocyanin actively chelates and reduces the silver ions to AgNPs. It has been postulated that the tautomeric conversion of anthocyanin from the enol-form to the

keto-form may liberate an active hydrogen atom that can reduce metal ions to form NPs [24, 25].

3.2.3 Structural analysis: The crystalline orientation of AgNPs was analysed by an XRD diffractogram. The Bragg's diffraction peaks at 2θ values of 38.1° , 44.2° , 64.4° , and 77.3° that correspond to the Miller indices (111), (200), (220) and (311) reveal the formation of face-centred cubic crystalline elemental AgNPs (Fig. 2c). The data obtained were indexed with the database of JCPDS (File no. 87-0717). The average crystalline size of the synthesised AgNPs was calculated by using the Scherrer equation $D = k\lambda/\beta\cos\theta$, where D is the average particle size, k is the shape factor (constant 0.9), λ is the X-ray wavelength (1.5406 Å), β is the full width at half maximum of the peak, and θ is the diffraction angle and was estimated as 15 nm. The diffraction pattern obtained was consistent with earlier reports [26, 27].

3.2.4 Morphological analysis: Fig. 2d shows the EDAX spectrum, which confirms the presence of an elemental signal of the silver and homogeneous distribution of AgNPs. A strong absorption band at 3 keV due to the excitation of SPR indicated the reduction of silver ions to AgNPs and also affirmed the crystalline property of Ag atoms. On careful examination scum on AgNPs showed the capping of organic moieties adsorbed from the MPBE which is responsible for the reduction of AgNPs [28]. The size and morphology of biologically synthesised AgNPs were visualised using TEM at 100 and 20 nm (Figs. 3a and b). From the data, it was determined that AgNPs were spherical in shape with the particle size ranging from 15 to 20 nm. The average particle size of 15 nm (Fig. 3d) was scrutinised using a particle distribution plot and was highly monodispersed surrounding by the scum of organic moieties due to the presence of anthocyanin in the MPBE which was coherent with the FE-SEM images. The selected area electron diffraction (SAED) (Fig. 3c) patterns explain a circular diffraction pattern, which denotes the crystalline nature of AgNPs that were consistent with the XRD data [29, 30]. The zeta potential analysis of stable AgNPs exhibits a strong peak at -22.9 mV due to the capping of phytoconstituents [23]. The negative value confirms the

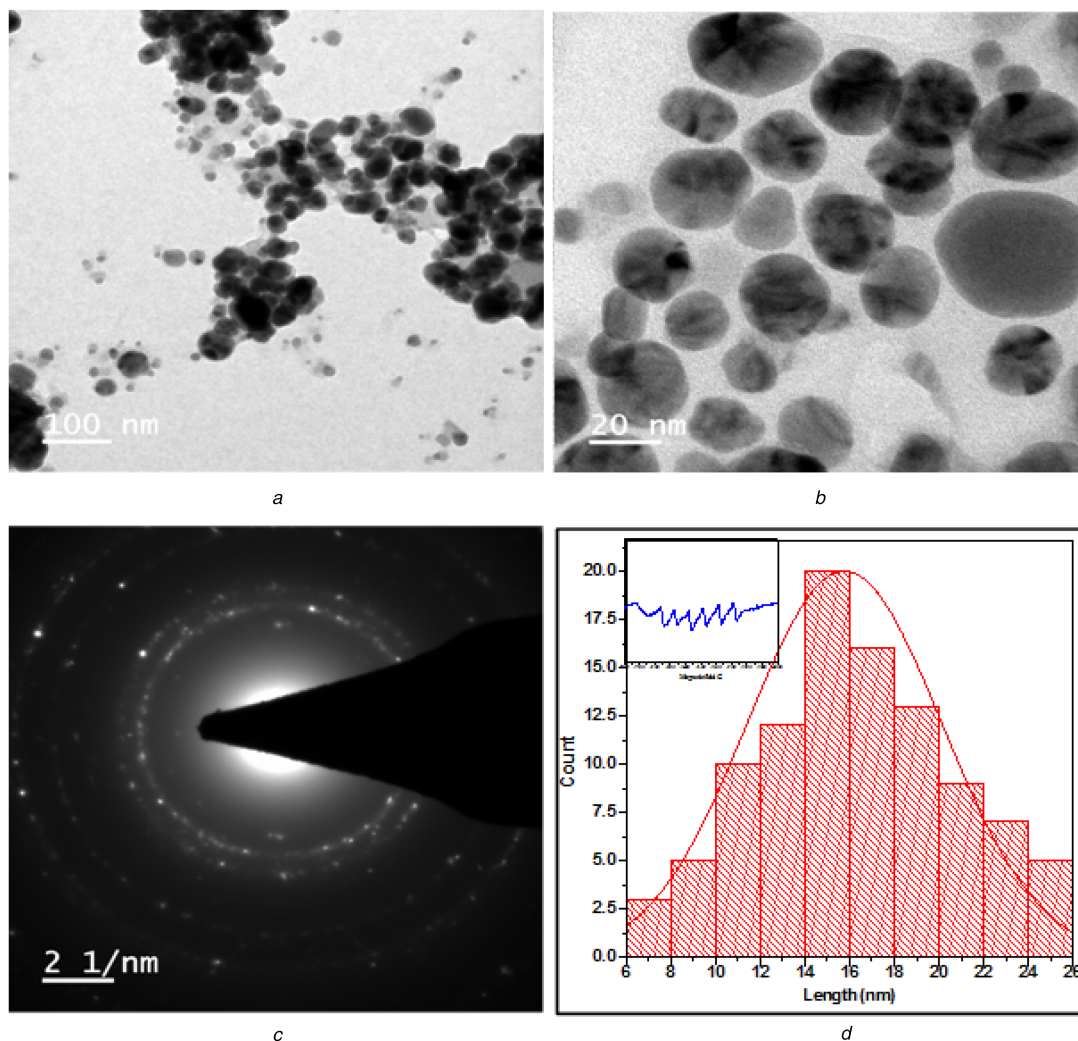


Fig. 3 Morphological analysis

(a), (b) TEM micrograph showing size AgNPs with different magnifications, (c) SAED pattern of AgNPs, (d) Particle size distribution analysis, (inset) ESR spectra of the synthesised AgNPs were measured in room temperature at a microwave frequency of 9.770 GHz with a microwave power of 10 mW and a modulation amplitude of 2.0 F

repulsion between the particles which clearly proves their long time stability and is depicted in Fig. 4c.

3.3 Antimicrobial assays

The antimicrobial activity of MPBE, AgNO₃ solution, biologically fabricated AgNPs and the standard chloramphenicol for bacteria and iprodione for fungi was evaluated against phytopathogens by the disc diffusion method. The statistical analysis was conducted using the one way analysis of variance (ANOVA) test which showed that the AgNPs had significant activity in all fungal species and two bacterial species with $p < 0.05$ (Fig. 4a). The minimum inhibition zone of 6.8 and 7.20 mm for *X. campestris*, *C. michiganensis*, *P. syringae*, *B. glumae* showed the maximum inhibition of 12.9 and 12.7 mm [31]. Fig. 4b shows the antifungal activity of the phytopathogens. A clear zone of inhibition ranging from 12.5 to 12.8 mm was observed for all tested phytopathogenic fungi. *B. cinerea* showed the least inhibition zone of 12.5 mm, whereas *A. alternata*, *S. sclerotiorum*, and *M. Phaseolina* showed the highest inhibition zone of 12.8, 12.6 and 12.7 mm [32]. Obviously biologically synthesised AgNPs inhibit the growth of all tested phytopathogens at 15 mg concentration. A comparative effect with commercially available antimicrobials was scrutinised in the present study which reveals that the synthesised AgNPs inhibited the growth of all tested phytopathogens more strongly than that of known standards. There is no prominent antimicrobial activity observed in AgNO₃ solution and crude extract against tested phytopathogens in resemblance with the synthesised AgNPs (Table 1). The feasible mechanism behind the antimicrobial activity of biologically formulated AgNPs is that it

anchors the cell wall consecutively and penetrates into it which produces free radicals resulting in induction of oxidative, DNA, or electron transport chain damage consequently leading to bacterial death. Similarly, AgNPs impinge on fungus cells by attacking their membranes, thus interrupting the membrane potential that leads to cell death [33]. The formation of free radicals was confirmed by ESR spectroscopy which was depicted in Fig. 3d (inset). Krishnaraj *et al.* synthesised spherical-shaped AgNPs from *Acalypha indica* leaf extract with the size ranging from 10 to 50 nm that exhibit moderate antimicrobial activity against plant pathogens [22]. Kanniah *et al.* synthesised spherical-shaped AgNPs from the leaf extract of *Piper nigrum* of size ranging from 4 to 14 and from 20 to 50 nm that show good antimicrobial activity [31]. In our study, the synthesised NPs exhibit excellent antimicrobial activity due to the monodispersity and the capping of phytoconstituents present in the MPBE [2].

3.4 In-vitro free radical scavenging assays

The free radical quenching effect of MPBE and the biologically fabricated AgNPs was determined using DPPH assay. DPPH is a stable free radical that can be reduced by the acceptance of hydrogen or electrons which was visually observed by the change of colour from purple to yellow and quantified by UV-visible spectroscopy at 517 nm. Based on the dose-dependent manner, the DPPH activity of AgNPs and MPBE was found to be increased and two tailed paired *t*-test was conducted for antioxidant scavenging activity of MPBE and AgNPs and showed significant activity in both DPPH and ABTS solution and found to be $p < 0.001$ is depicted in Fig. 5a. The average percentage of inhibition of

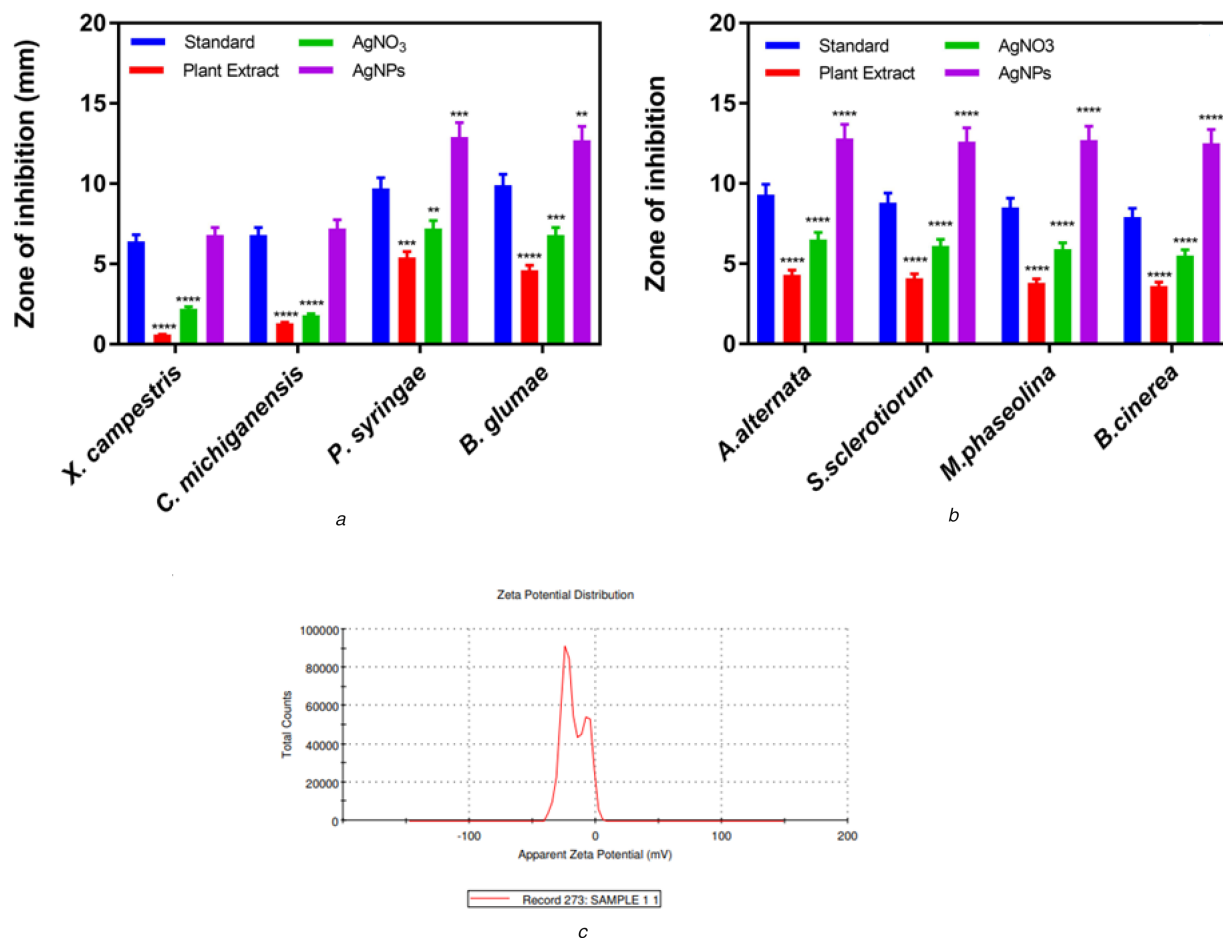


Fig. 4 Antimicrobial activity

(a) Antibacterial activity of extract, precursor, synthesised AgNPs, and standard, (b) Antifungal activity of extract, precursor, synthesised AgNPs, and standard. The data are expressed as mean \pm SD ($n=3$) where the zone of inhibition was analysed using one way ANOVA, ** $p < 0.01$, *** $p < 0.001$, **** $p < 0.0001$, (c) Zeta potential analysis of synthesised AgNPs

Table 1 Zone of inhibition for antibacterial and antifungal activity (mm)

S. no.	Name of the organism	Plant extract	AgNO ₃	AgNPs 15 mg/10 μ l	Standard
Bacteria					
1	<i>X. campestris</i>	0.60 \pm 0.03****	2.20 \pm 0.14****	6.80 \pm 0.48	6.40 \pm 0.42
2	<i>C. michiganensis</i>	1.30 \pm 0.08****	1.80 \pm 0.11****	7.20 \pm 0.56	6.80 \pm 0.48
3	<i>P. syringae</i>	5.40 \pm 0.37***	7.20 \pm 0.50**	12.90 \pm 0.90***	9.70 \pm 0.67
4	<i>B. glumae</i>	4.60 \pm 0.32****	6.80 \pm 0.47***	12.70 \pm 0.88**	9.90 \pm 0.69
Fungi					
1	<i>A. alternata</i>	4.30 \pm 0.30****	6.50 \pm 0.450****	12.80 \pm 0.89****	9.30 \pm 0.65
2	<i>S. sclerotiorum</i>	4.10 \pm 0.28****	6.10 \pm 0.42****	12.60 \pm 0.88****	8.80 \pm 0.61
3	<i>M. phaseolina</i>	3.80 \pm 0.26****	5.90 \pm 0.41****	12.70 \pm 0.88****	8.50 \pm 0.59
4	<i>B. cinerea</i>	3.60 \pm 0.25****	5.50 \pm 0.38****	12.50 \pm 0.87****	7.90 \pm 0.55

The data are expressed as mean \pm SD ($n=3$) where the zone of inhibition was analysed using one way ANOVA, ** $p < 0.01$, *** $p < 0.001$, **** $p < 0.0001$.

biologically synthesised AgNPs was 62% as compared to that of MPBE (45%). Biologically fabricated AgNPs show higher radical inhibition activity than that of MPBE due to the reactivity of functional groups attached on the huge surface area of AgNPs that entrap high free radicals than that of MPBE [34, 35]. Similarly, the synthesised AgNPs and MPBE show comparable scavenging activity on ABTS⁺ as shown in Fig. 5b. The reduction of ABTS⁺ free radical was visually observed by the change of colour from blue-green to transparent solution due to the reduction of ABTS⁺ to ABTS by a surface reaction phenomenon, which was measured at 734 nm using UV-visible spectroscopy. The ABTS quenching effect was higher to AgNPs (74%) than that of MPBE (52%) [36, 37]. From the above results of DPPH and ABTS assays, it can be inferred that the antioxidant potential of MPBE extract has been retained by biologically fabricated AgNPs possibly due to the

capping of the phytochemicals. As the AgNPs solution possesses the proton-donating ability it could act as a free radical scavenger, possibly serving as a primary antioxidant.

3.5 Catalytic property of biologically fabricated Ag nanocatalyst

3.5.1 Degradation of MO and MB: The degradation of MO and MB has been selected as a model reaction to investigate the proficiency of the MPBE-mediated Ag nanocatalyst. Fig. 6a depicts the compiled absorption spectra of UV-visible spectroscopy of MO in the presence of NaBH₄ and Ag as a nanocatalyst at room temperature. The absorption spectrum of MO was detected at 460 nm in the presence of NaBH₄, after the addition of a biologically fabricated Ag nanocatalyst with MO and

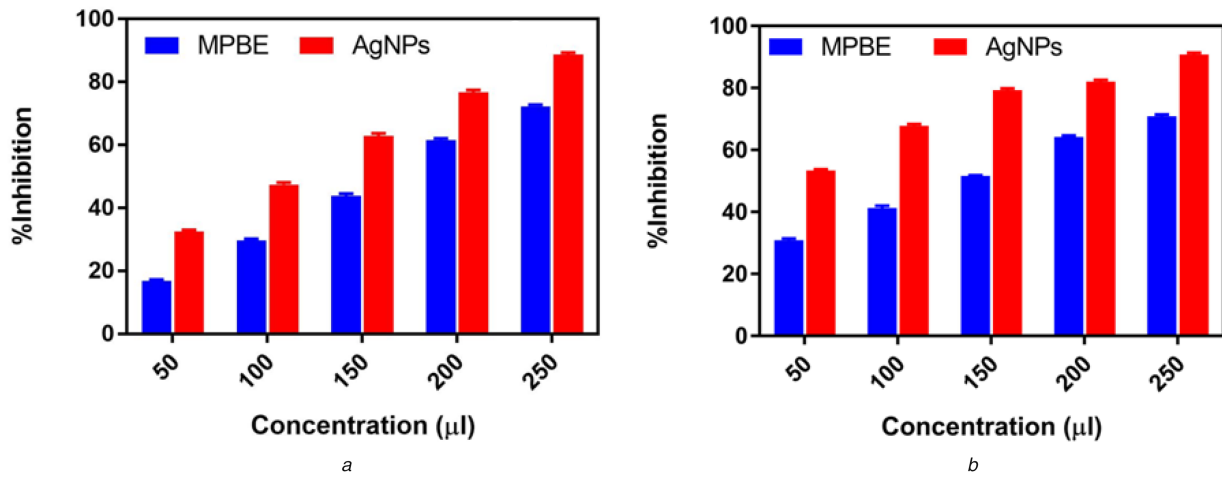


Fig. 5 Free radical scavenging assay

(a) DPPH assay for extract and AgNPs, (b) ABTS for extract and AgNPs. The data are expressed as mean \pm SD ($n = 3$). Percentage of inhibition was compared with that MPBE (paired samples t -test, two-tailed). * $p < 0.001$

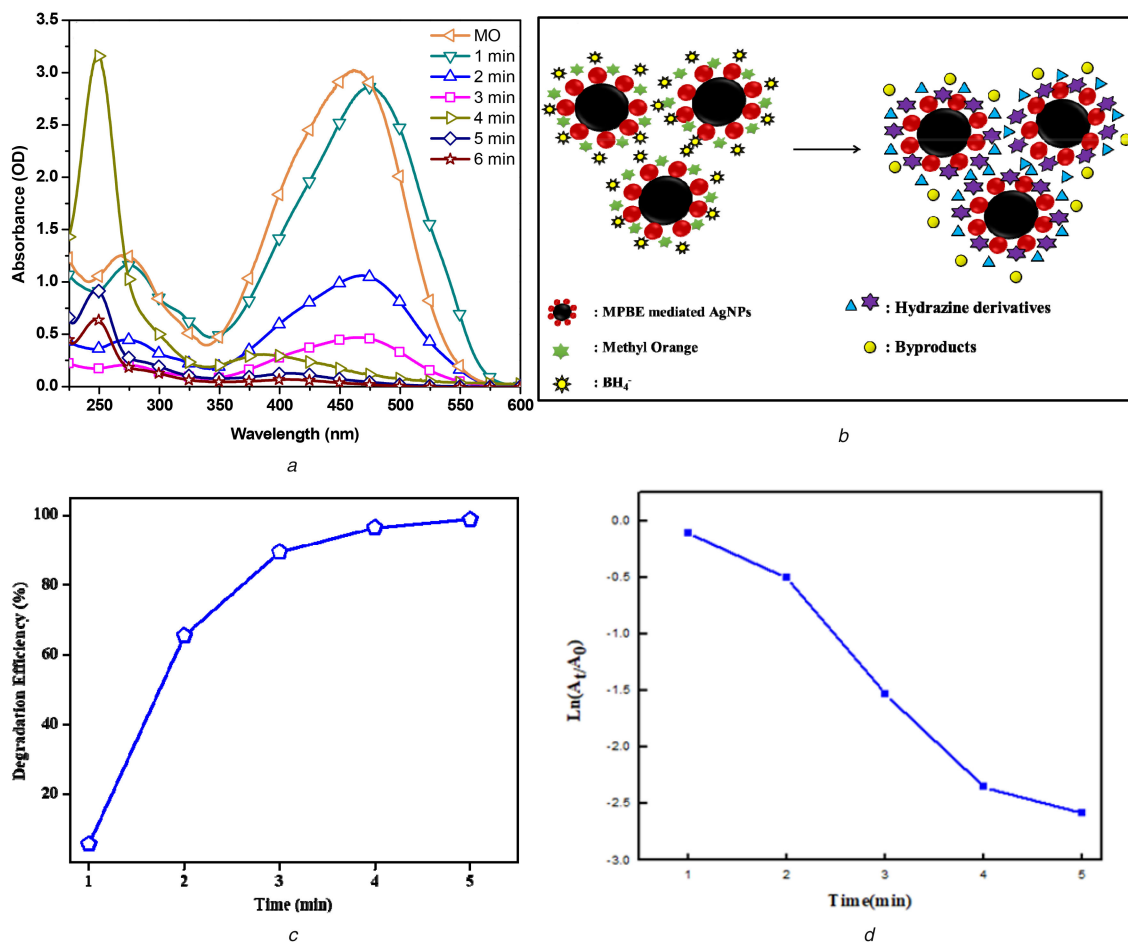


Fig. 6 Catalytic activity:

(a) UV-visible spectra of the reduction of MO with the aid of the MPBE-mediated Ag nanocatalyst in aqueous solution recorded every 1 min, (b) Schematic representation for the degradation of MO using MPBE-mediated AgNPs, (c) Degradation efficiency of MO with respect to time, (d) Plot of $\ln(A_t/A_0)$ versus reaction time for the reduction of MO

NaBH_4 solution, adsorption of MO molecules with the well-dispersed Ag nanocatalyst occurs, which results in the polarisation and the activation of those molecules. Subsequently, the transfer of electrons between MO and NaBH_4 was stimulated with the reduction of activation energy of the reaction. The resulting product of the reaction between MO and NaBH_4 was propagated on the surface of the nanocatalyst which was then diffused into the solution leading to a colour change from orange to a colorless solution as shown in Fig. 6b. Hence the MO absorption band at 460 nm disappears and the new band at 247 nm is assigned to the hydrazine derivatives. Furthermore, the kinetics of the reaction and

the degradation efficiency of MO were evaluated with time-dependent absorption spectra [38]. As NaBH_4 concentration was higher than MO concentration it does not influence the rate of the reaction. So the reduction process follows pseudo first-order kinetics which can be written as

$$\ln(A_t/A_0) = -K_{\text{app}}t,$$

where A_t is the absorbance of dye at time t and A_0 is the absorbance at $t = 0$, K_{app} is the apparent rate constant. Fig. 6d shows the plot of $\ln(A_t/A_0)$ versus time. From the plot, we can

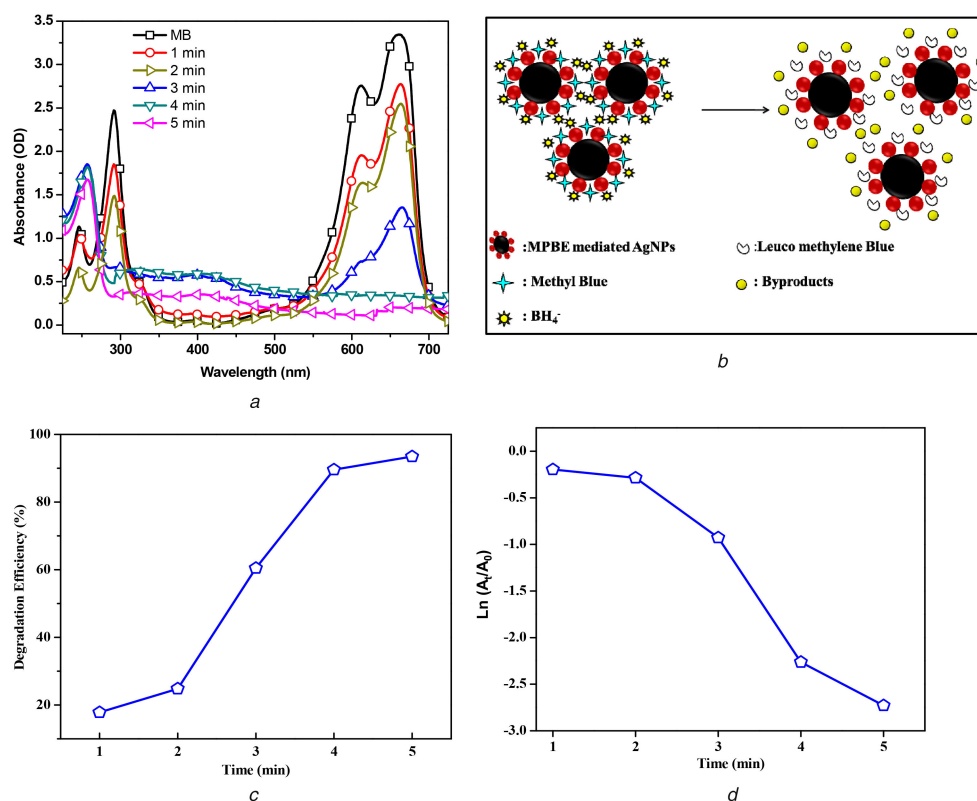


Fig. 7 Catalytic activity

(a) UV-visible spectra of the reduction of MB with the aid of MPBE-mediated Ag nanocatalyst in aqueous solution recorded every 1 min, (b) Schematic representation for the degradation of MB using MPBE-mediated AgNPs, (c) Degradation efficiency of MB with respect to time, (d) Plot of $\ln(A_t/A_0)$ versus reaction time for the reduction of MB

easily calculate the rate constant (K_{app}) value, which was obtained from the slope $k = 1.0991 \text{ min}^{-1}$ [39].

Fig. 6c shows that the degradation efficiency of the MO was found to be 98% in 5 min in the presence of the MPBE-mediated Ag nanocatalyst.

MB is a heterocyclic aromatic compound that exhibits the characteristic absorption peak at 662 nm with NaBH_4 at room temperature. After the addition of Ag nanocatalyst, the absorption intensity decreases as a function of time (Fig. 7a). The reduction process takes place by electron transfer from NaBH_4 to AgNPs which facilitates the electrophilic dye (MB) to capture electrons from the nanocatalyst and rapidly reduces the reduction process (Fig. 7b). The degradation of the MB dye follows pseudo-first-order kinetics. From the plot (Fig. 7d) the rate constant (K_{app}) of the reaction was calculated from the slope $k = 0.704 \text{ min}^{-1}$. The reduction efficiency of MB was found to be 93% in 5 min with the aid of a biologically fabricated Ag nanocatalyst and NaBH_4 as shown in Fig. 7c.

3.5.2 Degradation of o-nitrophenol to o-aminophenol: The reduction of o-nitrophenol to o-aminophenol in the presence of NaBH_4 was monitored by a UV-visible absorption band. From Fig. 8a, it was ascertained that the o-nitrophenol has the characteristics peak at 340 nm on the addition of NaBH_4 to o-nitrophenol solution the peak shifted from 340 to 400 nm with the visual detection of the yellow coloured solution. This indicates the formation of nitrophenolate ions when a scanty amount of the MPBE-fabricated Ag nanocatalyst was added to the solution. Reduction of o-nitrophenol was expeditious and was confirmed by the decolorisation of a bright yellow coloured solution. The peak at 400 nm reduced evidently and the yellow colour of the solution vanishes which indicates the reduction of o-nitrophenolate ions. Simultaneously the new peak at 280 nm was observed that corresponds to the formation of o-aminophenol. The schematic illustration is shown in Fig. 8b. Meanwhile, kinetics of the reaction was examined from the time-dependent absorption spectrum. When the surplus amount of NaBH_4 was added to the reaction

compared to that of o-nitrophenol the rate of the reaction is suspected to be independent of NaBH_4 . Hence the kinetic data obeys pseudo-first-order kinetics [15]. From the plot (Fig. 8d) the rate constant (K_{app}) $k = 0.1997 \text{ min}^{-1}$ of the reaction was calculated. Then the degradation efficiency of o-nitrophenol was found to be 85% in 5 min (Fig. 8c) [40]. From the catalytic activity of the biologically fabricated Ag nanocatalyst, it was noteworthy that the efficiency of AgNPs as an electron relay system. Conspicuously, our AgNPs act as an enhanced electron relay by promoting electron transfer for the catalytic reduction of the aforesaid anthropogenic pollutants in the presence of NaBH_4 .

4 Conclusion

In this study, MPBE-mediated AgNPs were obtained with a confined size distribution and the extract standalone as both reducing and capping mediator with higher stability. The entire preparation process garnered the doctrine of green chemistry and the resulting AgNPs showed significant potential in pharmacological and agricultural fields. As one side the fabricated AgNPs efficiently inhibit the growth of phytopathogens due to the higher dispersion of AgNPs. On the other hand, the AgNPs actively suppress the free radical production to prevent cell damage. Hence the above results clearly betrayed the MPBE-AgNPs used as a potential candidate in the preparation of pharmaceutical products against various degenerative diseases originated from free radicals and in the beneficial application in crop improvement and has a great defence in agricultural nanotechnology.

5 Acknowledgments

Authors gratefully acknowledge the SAIF, Mumbai for providing all spectroscopic images.

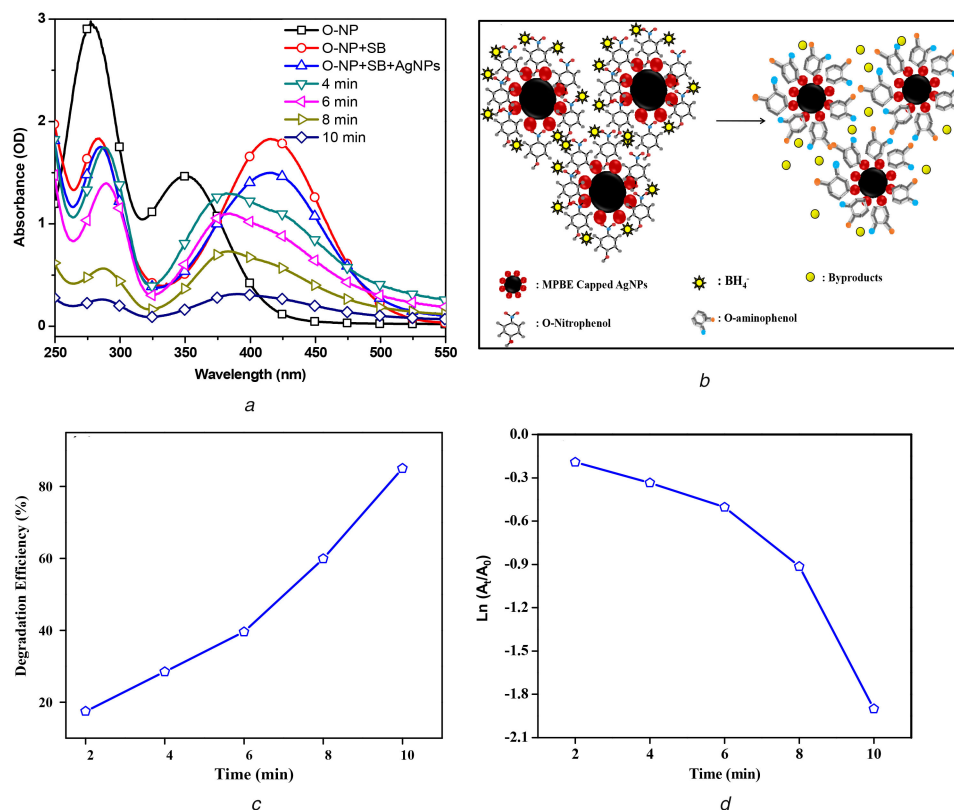


Fig. 8 Catalytic activity

(a) UV-visible spectra of the reduction of o-nitrophenol to o-aminophenol with the aid of MPBE-mediated Ag nanocatalyst in aqueous solution recorded every 1 min, (b) Schematic representation of the degradation of o-nitrophenol using MPBE-mediated AgNPs, (c) Degradation efficiency of o-nitrophenol with respect to time, (d) Plot of $\ln(A_t/A_0)$ versus reaction time for the reduction of o-nitrophenol

6 References

- [1] Chauhan, K., Sharma, R., Dharela, R., et al.: *RSC Adv.*, 2016, doi: 10.1039/C6RA13466A
- [2] Moosavi, R., Ramanathan, S., Lee, Y. Y., et al.: *RSC Adv.*, 2015, **5**, p. 76442
- [3] Moldovan, B., David, L., Achim, M., et al.: *J. Mol. Liq.*, 2016, **221**, pp. 271–278
- [4] Swaminathan, B., Several, M., Sukumaran, M., et al.: *RSC Adv.*, 2016, doi: 10.1039/C6RA17569D
- [5] Ahmad, A., Syed, F., Shah, A., et al.: *RSC Adv.*, 2015, **5**, pp. 99364–99377
- [6] Liu, J., Zhao, Z., Feng, H., et al.: *J. Mater. Chem.*, 2012, **22**, p. 13891
- [7] Moulton, M. C., Braydich-Stolle, L. K., Nadagouda, M. N., et al.: *Nanoscale*, 2010, **2**, pp. 763–770
- [8] Sahni, G., Panwar, A., Kaur, B.: *Int. Nano Lett.*, 2015, **5**, pp. 93–100
- [9] Krishna, M., Bhagavanth Reddy, G., Veerabhadram, G., et al.: *Appl Nanosci.*, 2016, **6**, (5), pp. 681–689
- [10] Kumari, R., Brahma, G., Rajak, S., et al.: *Orient Pharm. Exp. Med.*, 2016, **16**, (3), pp. 195–201
- [11] Yugandhar, P., Haribabu, R., Savithamma, N.: *3 Biotech.*, 2015, **5**, (6), pp. 1031–1039
- [12] Lee, K.-J., Park, S.-H., Govarthanan, M., et al.: *Mater. Lett.*, 2013, **105**, pp. 128–131
- [13] Kokila, T., Ramesh, P. S., Geetha, D.: *Ecotoxicol. Environ. Saf.*, 2016
- [14] Ajmal, M., Demirci, S., Siddiq, M., et al.: *New J. Chem.*, 2016, **40**, (2), pp. 1485–1496
- [15] Ji, T., Chen, L., Schmitz, M., et al.: *Green Chem.*, 2015, **17**, (4), pp. 2515–2523
- [16] Edison, T. J. I., Sethuraman, M. G.: *Spectrochim. Acta A, Mol. Biomol. Spectrosc.*, 2013, **104**, pp. 262–264
- [17] Mahmood, A., Ngah, N., Omar, M. N.: *Eur. J. Sci. Res.*, 2011, **66**, (2), pp. 311–318
- [18] Alexandra Pazmino-Duran, E., Monica Giusti, M., Wrolstad, R. E., et al.: *Food Chem.*, 2001, **73**, pp. 327–332
- [19] Vanathi, P., Rajiv, P., Sivaraj, R.: *Bull. Mater. Sci.*, 2016, **39**, (5), pp. 1165–1170
- [20] Saha, N., Trivedi, P., Dutta Gupta, S.: *J. Clust. Sci.*, 2016, **27**, (6), pp. 1893–1912
- [21] Kuppurangan, G., Karuppasamy, B., Nagarajan, K., et al.: *Appl. Nanosci.*, 2016, **6**, pp. 973–982
- [22] Krishnaraj, C., Ramachandran, R., Mohan, K., et al.: *Spectrochim. Acta A*, 2012, **93**, pp. 95–99
- [23] Balraj, B., Arulmozhi, M., Siva, C., et al.: *IET Nanobiotechnol.*, 2017, **11**, (3), pp. 241–246
- [24] Makarov, V. V., Love, A. J., Sinitsyna, O. V., et al.: *Acta Nat.*, 2014, **6**, p. 35
- [25] Kumar, B., Smita, K., Cumbal, L., et al.: *J. Mol. Liq.*, 2015, **211**, pp. 476–480
- [26] Anandalakshmi, K., Venugobal, J., Ramasamy, V.: *Appl. Nanosci.*, 2016, **6**, (3), pp. 399–408
- [27] Balan, K., Qing, W., Wang, Y., et al.: *RSC Adv.*, 2016, **6**, p. 40162
- [28] Prabhua, D., Arulvasua, C., Babua, G., et al.: *Process. Biochem.*, 2013, **48**, pp. 317–324
- [29] Kumar, B., Smita, K., Debut, A., et al.: *Trans. Nonferrous Met. Soc. China*, 2016, **26**, pp. 2363–2371
- [30] Ajitha, B., Ashok Kumar Reddy, Y., Sreedhara Reddy, P., et al.: *J. Mol. Liq.*, 2016, **219**, pp. 474–481
- [31] Paulkumar, K., Gnanajobitha, G., Vanaja, M., et al.: *Sci. World J.*, 2014, **829894**, p. 9
- [32] Medda, S., Hajra, A., Dey, U., et al.: *Appl. Nanosci.*, 2015, **5**, (7), pp. 875–880
- [33] Baranwal, A., Mahato, K., Srivastava, A., et al.: *RSC Adv.*, 2016, (107), doi: 10.1039/C6RA23411A
- [34] Bhuvanawari, R., John Xavier, R., Arumugam, M.: *J. Parasit. Dis.*, DOI: 10.1007/s12639-016-0773-6
- [35] Parveen, M., Ahmad, F., Malla, A. M., et al.: *Appl. Nanosci.*, 2016, **6**, (2), pp. 267–276
- [36] Kokila, T., Ramesh, P. S., Geetha, D.: *Appl. Nanosci.*, 2015, **5**, (8), pp. 911–920
- [37] Mittal, A. K., Bhaumik, J., Kumar, S., et al.: *J. Colloid Interface Sci.*, 2013, **415**, pp. 39–47
- [38] Zheng, L.-Q., Yu, X.-D., Xu, J.-J., et al.: *Chem. Commun.*, 2015, **51**, (6), pp. 1050–1053
- [39] Jyoti, K., Singh, A.: *J. Genet. Eng. Biotechnol.*, 2016, **14**, (2), pp. 311–317
- [40] Baruah, B., Gabriel, G. J., Akbashev, M. J., et al.: *Langmuir*, 2013, **29**, (3), pp. 4225–4234
- [41] Vimala, R. T. V., Sathishkumar, G., Sivaramakrishnan, S.: *Spectrochim. Acta A, Mol. Biomol. Spectrosc.*, 2015, **135**, pp. 110–115
- [42] Saware, K., Venkataraman, A.: *J. Clust. Sci.*, 2014, **25**, (4), pp. 1157–1171
- [43] Baghizadeh, A., Ranjbar, S., Gupta, V. K., et al.: *J. Mol. Liq.*, 2015
- [44] Chokshi, K., Pancha, L., Ghosh, T., et al.: *RSC Adv.*, 2016, **6**, pp. 72269–72274
- [45] Bordbar, M.: *RSC Adv.*, 2017, **7**, (1), pp. 180–189